Evaluating the electrochemical properties and behaviour of copper/cobalt minerals

Using Cyclic Voltammetry and Electrochemical Quartz Crystal Microbalance techniques

---

Chris (C.H.J) Elpenhof

As part of the CoG^3 *project*

Electrochemical experiments
(CV + EQCM) in progress
Please do not (re)move any
equipment and/or chemicals.
Mineral Proce
PHURIC ACID
ZED WATER

Evaluating the electrochemical properties and behaviour of copper/cobalt minerals

Using Cyclic Voltammetry and Electrochemical Quartz Crystal Microbalance techniques

by

C.H.J. Elpenhof

to obtain the degree of Master of Science
at the Delft University of Technology,
to be defended publicly on Monday October 28, 2019 at 10:00.

Student number:	4228693	
Project duration:	February 4, 2019 – October 28, 2019	
Thesis committee:	Prof. dr. ir. H. J. Glass,	Camborne School of Mines (supervisor)
	Dr. M. W. N. Buxton,	TU Delft; *Resource Engineering*
	Dr. M. C. M. Bakker,	TU Delft; *Resources & Recycling*

An electronic version of this thesis is available at `http://repository.tudelft.nl/`.

Acknowledgements

This thesis was written in many places: in an office in Cornwall with heavy construction work outside, a picturesque pier in Falmouth, on a couple of planes, in a number of hotel rooms, in the United Kingdom and the Netherlands, in the centre of a city, and in coffee bars and cafe's, with ideas scribbled on the proverbial paper napkin, in notebooks, and on a laptop, all the while realising that with this thesis I will conclude my Master of Science in Geo-Resource Engineering at Delft University of Technology. After eight memorable years, my student life is coming to an end.

Throughout the writing of this dissertation I have received a great deal of support and assistance. I would first like to thank my supervisor, Hylke J. Glass, whose expertise was invaluable in the formulating of the research topic and especially for hosting me at Camborne School of Mines and creating the ability to write this thesis in Cornwall. I would like to thank my supervisor from TU Delft, Mike Buxton for his assistance during my work on this thesis. My appreciation also goes out to Maarten Bakker, for reviewing this thesis and being part of the assessment committee.

I would also like to thank the research staff of Camborne School of Mines, Dr. Gavyn Rollinson and Miss. Sharon Uren, for their valuable guidance and support with every question I asked and every chemical composition I requested. You provided me with the tools that I needed to choose the right direction and successfully complete my thesis. I also would like to thank Dr. Caroline Kirk and Sandra Dreßler from Loughborough University for providing the synthetic cobalt samples used in the thesis. I would like to thank Laurens Tijsseling for the previous work carried out on this subject and the obtained results that are also incorporated in this thesis.

I would like to acknowledge my colleagues from the PhD-room for the wonderful time I had with all of you, making it a lot easier to get a good start in a completely new environment. You supported me greatly and were always willing to help me. Also outside the office hours it was very nice to have some fun parties and eating-out evenings from time to time. Also a big thanks to my former roommates Drew, Stan and Tim for welcoming me into their house and making my time here much more enjoyable.

In addition, I would like to thank my family and friends for their support and sympathetic ear, even when I was a hundred miles away on the other side of the sea. Finally, there is my girlfriend Charlotte, who was of great support in deliberating over a lot of grammar and structure in this thesis, as well as providing a happy distraction to rest my mind outside of my research. Thank you so much!

C.H.J. (Chris) Elpenhof
Falmouth (U.K.), October 2019

Abstract

Mining projects around the world face a significant challenge to reduce their footprint and be more environmentally friendly. Research has shown that mineral processing is of major influence, due to the use of heavy chemicals that are both expensive and polluting. Currently, electrowinning (the electrodeposition of metals) is only used in the last purification step of the process. So far, the majority of the studies on cobalt have focused on non-electrowinning possibilities. Therefore, it is of interest to investigate the electrochemical behaviour within different environments to obtain more information and gain a better understanding.

This thesis focuses on the electrochemical behaviour and deposition of cobalt-bearing minerals, which will be evaluated with the help of cyclic voltammetry (CV) and the electrochemical quartz crystal microbalance (EQCM). These techniques use the help of multiple variable input parameters, which will be investigated and compared to gain the optimised condition to perform the experiments. Furthermore, the sensitivity of the techniques to different input parameters and different solutions will be investigated. This is done to investigate what the origins are for the differences in the electrochemical behaviour of copper-cobalt minerals in aqueous solutions using analytical, synthetic and real ores, and to find a correlation between the obtained results using the graphs generated using CV and EQCM-techniques. This is done to investigate to possibilities using selective electrowinning, meaning the electrodeposition of multiple elements within the same electrolyte solution.

Based on a review of the literature, the experimental setup used for the experiments will be discussed to gain better understanding of the specialised equipment and corresponding software. Cobalt chloride, cobalt sulphate and copper sulfate solution will be evaluated first, after which two synthetic cobalt-bearing minerals containing iron will be tested. With the help of CV, the electrochemical behaviour, e.g. redox- reactions, can be analysed. Using the EQCM, accurate measurements of the mass change per unit area of the electroplated cobalt will be recorded. Synthetic minerals will be used to discover how much can be recovered using this technique. Finally, six samples from the Democratic Republic of Congo (DRC) will be evaluated to obtain the same data as for the synthetic minerals. For this QEMSCAN data is used to evaluate the mineral composition.

Analysis of the results demonstrated that under different circumstances in different environments, similar electrochemical behaviour and the occurrence of copper, iron and/or cobalt deposition is observed. However, for special cases these reactions do not occur. This difference can be explained by a varying mineralogy, where bornite and chalcopyrite have a positive effect on the electrochemical activity. Regarding the shape of the voltammogram, the number of electrons involved in the reaction has the largest influence. Furthermore, alkaline conditions have a positive effect on the electrodeposition of cobalt. No overall correlation has been found between the samples. For all experiments similar reactions and electrochemical activity is observed regarding the peak potentials and within the same environment, correlations can be found.

Recommendations for further research are to investigate the influence of changes to parameters such as temperature, magnetic field and impurities on the electrochemical behaviour of the reaction and changes in the yield of electrodeposited material, to generate more data to validate and calibrate the characteristic potentials that can be used for selective electrowinning and to gather more data of the selective electrowinning experiments in terms of additional (rare) elements, such as Lithium.

Contents

List of Abbreviations and Symbols **x**

List of Figures **xi**

List of Tables **xv**

1 Introduction **1**
- 1.1 Cobalt 1
  - 1.1.1 Production and reserves 1
  - 1.1.2 Use 2
  - 1.1.3 Occurrence 3
  - 1.1.4 Price 3
- 1.2 CoG3 project 4
- 1.3 Electrochemistry 4

2 Research approach **5**
- 2.1 Problem definition 5
- 2.2 Objective 5
- 2.3 Research questions 6
- 2.4 Scope 6
- 2.5 Methodology 6

3 Literature review **7**
- 3.1 Mutanda mining operation 7
  - 3.1.1 Regional geology 8
  - 3.1.2 Local geology 9
  - 3.1.3 Mineralisation 10
  - 3.1.4 Mineral resources and ore reserves 11
  - 3.1.5 Electrowinning 11
  - 3.1.6 Future 12
- 3.2 Electrochemical processes 13
  - 3.2.1 Electrode reactions 13
  - 3.2.2 Phase formation and growth 16
  - 3.2.3 Cobalt deposition 17
- 3.3 Cyclic voltammetry 18
  - 3.3.1 Wave characteristics 19
  - 3.3.2 Electrochemical reversibility 20
  - 3.3.3 Scan rate 22
- 3.4 Electrochemical quartz crystal microbalance 23
- 3.5 Effects on the electrochemical behaviour of cobalt 25
  - 3.5.1 Temperature 25
  - 3.5.2 pH-value 26
  - 3.5.3 Concentration 27
  - 3.5.4 Magnetic fields 27
  - 3.5.5 Additives and impurities 28
- 3.6 Simulated cyclic voltammetry 29
  - 3.6.1 Microsoft Excel 30
  - 3.6.2 MATLAB 30

4 Experimental setup and procedures **33**
- 4.1 Electrochemical cell 33
  - 4.1.1 Electrolyte solution 34

4.1.2 Working electrode . . . 34
4.1.3 Counter electrode . . . 34
4.1.4 Reference electrode . . . 34
4.1.5 Electrode polishing . . . 35
4.2 Equipment . . . 36
4.2.1 Potentiostat . . . 36
4.2.2 Electrochemical quartz crystal microbalance . . . 36
4.2.3 EC-Lab . . . 37
4.3 Experimental parameters . . . 38

5 Results 41
5.1 Sensitivity analysis using CV-modelling . . . 41
5.1.1 Diffusion Coefficient . . . 41
5.1.2 Initial concentration . . . 42
5.1.3 Charge-transfer coefficient . . . 43
5.1.4 Number of electrons transferred . . . 43
5.1.5 Temperature . . . 44
5.2 Cobalt chloride . . . 45
5.3 Cobalt chloride in nitric acid . . . 47
5.4 Cobalt sulfate . . . 48
5.5 Copper sulfate . . . 48
5.6 Cobalt chloride with copper sulfate . . . 50
5.7 Synthetic samples . . . 53
5.7.1 SD069 . . . 53
5.7.2 SD073 . . . 54
5.8 Mutanda samples . . . 56
5.8.1 18GL3F . . . 58
5.8.2 18GL31 . . . 59
5.8.3 18GL33 . . . 60
5.8.4 18GL35 . . . 62
5.8.5 18GL3D . . . 63
5.8.6 18GL3E . . . 64
5.9 Electrochemical cleaning of electrodes . . . 65

6 Discussion 67
6.1 Sensitivity analysis . . . 67
6.2 Chemical compositions . . . 68
6.2.1 $CoCl_2$ vs. $CoCl_2$ with HNO_3 . . . 68
6.2.2 $CoCl_2$ vs. $CoSO_4$ vs. $CuSO_4$ . . . 69
6.2.3 $CuSO_4$ mixed with $CoCl_2$ . . . 70
6.2.4 Overview . . . 71
6.3 SD069 vs. SD073 . . . 71
6.4 Ores from Mutanda mining operation . . . 72

7 Conclusions and recommendations 75
7.1 Conclusions . . . 75
7.2 Recommendations . . . 77
7.2.1 Recommendations regarding the electrochemical properties and behaviour of copper and cobalt-bearing minerals using CV and EQCM . . . 77
7.2.2 Recommendations for further research . . . 77

Bibliography 79

A Lithostratigraphic units of the KCB 85

B Mineral Mass (%) based on density weighted QEMSCAN analysis. 87

C Analysed Mutanda samples. 89

List of Abbreviations and Symbols

Abbreviations

B-field	Electromagnetic Field
CE	Counter Electrode
CoG^3	Cobalt: Geology, Geomicrobiology and Geometallurgy
CSM	Camborne School of Mines
CV	Cyclic Voltammetry
DRC	Democratic Republic of Congo
EQCM	Electrochemical Quartz Crystal Microbalance
EV	Electric Vehicles
FTIR	Fourier-Transform Infrared Spectroscopy
HER	Hydrogen Evolution Reaction
ICP-AES	Inductively Coupled Plasma Atomic Emission Spectroscopy
KCB	Katanga Copperbelt
Li-on	Lithium-ion Battery
MO	Molecular Orbitals
NHM	Natural History Museum
NiMH	Nickel Metal Hydride Battery
QEMSCAN	Quantitative Evaluation of Minerals by SCANning electron microscopy
RE	Reference Electrode
Redox	Reduction–Oxidation Reaction
SCE	Saturated Calomel Electrode
SHE	Standard Hydrogen Electrode
WE	Working Electrode
WP	Work Package
XRF	X-Ray Fluorescence

Symbols

α	Charge transfer coefficient	-
λ	Switching time	s
A	Surface area of electrode	cm^2
C_O	Concentration gradients for the reactant	M
C_R	Concentration gradients for the product	M
D_0	Diffusion coefficient	$cm^2\,s^{-1}$

E^0	Standard potential	V
E_λ	Switching potential	V
E_i	Initial potential	V
E_p	Peak potential	V
E_p^a	Anodic peak potential	V
E_p^c	Cathodic peak potential	V
$E_{1/2}$	Half-wave potential	V
$E_{p/2}^a$	Anodic half-peak potential	V
$E_{p/2}^c$	Cathodic half-peak potential	V
f	Frequency	Hz
I	Current	A
I_p, i_p	Peak current	A
$I_{p/2}$	Half-peak current	A
j	Current density	$\mathrm{A\,cm^{-2}}$
K	Experimental mass coefficient	$\mathrm{s^{-1}\,g^{-1}}$
k_s or k	Electron transfer rate	$\mathrm{cm\,s^{-1}}$
kg	Kilogram	-
$ktpa$	Kilo tonnes per annum	-
M	Molar mass	$\mathrm{g\,mol^{-1}}$
m	Mass	g
Ma	Mega annum	-
n	Number of electrons involved	-
n_α	Number of electrons transferred before the rate determining step	-
Q	Charge	C
T	Temperature	K
t	Time	s
V	Volt	-
v	Scan rate	$\mathrm{V\,s^{-1}}$
$wt\%$	Weight percentage	%
z	Electrons involved in the reaction	-

Physical Constants

μ_q	Shear modulus of quartz for AT-cut crystal	$2.947 \times 10^{11}\,\mathrm{g\,cm^{-1}\,s^{-2}}$
ρ_q	Density of quartz	$2.648\,\mathrm{g\,cm^{-3}}$
F	Faraday constant	$96\,485\,\mathrm{C\,mol^{-1}}$
R	Gas constant	$8.314\,\mathrm{J\,K^{-1}\,mol^{-1}}$

List of Figures

1.1 EU criticality assessment (EC 2017c) for materials (Tkaczyk et al., 2018) . . . 2
1.2 (a) Global share of Co mining mine production in 2016 in tonnes, (b) Estimated Co reserves in 1000 tonnes (Shedd, 2017) . . . 2
1.3 Refined cobalt demand by end-use and end-use specifications in 2015 (Modified from Darton Commodities, 2016) . . . 3
1.4 World Co mining production, annually from 1960–2015 (USGS, 2019) . . . 3
1.5 Price of Co over time in USD kg^{-1} (dots) and inflation-adjusted USD kg^{-1} (triangles) (Metalary, 2019) . . . 3

3.1 Location of the Mutanda Mining operation within Africa and the DRC (Modified from: Walt and Meyer, 2018) . . . 7
3.2 Geological map of the KCB (Santoro et al., 2019) . . . 8
3.3 Schematic overview of the stratigraphy within the KCB (Dehaine et al., 2017) . . . 8
3.4 Schematic overview of the geology of the Mutanda operation (Modified from: Dehaine et al., 2017) . . . 10
3.5 Lead anodes fitted in the electrochemical cells (Wimberley et al., 2011) . . . 12
3.6 Copper cathode from the heap leach operation (Wimberley et al., 2011) . . . 12
3.7 Schematic overview of (a) reduction and (b) oxidation process of a species A in solution. The molecular orbitals (MO) if species A shown are the highest occupied MO and the lowest vacant MO (Bard and Faulkner, 2001) . . . 14
3.8 Potentials for possible reductions of Fe^{3+}, Cu^{2+}, and Co^{2+} at a platinum electrode (Modified from Bard and Faulkner, 2001) . . . 15
3.9 Pathway of a general electrode reaction (Bard and Faulkner, 2001) . . . 15
3.10 Electrodeposition of a metal layer by a mechanism involving progressive nucleation and growth as hemispherical centres (Modified from Pletcher, 2009) . . . 16
3.11 (a) Cyclic potential sweep. (b) Resulting cyclic voltammogram (Bard and Faulkner, 2001) . . . 18
3.12 Concentration distribution of the oxidised and reduced forms of the redox couple (Wang, 2006) 19
3.13 Voltammogram to define the symbols used in table 3.5 (Pletcher, 2009) . . . 20
3.14 Voltammograms for reversible *(curve a)* and irreversible *(curve b)* redox processes (Wang, 2006) 21
3.15 The transfer coefficient as an indicator of the symmetry of the voltammograms (Harvey, 1999) . 22
3.16 Example of voltammograms at different scan rates of 30, 50, 100, 150, 200, 250, 300 and 400 mV/s (Kasa and Solomon, 1964) . . . 23
3.17 Quartz crystal microbalance: (1) the quartz crystal; (2) the (platinum) electrode; (3,4) connecting metal wires; (5) the base. (Wang, 2006) . . . 24
3.18 Example of an EQCM output presenting a frequency change as a function of time of potential cycling. The applied potential changes are depicted at the top of the figure. The used solution is a 1 M KOH_{aq} solution measured at a scan rate of 20 mV s^{-1} (Grdeń et al., 2009) . . . 24
3.19 Voltammograms for cobalt deposition and stripping in 60 g l^{-1} Co + 30 g l^{-1} boric acid, 20 mV s^{-1} at various temperatures; (1) 20, (2) 40, (3) 50 and (4) 60 °C (Elsherief, 2003) . . . 25
3.20 Voltammograms for cobalt deposition and stripping in various cobalt concentrations + 30 g l^{-1} boric acid, pH 4 solutions at 20 °C and 20 mV s^{-1}. Cobalt conc.: (1) 5, (2) 20, (3) 40 and (4) 60 g l^{-1} (Elsherief, 2003) . . . 27
3.21 B-field relative to the electrode configurations (Krause et al., 2004) . . . 28
3.22 Voltammograms for cobalt deposition and stripping in 60 g/l Co + 30 g/l boric acid, in presence of various (a) zinc, (b) copper and (c) iron concentrations at 100 mV/s, 20 °C (Elsherief, 2003) . . 29
3.23 Effect of changing different parameters *(a, b, c)* within graphical CV simulation (Brown, 2015) . 30
3.24 Snapshots of diffusion profiles for the reversible electron transfer reaction at 32.7 mV (when the peak currents occur): (a) scan rate = 1 V/ s; (b) scan rate = 0.1 V/s (Wang et al., 2017) . . . 31

4.1 Schematic representation of an electrochemical cell for cyclic voltammetry experiments (Rountree et al., 2018) 33
4.2 Schematic overview of the used reference Ag/AgCl electrode (Rountree et al., 2018) 34
4.3 Standard type platinum working electrode 35
4.4 Platinum counter electrode 35
4.5 Small size Ag/AgCl reference electrode with 3 M NaCl electrolyte 35
4.6 Schematic overview of how to polish a working electrode correctly (Rountree et al., 2018) 35
4.7 Bio-Logic SP-200 potentiostat 36
4.8 Schematic diagram of a three-electrode setup (Wang, 2006) 36
4.9 Seiko EG&G Quartz Crystal Microbalance (EQCM) 36
4.10 Schematic diagram of a three-electrode potentiostat including the EQCM (Modified from: Wang, 2006) 36
4.11 Schematic representation of the setup for a EQCM measurement (Modified from: Princeton Applied Research, 2007) 37
4.12 Bio-Logic EC-Lab software including a CV-curve 38
4.13 External device configuration window 38
4.14 Extraction percentages for cobalt, iron and nickel for different (a) temperatures, (b) reaction times and (c) HNO_3 concentrations (Modified from Gürmen and Friedrich, 2004) 39

5.1 Modelled cyclic voltammograms for different values of the diffusion coefficient (D) 42
5.2 Cathodic peak current (V_{min}) vs. diffusion coefficient (D). X-axis is displayed as logarithmic scale 42
5.3 Modelled cyclic voltammograms for different values of the initial concentration (C_O) 42
5.4 Cathodic peak current (V_{min}) vs. initial concentration (C_O) 42
5.5 Modelled cyclic voltammograms for different values of the charge-transfer coefficient (α) 43
5.6 Cathodic peak current (V_{min}) vs. charge-transfer coefficient (α) 43
5.7 Modelled cyclic voltammograms for different values of the number of transferred electrons (n) 44
5.8 Cathodic peak current (V_{min}) vs. number of transferred electrons (n) 44
5.9 Modelled cyclic voltammograms for different values of the temperature (T) 44
5.10 Cathodic peak current (V_{min}) vs. temperature (T) 44
5.11 Single voltammogram using 0.05 M $CoCl_2$ at 298K, $\nu = 50$ mVs^{-1} 45
5.12 Voltammogram for 0.05 M $CoCl_2$ at 298 K under different scan rates at pH of 5.80 45
5.13 Cathodic peak current densities of voltammogram for 0.05 M $CoCl_2$ at 298 K under different scan rates 45
5.14 Cyclic voltammogram (—) for 0.05 M $CoCl_2$ solution and corresponding frequency change (—) 46
5.15 Cyclic voltammogram (—) for 0.05 M $CoCl_2$ solution and corresponding mass change (—) 46
5.16 Frequency variation as a function of charge 47
5.17 Cyclic voltammogram using a 0.05 M $CoCl_2$ in 0.5 M HNO_3 at 298 K under different scan rates 47
5.18 Cathodic peak current densities of voltammogram in 0.05 M$CoCl_2$ in 0.5 M HNO_3 at 298 K 47
5.19 Cyclic voltammogram (—) for 0.5 M $CoCl_2$ solution in 0.5 M HNO_3 and corresponding mass change (—) 48
5.20 Cyclic voltammogram of 0.1 M $CoSO_4$ for varying scan rates between 40 and 120 mV/s at 298 K 48
5.21 Cathodic peak current densities of CV curve for 0.05 M $CoSO_4$ at 298 K for different scan rates 48
5.22 Cyclic voltammogram of 0.1 M $CuSO_4$ for varying scan rates between 40 and 120 mV/s at 298 K 49
5.23 Cathodic peak current densities of CV curve for 0.05 M $CuSO_4$ at 298 K for different scan rates 49
5.24 Cyclic voltammogram of 0.1 M $CuSO_4$ in 0.5 M HNO_3 for varying scan rates between 40 and 80 mV/s at 298 K 49
5.25 Voltammogram for 0.05 M $CuSO_4$ and 0.05 M $CoCl_2$ for scan rates between 40 and 120 mV/s at pH 5.6 50
5.26 Cathodic peak current densities of CV curve for 0.05 M $CuSO_4$ and 0.05 M $CoCl_2$ at pH 5.6 50
5.27 Voltammogram for 0.05 M $CuSO_4$ and 0.05 M $CoCl_2$ for scan rates between 40 and 120 mV/s at 298 K at pH 1.5 50
5.28 Cathodic peak current densities of CV curve for 0.05 M $CuSO_4$ and 0.05 M $CoCl_2$ at pH 1.5 50
5.29 Cyclic voltammogram (—) for 0.05 M $CuSO_4$ and 0.05 M $CoCl_2$ at pH 5.60 and corresponding curve for Δf (—) 51
5.30 Cyclic voltammogram (—) for 0.05 M $CuSO_4$ and 0.05 M $CoCl_2$ at pH 1.50 and corresponding curve for Δm (—) 51

5.31 CV (—) for SD069 synthetic sample in 0.5 M HNO_3 at pH 5.60 and corresponding curve for Δm (—) . . . 53
5.32 CV (—) for SD069 synthetic sample in 0.5 M HNO_3 at pH 1.10 and corresponding curve for Δm (—) . . . 53
5.33 CV (—) for SD069 synthetic sample in 0.5 M HNO_3 at pH 5.60 and corresponding curve for Δm (—) after 12 cycles . . . 54
5.34 CV (—) for SD069 synthetic sample in 0.5 M HNO_3 at pH 1.10 and corresponding curve for Δm (—) after 6 cycles . . . 54
5.35 CV (—) for SD073 synthetic sample in 0.5 M HNO_3 at pH 5.60 and corresponding curve for Δm (—) . . . 55
5.36 CV (—) for SD074 synthetic sample in 0.5 M HNO_3 at pH 1.10 and corresponding curve for Δm (—) . . . 55
5.37 CV (—) for SD073 synthetic sample in 0.5 M HNO_3 at pH 5.60 and corresponding curve for Δm (—) after 12 cycles . . . 56
5.38 CV (—) for SD073 synthetic sample in 0.5 M HNO_3 at pH 1.10 and corresponding curve for Δm (—) after 12 cycles . . . 56
5.39 Overview of the used samples for the experiments in this section . . . 56
5.40 Mineral mass for the six chosen samples from the Mutanda mining operation with an increasing grade of cobalt-bearing Carrolite and Heterogenite . . . 57
5.41 Voltammogram for 0.75 g 18GL3F in 0.5 M HNO_3 for scan rates between 40 and 120 mV/s at 298 K at pH 1.1 . . . 58
5.42 Cathodic peak current densities of CV curve for 0.75 g 18GL3F in 0.5 M HNO_3 at pH 1.1 . . . 58
5.43 Cyclic voltammogram (—) for 18GL3F sample in 0.5 M HNO_3 at pH 1.10 and corresponding curve for Δm (—) . . . 59
5.44 Voltammogram for 0.75 g 18GL31 in 0.5 M HNO_3 for scan rates between 40 and 120 mV/s at 298 K at pH 1.1 . . . 59
5.45 Anodic peak current densities of CV curve for 0.75 g 18GL31 in 0.5 M HNO_3 at pH 1.1 . . . 59
5.46 Cyclic voltammogram (—) for 18GL31 sample in 0.5 M HNO_3 at pH 1.20 and corresponding curve for Δm (—) . . . 60
5.47 Voltammogram for 0.75 g 18GL33 in 0.5 M HNO_3 for scan rates between 40 and 120 mV/s at 298 K at pH 1.1 . . . 61
5.48 Cathodic peak current densities of CV curve for 0.75 g 18GL33 in 0.5 M HNO_3 at pH 1.1 . . . 61
5.49 Cyclic voltammogram (—) for 18GL33 sample in 0.5 M HNO_3 at pH 1.10 and corresponding curve for Δm (—) . . . 61
5.50 Voltammogram for 0.75 g 18GL35 in 0.5 M HNO_3 for scan rates between 40 and 120 mV/s at 298 K at pH 1.1 . . . 62
5.51 Cathodic peak current densities of CV curve for 0.75 g 18GL35 in 0.5 M HNO_3 at pH 1.1 . . . 62
5.52 Cyclic voltammogram (—) for 18GL35 sample in 0.5 M HNO_3 at pH 1.10 and corresponding curve for Δm (—) . . . 63
5.53 Voltammogram for 0.75 g 18GL3D in 0.5 M HNO_3 for scan rates between 40 and 120 mV/s at 298 K at pH 1.1 . . . 63
5.54 Cathodic peak current densities of CV curve for 0.75 g 18GL3D in 0.5 M HNO_3 at pH 1.1 . . . 63
5.55 Cyclic voltammogram (—) for 18GL3D sample in 0.5 M HNO_3 at pH 1.10 and corresponding curve for Δm (—) . . . 64
5.56 Voltammogram for 0.75 g 18GL3E in 0.5 M HNO_3 for scan rates between 40 and 120 mV/s at 298 K at pH 1.1 . . . 65
5.57 Cathodic peak current densities of CV curve for 0.75 g 18GL3E in 0.5 M HNO_3 at pH 1.1 . . . 65
5.58 Cyclic voltammogram (—) for 18GL3E sample in 0.5 M HNO_3 at pH 1.10 and corresponding curve for Δm (—) . . . 65
5.59 Cyclic voltammogram for a clean 0.5 M HNO_3 solution . . . 66
5.60 Cyclic voltammogram (—) for 0.5 M HNO_3 cleaning solution and corresponding frequency change (—) . . . 66
5.61 Peak potentials for all cycles shown in figure 5.60. . . . 66

6.1 Cyclic voltammogram 0.05 M $CoCl_2$ for pH 5.80 and 1.70 shown in figures 5.12 and 5.17. The scan rate was 100 mVs^{-1} . . . 69

6.2 Cyclic voltammogram 0.05 M $CoCl_2$, 0.05 M $CoSO_4$ and 0.05 M $CuSO_4$. The scan rate was 100 mVs^{-1} for all solutions . . . 69
6.3 Cyclic voltammogram 0.05 M $CoCl_2$ mixed with 0.05 M $CuSO_4$. The scan rate was 50 mVs^{-1} . . . 70
6.4 Voltammogram for SD069 and SD073 synthetic samples is 0.5 M HNO_3 for pH 5.60, where ν = 50 mVs^{-1} . . . 72
6.5 Voltammogram for SD069 and SD073 synthetic samples is 0.5 M HNO_3 for pH 1.10, where ν = 50 mVs^{-1} . . . 72
6.6 Cyclic voltammogram of 0.75 g of DRC-ore in 0.5 M HNO_3 with ν = 50 mVs^{-1} . . . 73

List of Tables

3.1 ICP-AES results for Co, Cu, Fe and Mn prior and after leaching tests. The results reported are the mean of the values for each element (Santoro et al., 2019) 10
3.2 Mineral resources of the total Mutanda project on 31 December 2018 (Glencore, 2018) 11
3.3 Mineral reserves of the total Mutanda project on 31 December 2018 (Glencore, 2018) 11
3.4 Limited overview of Co and Cu standard reduction potentials E^0 (Vanysek, 2010) 13
3.5 Tests for the the form of cyclic voltammetric responses for a reversible and irreversible couple at 298 K (Pletcher, 2009) 21
3.6 Characteristic M/z values for reactions used for this thesis 24

5.1 M/z found by fitting the slope of the frequency versus charge for cobalt deposition of $CoCl_2$ solution at pH= 5.80 47
5.2 M/z values for cobalt deposition of 0.05 M $CoCl_2$ added with HNO_3 up to pH = 1.70 48
5.3 M/z for 0.05 M $CoCl_2$ and 0.05 M $CuSO_4$ solution at pH = 5.60 using chronoamperometry for constant potentials of 0.50 V, -0.30 V and -1.10 V 52
5.4 M/z for 0.05 M $CoCl_2$ and 0.05 M $CuSO_4$ solution at pH = 5.60 52
5.5 M/z for 0.05 M $CoCl_2$ and 0.05 M $CuSO_4$ solution at pH = 1.50 52
5.6 Overview of the synthesis of the synthetic samples 53
5.7 M/z for SD069 in 0.5 M HNO_3 solution at pH = 5.60 54
5.8 M/z for SD069 in 0.5 M HNO_3 solution at pH = 1.10 54
5.9 M/z for SD073 in 0.5 M HNO_3 solution at pH = 5.60 55
5.10 M/z for SD073 in 0.5 M HNO_3 solution at pH = 1.10 55
5.11 Overview of mineral mass (%) of the analysed samples from the Mutanda mining operation . . 57
5.12 Peak characteristics for the 18GL3F sample 58
5.13 M/z for 18GL3F sample in 0.5 M HNO_3 solution at pH = 1.10 59
5.14 Peak characteristics for the 18GL31 sample for v = 100 mV/s 59
5.15 M/z for 18GL31 sample in 0.5 M HNO_3 solution at pH = 1.10 60
5.16 Peak characteristics for the 18GL33 sample 60
5.17 M/z for 18GL33 sample in 0.5 M HNO_3 solution at pH = 1.10 61
5.18 Peak characteristics for the 18GL35 sample 62
5.19 M/z for 18GL35 sample in 0.5 M HNO_3 solution at pH = 1.10 63
5.20 Peak characteristics for the 18GL3D sample 63
5.21 M/z for 18GL3D sample in 0.5 M HNO_3 solution at pH = 1.10 64
5.22 Peak characteristics for the 18GL3E sample 64
5.23 M/z for 18GL3E sample in 0.5 M HNO_3 solution at pH = 1.10 65

6.1 Overview of the minimum and maximum current densities combined with evaluated parameter 68
6.2 Overview of diffusion coefficient of Co(II) in various electrolyte solutions (modified from: Li et al., 2014) 71
6.3 Overview of values for α, D, k_s and Δm obtained from experiments using the Mutanda ores . . . 73

1

Introduction

Metal extraction takes place all around the globe, but the complexity of this extraction is increasing every year. Within the metal extraction process, electrochemical reactions will become more important than before, due to the complexity of the mineral deposits that need to be mined. Except for iron alloys and recycled materials, electrochemical reactions are also used in producing much of the world's metals. Iron, aluminium and copper are the major metals that are produced partially by electrolytic processes, but other such metals include cadmium, chromium, cobalt, lithium, manganese, magnesium, nickel and zinc (Evans, 2015).

Electrolytic processes reduce metal forms using an applied voltage, an anode at which oxidation takes place, and a cathode at which the metal is reduced to its metallic state (Free and Moats, 2015). By performing multiple experiments on the electrochemical behaviour of minerals, their ideal electroplating parameters can be obtained to use for the use of selective electrowinning. This thesis investigates the electrochemical behaviour of cobalt-bearing solutions and minerals.

1.1. Cobalt

Cobalt is a chemical element and a hard lustrous bluish grey metal. It has the chemical abbreviation Co and atomic number 27 in the periodic table. Cobalt is a transition metal and is typically found in the earth as an alloy, which indicates that it is joined with another metal. Cobalt minerals have been used as pigments for thousands of years. This was the only use of cobalt until the 20th century (Crundwell et al., 2011). It was isolated for the first time in the 1730s and recognised as an element in 1780 (Commodity Research Bureau, 2005). Nowadays, the interest focuses on properties like its ductility, strength and heat resistance, which makes it suitable for a wide variety of industrial and military applications (Hannis et al., 2009).

Currently, the European Union (EU) has identified cobalt as a critical element. This is based on the economic importance of the element, which indicates the importance of the raw material, the consequent impact of supply shortfalls, and the supply risk, which indicates the likelihood of the occurrence of such disruptions (Tkaczyk et al., 2018). For several elements, the economic importance versus the supply risk is presented in figure 1.1. Cobalt can be seen at a supply risk of 1.6 and a economic importance of 5.7.

1.1.1. Production and reserves

Since the importance of cobalt is increasing, the production of cobalt has increased rapidly since 1960. As can be seen in figure 1.4, a general increase in cobalt mining can be seen from 1960 until 1986. Afterwards, in the mid-1990s, there was a decreased production which ended in 1994 with 18,000 t. This was followed by a seven-fold increase to 126,000 in 2015. With an increasing demand for cobalt, the prices are likely to adapt to this. As can be seen in figure 1.5, there have been multiple price fluctuations for cobalt. Here, the real price and inflation corrected price for 2017 can be seen. The highest peak occurred in 1979, with a price of 250 USD/kg. As of September 2019, the price has hit its highest level since 2008, the most recent peak has been prompted by rising demand of electric cars and the prospect of higher taxes in the DRC (Sanderson, 2019).

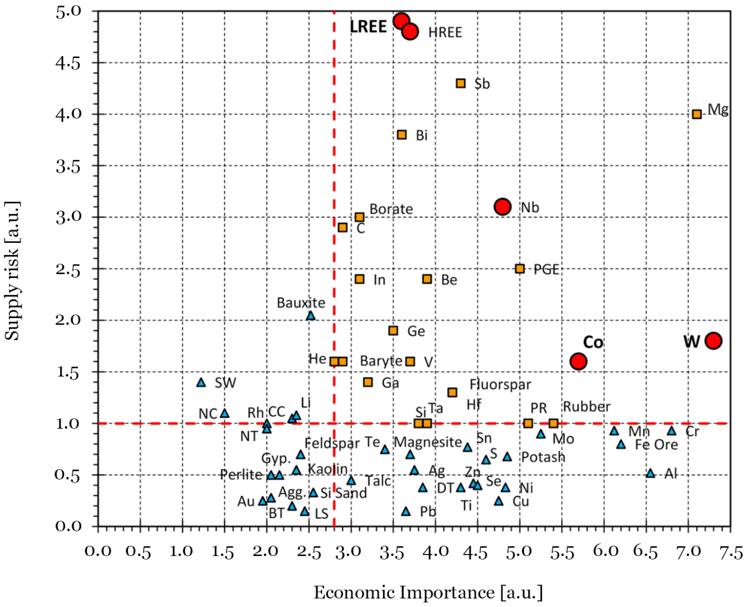

Figure 1.1: EU criticality assessment (EC 2017c) for materials (Tkaczyk et al., 2018)

In the EU, the production of cobalt ores and concentrates was estimated at 2,300 tonnes in 2016 (WMD, 2018), which is 2% of the total world production of cobalt. These ores were all sourced from Finland. However, other projects at an early developing stage can be found in Finland, Sweden, Cyprus, Slovakia, Austria, Czech Republic, Germany, Italy and Poland (Alves Dias et al., 2018). Over the period 2010-2014, circa 48% of the imported cobalt originated form DRC, which indicates that the European share is still fairy low.

The vast majority of cobalt is mined in the DRC. According to Tkaczyk et al. (2018), in 2016, the country accounted for 54% of the global cobalt mining production. Furthermore, circa half of the total reserves of cobalt are situated in the DRC. The countries with the highest number of mines and late-stage exploration projects are Australia (49), Canada (33) and DRC (17) (Alves Dias et al., 2018). Figure 1.2 gives an overview of the current production and the estimated reserves.

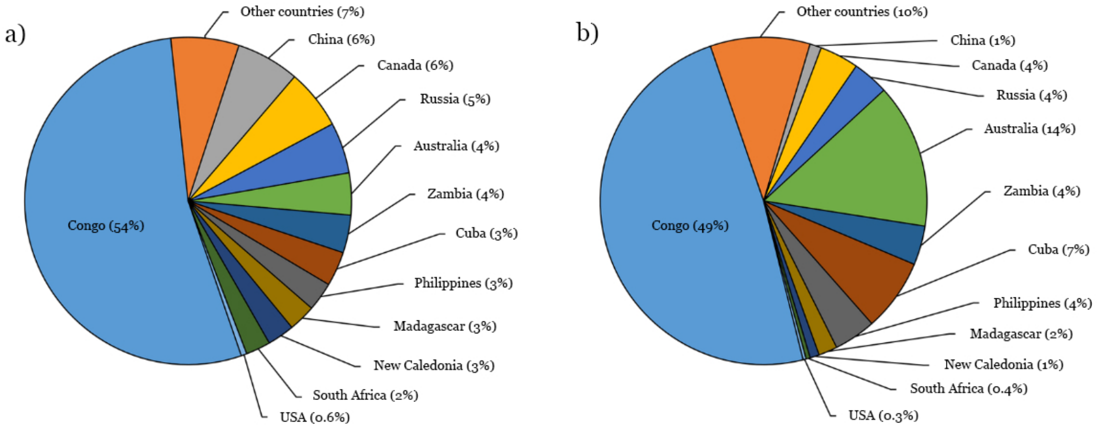

Figure 1.2: (a) Global share of Co mining mine production in 2016 in tonnes, (b) Estimated Co reserves in 1000 tonnes (Shedd, 2017)

1.1.2. Use

According to Alves Dias et al. (2018), in 2016, the global demand for refined cobalt was around 98,000 tonnes. This amount has almost tripled since the beginning of 2000. The main use is as battery chemicals (Li-ion and NiMH), superalloys (aerospace and medical) and hardmetals (cutting tools and mining). Figure 1.3 gives an overview of the current cobalt consumption.

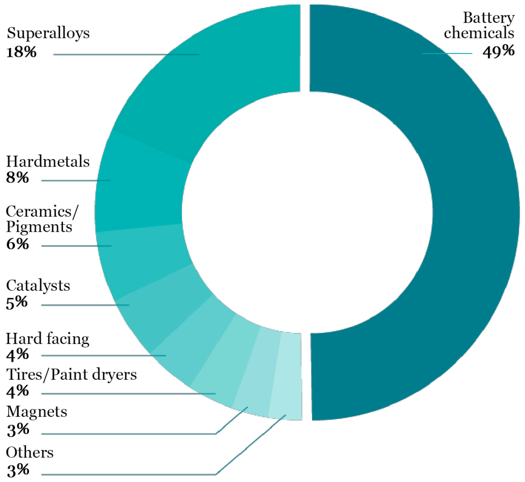

Figure 1.3: Refined cobalt demand by end-use and end-use specifications in 2015 (Modified from Darton Commodities, 2016)

1.1.3. Occurrence

Cobalt is typically mined as a byproduct of copper, nickel and iron and is widely distributed in different mineral deposits including sulphides, sulphosalts, arsenides, oxides and carbonates (Cheang and Mohamed, 2016). In general, cobalt can mainly be found within sulfide or laterite ores (Crundwell et al., 2011). Circa 25% of the primary production of cobalt is from sulfide ores, here the cobalt element is specifically found in nickel sulfide ores. The most common mineral is pentlandite, $(Ni,Fe,Co)_9S_8$, which is the most common variant of of nickel sulfide mineral. The average cobalt content of pentlandite is about $1.1 \pm 0.3\%$ (Crundwell et al., 2011). A quarter of the primary production of cobalt is generated by laterite ores. This indicates that it is always present in the unlaterised precursors of igneous rock (Freyssinet et al., 2005). The cobalt in these ores is available as the ghoethite mineral, chemically known as (Fe,Ni,Co)OOH.

Geographically, the ores of the Central African Copperbelt in the Democratic Republic of Congo (DRC) and Zambia contain the vastest amount of cobalt. About half the world's production originates in this region. The main mineral found in this region is carrollite, $CuCo_2S_4$, which is present together with chalcocite, Cu_2S, and digenite, Cu_9S_5 (Crundwell et al., 2011). The overall grade of the deposit typically contains 0.3% cobalt and circa 3% copper.

1.1.4. Price

With a fluctuating demand for cobalt, the prices are likely to adapt to this. As can be seen in figure 1.5, there have been multiple price fluctuations for cobalt. Here, the real price and inflation corrected price for 2017 can be seen. The highest peak occurred in 1979, with a price of 250 USD/kg. As of September 2019, the price has hit its highest level since 2008, the most recent peak has been prompted by rising demand of electric cars and the prospect of higher taxes in the DRC (Sanderson, 2019).

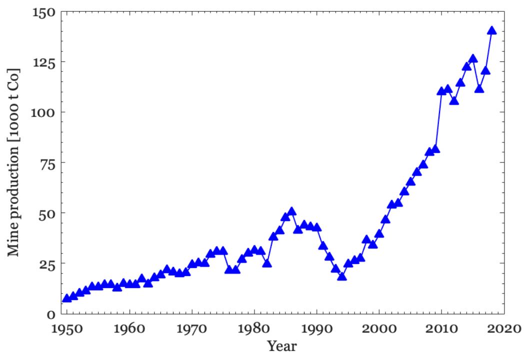

Figure 1.4: World Co mining production, annually from 1960–2015 (USGS, 2019)

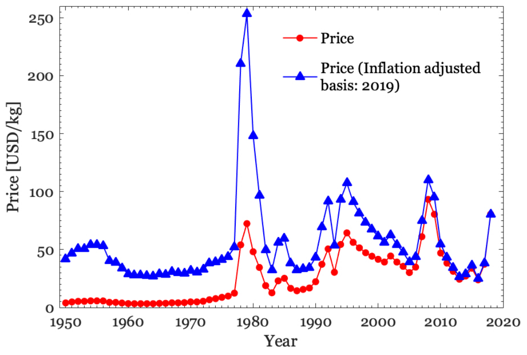

Figure 1.5: Price of Co over time in USD kg^{-1} (dots) and inflation-adjusted USD kg^{-1} (triangles) (Metalary, 2019)

1.2. CoG3 project

This study is part of a larger project named: "Cobalt: Geology, Geomicrobiology, Geometallurgy (CoG^3)". This is a multi-institute and multi-investor consortium with internationally recognised expertise across the geosciences including geology, geochemistry, mineralogy, microbiolology and bioprocessing (UK Research and Innovation, 2017). The main objective of the project is to understand the natural behaviour and (bio)chemistry of cobalt in order to develop and apply new strategies for cobalt extraction and recovery. The goal of the project is to increase the United Kingdom's exploration, mining and recovery of cobalt. Circa 126,000 tonnes of cobalt are produced globally each year, but less than 2.0% of this is produced within Europe, yet European countries use around 30% of the globally produced cobalt (Natural History Museum, 2017).

Overall, the project has the ambitious plans of providing (UK Research and Innovation, 2017):

1. New geological and mineralogical knowledge from existing and potential deposits of cobalt, that will underpin new, more efficient exploration and mining activities
2. A clearer understanding of the natural biochemical cycle of cobalt, better defining the pathways that make and break cobalt-bearing compounds in natural systems
3. An assessment of a range of bioprocessing pathways, at a range of scales, in both reduced and oxidised ore systems, targeted towards more benign bio-recovery methods for cobalt
4. Insights into new methods capable of (bio)engineering compounds, for use by the broader the downstream cobalt user community.

To deliver on these plans, the CoG^3-project is based upon four integrated work packages (WP), each accountable for a different aim. As can be seen, the University of Exeter is heading work package four (WP4):

WP1: The new sources of cobalt (Natural History Museum)

WP2: Natural bio-geochemistry of cobalt (University of Manchester)

WP3: Bio-processing of cobalt (University of Bangor)

WP4: Improving the supply chain of cobalt (University of Exeter)

The research of work package four focuses on improving the supply chain of cobalt through investigation into the geometallurgy of cobalt with direct engagement of the industry. WP4 will integrate the results of WP1, WP2 and WP3 with a view to refine and extend the geometallurgical modelling of cobalt recovery. In the end, this will provide a valuable insight into where future cobalt supplies may be recovered, using more sustainable processing methods (Natural History Museum, 2017).

1.3. Electrochemistry

A more sustainable and cost-effective processing method could be by implementing electrochemical processes, to improve the supply chain of cobalt, which is linked to work package four. Electrochemistry involves the study of the chemical processes and the relationship between electrical and chemical effects that cause electrons to move. When such a movement occurs, electricity is generated. This movement of electrons from one element to another is a reaction known as an reduction-oxidation (redox) reaction. Overall, it offers a wide range of applications and different phenomena, (e.g. electrophoresis and corrosion), devices (electrochromic displays, electroanalytical sensors, batteries, and fuel cells), and technologies (the electroplating of metals and the large-scale production of for example aluminium and chlorine) (Bard and Faulkner, 2001).

Currently, due to their importance in many (industrial) applications, the iron group metals (Fe, Co and Ni) have undergone a lot of investigation concerning their electrochemical behaviour in aqueous solutions. However, the electrochemical behaviour of cobalt has still not been thoroughly investigated, and the obtained results are contradictory and not single minded (Badawy et al., 2000). With the increasing demand of cobalt, due to its indispensability for lithium-ion batteries (LIB) used in electric vehicles (EV) and stationary energy storage (Alves Dias et al., 2018), initiatives have been started to secure reliable and unhindered access to the raw materials. Therefore, further investigation is needed to learn more about the electrochemical behaviour of cobalt to gain a better understanding of the electrowinning, which is the electrodeposition of metals from their ores that have been put in solution via a process commonly referred to as leaching. The theory and used methods of electrochemistry will by explained in chapter 3.

2

Research approach

In this chapter, the scope of the research will be given, therewith providing the layout of the report. As a result of the problem definition, a research objective will be set. In order to reach this objective, multiple research questions are presented. The research in this thesis is aimed at answering these questions and they are used as a general thread throughout the remainder of this thesis. In the last part of the research approach, the scope and methodology are explained briefly.

2.1. Problem definition

Camborne School of Mines (CSM) is involved in the research and scientific investigation of cobalt within the "Cobalt: the roles of Geology, Geomicrobiology and Geometallurgy (CoG^3)" consortium. The project focuses on investigating different solutions for recovery of cobalt, leading to new product streams.

As mentioned in the introduction, nowadays, Cobalt is mostly mined as byproduct of copper winning in general mining, especially in the Democratic Republic of Congo (DRC). One of the primary difficulties facing cobalt recovery from sulphide ores relates to its flotation when using conventional processes. In an attempt to overcome these difficulties, processing companies are using increasingly complex chemical additives. The toxicity of these chemicals increases the potential environmental risk of the process, both in terms of volatilisation and leakage into the surroundings.

To avoid these difficulties, other methods of cobalt recovery are being investigated, including electrowinning opportunities. Should other recovery methods be examined, then several experiments are needed to investigate the electrochemical behaviour of cobalt in solutions. So far, the majority of the studies on cobalt have focused on non-electrowinning possibilities. Therefore it is of interest to investigate the electrochemical behaviour within different environments.

2.2. Objective

The main objective for this research is stated as follows:

> *Investigate what causes the differences in the electrochemical behaviour of copper-cobalt minerals in aqueous solutions using chemical compositions, synthetic and real ores, and find a correlation between the obtained results using the graphs generated using CV and EQCM-techniques.*

To be able to answer this objective, first a literature review is carried out to evaluate the Mutanda mining operation and the environment in which the used samples are mined. This is followed by the evaluation of the electrochemical processes, the theory behind the CV and EQCM techniques, the effects on the electrochemical behaviour of cobalt, simulated CV measurements and electrochemical mechanisms occurring with cobalt deposition. Then the experimental setup used for this research will be discussed, including the parameters used for the experiments in this thesis, where after the results of the experiments are presented together with a discussion and the conclusion.

2.3. Research questions

In order to reach the objective set for this research, five research questions are proposed to provide guidance throughout the project. These research questions are:

1. How do different electrochemical properties influence the electrochemical behaviour of cobalt in solutions using cyclic voltammetry simulations?
2. What are the most important electrochemical properties of multiple cobalt-bearing solutions, investigated with the help of cyclic voltammetry (CV) and the electrochemical quartz crystal microbalance (EQCM)?
3. Can selective electrodeposition be applied, so reduction and/or deposition is possible so other elements than cobalt (Co), such as copper (Cu) and iron (Fe), can be gained in the same solution by using their characteristic reduction potentials?
4. What is the influence of a varying mineralogy and mineral structure on the electrochemical behaviour of the cobalt-bearing ores and the shape of the corresponding voltammogram?
5. Is it possible to find a correlation between the electrochemical properties of chemical compositions, the synthetic iron-cobalt ore and the cobalt-bearing samples from the DRC?

2.4. Scope

This thesis focuses on the electrochemical behaviour and deposition of cobalt-bearing minerals, which will be evaluated with the help of cyclic voltammetry (CV) and the electrochemical quartz crystal microbalance (EQCM). These techniques use the help of multiple variable input parameters, which will be investigated and compared to gain the optimised condition to perform the experiments. Furthermore, the sensitivity of the techniques to different input parameters and different solutions will be investigated.

During the experiments using CV and EQCM, cobalt is electroplated on the electrode. Once the electrochemical reaction is finished, the electroplated material will be analysed using the EQCM technique to investigate which electrochemical reactions happen inside the electrolyte solution. These techniques will be evaluated in section 3.

2.5. Methodology

In order to answer the research questions, this study will conduct a literature review including an overview of the mining activities of the Mutanda mining operation, the source for the cobalt-bearing samples used in this study. The next section of the literature review will focus on the electrochemical behaviour of cobalt within a broad spectrum, especially for CV and EQCM results. After that, the principles behind the different electrochemical and characterisation techniques will be explained.

Then, the experimental setup used for the electrochemical experiments will be discussed to gain understanding of the specialised equipment and corresponding software used for gathering the data. Two synthetic cobalt-bearing solutions will be tested. With the help of CV the electrochemical behaviour, e.g. redox-reactions, can be analysed. Using the EQCM, accurate measurements of the mass change per unit area of the electroplated cobalt will be recorded. Synthetic minerals will be used to know how much can be recovered using this technique. Finally, samples from the DRC will be used to obtain the same data as for the synthetic minerals where QEMSCAN data is used to evaluate the mineral composition.

With the obtained results, the reaction mechanisms in multiple cobalt-bearing solutions will be compared and the best electroplating potential can be determined for a particular solution. The overall goal is to investigate the electrochemical properties of several cobalt-bearing solutions and indicate if there is a linkage between the obtained data of the synthetic minerals and the DRC-samples. In order to determine this correlation, the obtained results will be analysed and discussed, after which conclusions can be drawn and recommendations can be made.

3

Literature review

This chapter evaluates the Mutanda Mining operation the Democratic Republic of Congo (DRC) together with the fundamentals of the electrochemical methods, the principles of the used characterisation methods and the current applications for these methods.

For the Mutanda mining operation, the regional and local geology are evaluated, which indicate the origin of the ores used in this thesis. Next, the overall mineral resources and ore reserves are discussed, as well as the current electrowinning procedure. Next, the current approach and thoughts on the electrochemical behaviour of cobalt is evaluated, discussing what subjects are on agreement and which ones are still in division and (modelled) cyclic voltammetry and the electrochemical quartz crystal microbalance are discussed. With the results of the literature review, different scenarios for electrochemical experiments can be created.

3.1. Mutanda mining operation

The Mutanda mining project is located in the southern part of the DRC. The area is located circa 40 kilometres to the southeast of the town of Kolwezi in the Haut-Katanga province (see figure 3.1). The mining project has been fully owned by Glencore International since the end of 2017 (Kruger, 2017). The deposit is situated within the Central African Copper Belt that runs through northern Zambia and the southern parts of the DRC, and is host to one of the world's largest concentrations of sediment-hosted stratiform Copper-Cobalt mineralisation (Herman and Beverley, 2016).

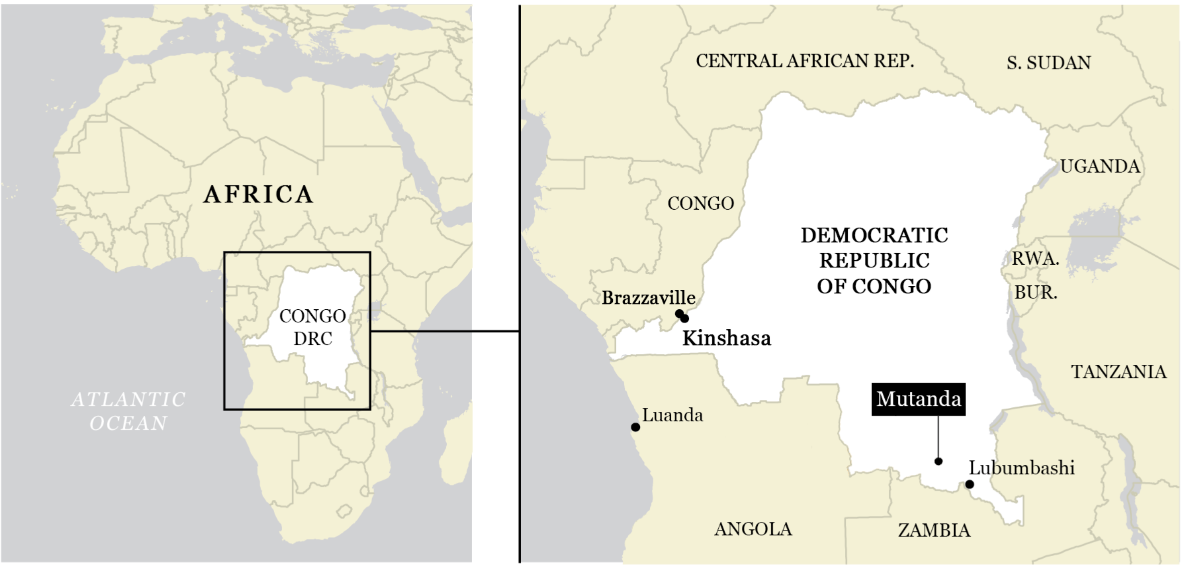
AFRICA
CONGO DRC
ATLANTIC OCEAN
CENTRAL AFRICAN REP.
S. SUDAN
UGANDA
CONGO
DEMOCRATIC REPUBLIC OF CONGO
RWA.
BUR.
Brazzaville
Kinshasa
TANZANIA
Mutanda
Luanda
Lubumbashi
ANGOLA
ZAMBIA

Figure 3.1: Location of the Mutanda Mining operation within Africa and the DRC (Modified from: Walt and Meyer, 2018)

The production capacity of the Mutanda Mining project is circa 2000 kilo tonnes per annum (ktpa) copper cathodes and 23 ktpa contained cobalt in hydroxide form as $Co(OH)_2$. The ore has been extracted since 2008, and the expected life of the mine is approximately more than 20 years (Glencore, 2013). In 2015, Mutanda produced 216,100 tonnes of copper and 16,500 tonnes of cobalt, more than any other mine in the DRC. The operation is considered one of Glencore's main growth assets and a key operation in the DRC, largely thanks to its high ore grades and low expansion costs (Jamasmie, 2017).

3.1.1. Regional geology

The Neoproterozoic Katanga Supergroup, a name for this mineral group within the DRC, hosts one of the world's greatest concentrations of sediment-hosted copper-cobalt deposits. The sedimentary succession is assumed to be roughly 7.5 km thick where it has been deposited on the Archean-Paleoproterozoic basement of the Congo Craton(François, 1987). The mineralised levels occur in the sedimentary sequences of the Mines Subgroup of the Roan Group. The copper belt extends for about 450 kilometres and is 260 kilometres in width. Mineralisation is hosted in a variety of rocks and fluid traps, and emplaced by a number of events spread over a period of 200 Ma. containing about 34% of global cobalt reserves, and more than 10% of the global copper reserves (Mbendi, 2005).

The Mutanda copper-cobalt deposit is part of a thrust-and-fold belt known as the Lufilian Arc and part of the Central African Copper belt, where it has the same characteristics as most of the deposits within the Copperbelt in that it is stratiform and associated with carbonate or carbon-rich lithologies (Cailteux et al., 2005). The Katanga Supergroup succession is interpreted as a result of the opening of an intracontinental rift basin between the Congo and Kalahari cratons, which is an old and stable part of the continental lithosphere. This all happened during the Rodinina Supercontinent break-up one million billion years ago. Later, the basin closed, due to convergence between these two cratons. This convergence led to the development of a fold-and-thrust belt which was tectonically transported to the north, detaching the Katanga sedimentary pile from the base (Cailteux and De Putter, 2019).

The Katanga Supergroup sequence is subdivided into multiple groups based on their lithological characteristics. It was first subdivided by who François (1973) into three groups; the Roan (R), Nguba (Ng) (*former Lower Kundelungu*) and Kundelungu (Ku) (*former Upper Kundelungu*). The Roan group is a sedimentary succesion which is affected by many structural dislocations and occurs mainly as fragments and finely ground material within tectonic megabreccias. The conglomerate is interpreted as the base of the Roan in the Katanga Copperbelt (KCB). The Nguba and Kundelungu groups are similar sedimentary groups characterised by diamictites at the bottom with overlying carbonates, followed by predominantly siliclastic sedimentary rocks at the top (Cailteux and De Putter, 2019).

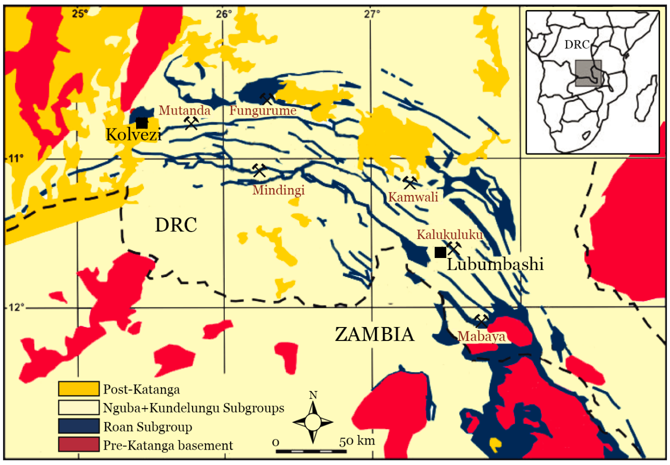
25°
26°
27°
DRC
Mutanda
Fungurume
Kolwezi
11°
Mindingi
Kamwali
DRC
Kalukuluku
Lubumbashi
12°
ZAMBIA
Mabaya
Post-Katanga
Nguba+Kundelungu Subgroups
Roan Subgroup
Pre-Katanga basement
N
0
50 km

Figure 3.2: Geological map of the KCB (Santoro et al., 2019)

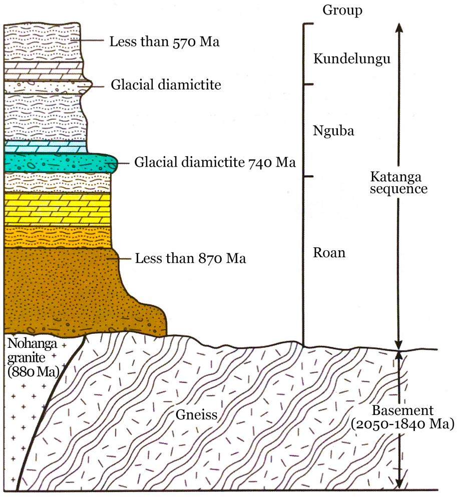
Group
Less than 570 Ma
Kundelungu
Glacial diamictite
Nguba
Glacial diamictite 740 Ma
Katanga sequence
Less than 870 Ma
Roan
Nohanga granite (880 Ma)
Gneiss
Basement (2050-1840 Ma)

Figure 3.3: Schematic overview of the stratigraphy within the KCB (Dehaine et al., 2017)

For the Mutanda Mining project location, the Roan group is of most importance, since the Mutanda deposit is located within a small thrust of this group (Herman and Beverley, 2016). For this reason, this group will be discussed more extensively. An overview of the geological setting can be seen in figure 3.2. The stratigraphy of the geology is shown in figure 3.3.

The sedimentary rocks of the Roan Group are subdivided into four groups, from bottom to top known as the Musonoï (*R-1*), Mines (*R-2*), Fungurume (*R-3*) and Mwashya (*R-4*) subgroups (Cailteux and De Putter, 2019). The Musonoï (before 2016 known as the R.A.T.) is located within the megabreccia of Kolwezi. They consist of pinkish to reddish or purple-grey hematite-rich fine-grained clastic deposits, mostly found together with dolomite, Mg-chlorite and quartz. The succession contains mostly silty to sandy bands at the bottom; in the upper part more dolomite and chloride cements can be found.

The Mines subgroup host the majority of the Cu-Co stratiform deposits in the KCB. It is mostly a carbonate succession that has been deposited in shallow-water and lagoonal environments (Cailteux, 1994). The subgroup contains, from bottom to top, the Kamoto, Dolomitic Shales and Kambove formations with an average thickness of 20 to 25 metres. The primary mineralisation is located at different stratigraphic positions, and consists of stratiform Cu-Co ores, mainly carrollite ($Cu(Co,Ni)_2S_4$), chalcopyrite ($CuFeS_2$), bornite (Cu_5FeS_4) and chalcocite (Cu_2S) (Dewaele et al., 2006).

The Fungurume Subgroup (formerly known as Dipeta) is characterised by frequent shearing, tectonic discontinuities and possible duplication of the sequences (Cailteux, 1994). Sediments in the Fungurume Subgroup show an alternating shaly greenish siltstones and dolomite beds that relate to the former Dipeta Formation. Within the dolomite beds laminar dolomites can be observed, which also contain some Cu mineralisation.

The Mwashya Subgroup is a carbonate formation which is characterised by massive interlayered talc-bearing dolomites, where sometimes oolitic beds and evaporite-type collapse breccias are observed (Cailteux and De Putter, 2019). Two later formations indicate a sea level lowering and a contraction of the basin related to climatic changes due to the onset of a major glacial period (Cailteux et al., 2005).

It needs to be mentioned that an alternative hypothesis has been proposed which suggests that the megabrecccias represent coarse clastic sedimentary deposits supplied by north advancing nappes into the foreland basin, which was for the first time introduced by Wendorff (2000). This indicates that that the origin of the regional geological settings is not widely spread, and more theories have been proposed to support this view. An overview of the current, revised and former lithostratigraphic units can be found in Appendix A.

3.1.2. Local geology

The Mutanda deposit lies within a small thrust slice bounded sliver of the Roan Group, which is located close to Kolwezi. The main Cu-Co deposits are located in the Mines Subgroup (*R-2*). Within these lithographic units, the ore bodies extend for hundreds of metres to several kilometres along strikes, which are often interrupted by faults. There is a lateral variation of the sulphides within the mineralised layers which grade from copper-rich into copper-poor zones.

However, the Mutanda deposit lies within stratigraphic units including the Fungurume (*R-3*) and Mwashya (*R-4*) of the Roan Group and lower parts of the Nguba Group (Ng 1.1 and Ng 1.3). The abundance of outcrops is generally poor, because it is underlain by clastic sediments of the lower Nguba Group. On top of that, the majority of the deposit is covered under red soil (terre rouge) and laterite (Wimberley et al., 2011).

The Fungurume (R-3) group consist mostly of argillite, which is highly weathered and where many of the exposures are massive and red to purple. In some places it has a brecciated appearance, which are probably not tectonic and may be due to the presence of expanding clay's (Herman and Beverley, 2016). This is the most common lithology present in the Mutanda project. The second most common lithology is a banded rock, which is possibly intruded with tuff, where it is highly weathered. It has the appearance of a fine-grained pyroclastic, but there is no volcanic rock in the R-3. Most typically for the R-3 is the weathering at greater depths that the other units.

The Fungurume (R-3) is in contact with the lower Nguba groups and the Mwashya (R-4), where the contacts are typically a breccia which has been infiltrated and cemented by silica and iron and magnesium oxides. Where they are in contact, the breccias locally contain heterogenite (Wimberley et al., 2011). The Lower Mwashya (R-4) is also highly weathered and contains copper and cobalt oxide mineralisation. Furthermore, the R-4 presents a very different aspect and largely consists of recrystallised dolomite with veins of chalcocite and carrollite and (more rarely) bornite. Above this dolomite is a black shale layer which locally is highly mineralised. Above the R-4 is a chaotic breccia which is interpreted to be a collapsed remnant of an original evaporite removed by hydrothermal fluids (Wimberley et al., 2011).

The Grand Conglomérat is a greenish diamictite. The unit is restricted to the Central, Southern and West Zones in the northern part of the Katanga super group . It forms the footwall to the R-4 mineralisation in the western part of the Central Zones but terminates against a fault in the east. At the location where the Grand Conglomérat is in conact with the R-4, it is mainly mineralised, and near the surface veins of malachite can be observed. However little cobalt is found. An overview of the project geology can be found in figure 3.4.

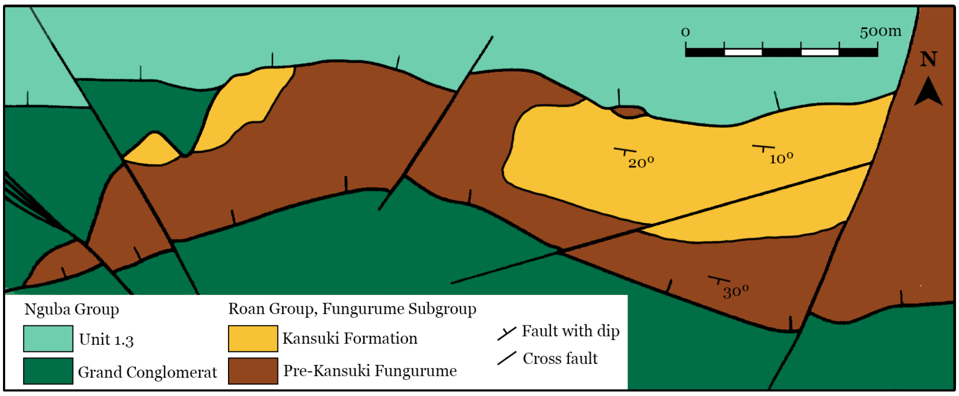

Figure 3.4: Schematic overview of the geology of the Mutanda operation (Modified from: Dehaine et al., 2017)

3.1.3. Mineralisation

The Mutanda Deposit consists out of different mineralisation facies, separated into oxide, transitional and sulphide zones. The majority of the mineralisation in the Central and Northwestern zones is oxidised, although portions still contain sulphides (Herman and Beverley, 2016). Similarly, much of the upper part of the Eastern Zone is oxidised, with sulphides appearing at large depths (Wimberley et al., 2011).

The main copper oxide minerals in the Mutanda Deposit are malachite and pseudomalachite, occurring with heterogenite as the main Cobalt mineral. The gangue material is mostly quartz and chlorite, with some contamination of illite and minor amounts of talc (Santoro et al., 2019). The minerals in which copper is present are malachite and the pseudomalachite, both having a slightly greenish colour. Generally, both the Cu-rich and Co-rich samples can be classified as an oxide-type ore, with minor secondary sulphides.

The main sulphide minerals in the Deposit are chalcocite and bornite with minor traces of chalcopyrite. The presence of pyrite is not found and the only other sulphide mineral found is carrollite. The copper sulphides tend to disseminate along bedding planes in the dolomitic argillites and in the more coarse dolomite (Wimberley et al., 2011). A less common style of sulphide occurrence is in coarse quartz breccias where there are clasts of very coarse chalcopyrite associated with coarser quartz fragments.

The average cobalt content for the Mutanda mining operation is ± 1%, and the copper content is around 3% (Santoro et al., 2019). The residues of all samples show a low value for copper. The iron content is ± 2.6% and the amount of manganese is also very low, around 0.1%. An overview can be seen in table 3.1.

Table 3.1: ICP-AES results for Co, Cu, Fe and Mn prior and after leaching tests. The results reported are the mean of the values for each element (Santoro et al., 2019)

	Grade (%)			
	Co	Cu	Fe	Mn
Mutanda	1.38	3.74	2.59	0.12
Mutanda-residue	0.37	0.15	2.73	< 0.10

According to Santoro et al. (2019), in the Mutanda Mine both heterogenite and Co-bearing mixed phases contents are low, ± 2 wt%, where the mineral is only inter grown with iron oxides in traces. On the other side, there are high contents of Cu-bearing mixed phases and Cu-secondary minerals. The gangue phases comprises up to 81 wt% where traces of sulphides and other gangue minerals are also abundant.

3.1.4. Mineral resources and ore reserves

The resource and reserve data provided in this section are as on 31 December 2018. A distinction is made between the mineral reserves and mineral resources of the project. Summarised, the mineral reserves are the portion of mineral resources that are economically feasible to produce and sell (New Pacific Metals Corp., 2018). According to CIM (2014), the mineral resources are subdivided into three categories, in order of increasing geological confidence: inferred, indicated and measured. The mineral reserves are divided in order of increasing confidence into probable and proven mineral reserves.

Comparing the resources and reserves of 2017 and 2018, an increase can be seen in both categories. The mineral resources increased by 128 million tonnes (mt) from 2017 to 2018, which can be attributed to extra drilling exploration in the Eastern part of the project area. The ore reserve estimate increased by 6 mt from 2017 to 2018 due to the updating of the resource model and engineering changes. The Mutanda operation currently has processing options for oxide and transitional ores. However, the sulphide ore reserve has been reclassified as probable due to the current uncertain political and increased cost environment (Glencore, 2018).

Table 3.2 shows the mineral resources of the total Mutanda project, which includes both the Northern and Southern mining activities. Table 3.3 shows the mineral reserves of the Mutanda project. This includes the oxide ore, the transitional ore, the sulphide ore and the stockpiles.

Table 3.2: Mineral resources of the total Mutanda project on 31 December 2018 (Glencore, 2018)

Commodity	Measured	Indicated	Measured and Indicated	Inferred
Mt	404	263	667	119
Copper (%)	1.36	0.79	1.14	0.65
Cobalt (%)	0.47	0.25	0.38	0.15

Table 3.3: Mineral reserves of the total Mutanda project on 31 December 2018 (Glencore, 2018)

Commodity	Proved	Probable	Total
Mt	80	52	132
Copper (%)	1.69	1.79	1.73
Cobalt (%)	0.70	0.59	0.66

3.1.5. Electrowinning

Because this thesis is focused on the electrochemical behaviour of cobalt, this section will briefly summarise the current electrowinning process that is used in the DRC for the Mutanda mining operation. Currently, the electrolyte is pumped to 16 polishing cells before being pumped into 66 commercial cells, where each cell has 48 cathodes and 49 anodes, which can be seen in figures 3.5 and 3.6. In this stage, the copper will plate onto the cathodes by the process of electroplating. After electroplating, the cathodes are removed from the electrowinning cells. They are washed and stripped using a semi-automatic stripping machine. The used electrolyte is pumped back into the strip section of the solvent extraction.

In order to concentrate the cobalt mineral, two stages are used; the iron/manganese removal and the cobalt hydroxide recovery, where both iron and manganese sections are treated at elevated temperatures (Wimberley et al., 2011). First, the solution from the storage pond will be recycled to leach and the pH value will be brought to 3.5. The solution is then heated by steam to a temperature of 40 °C. Iron, manganese, some aluminium and a little copper is precipitated under these oxidising conditions, afterwhich the resulting solution is pumped to the cobalt precipitation.

For the cobalt recovery, the thickener overflow and filtrate from the iron/manganese circuit is brought in contact with magnesium oxide slurry in agitating tanks at a pH of 8.2. To increase the temperature, steam is directly inserted to heat up the solution to 50 °C. Cobalt and the remaining copper in the solution is precipitated under alkaline conditions and the slurry is thickened and filtered. The resulting cobalt hydroxide cake is dried in a belt dryer and packaged in bulk bags as the finished cobalt product (Herman and Beverley, 2016).

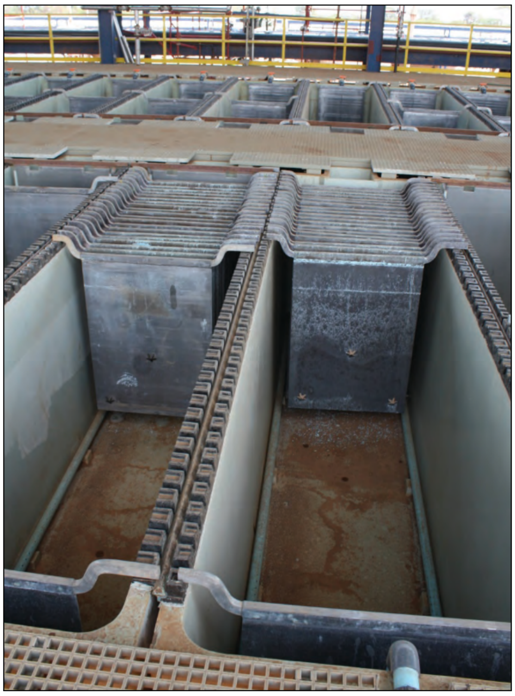

Figure 3.5: Lead anodes fitted in the electrochemical cells (Wimberley et al., 2011)

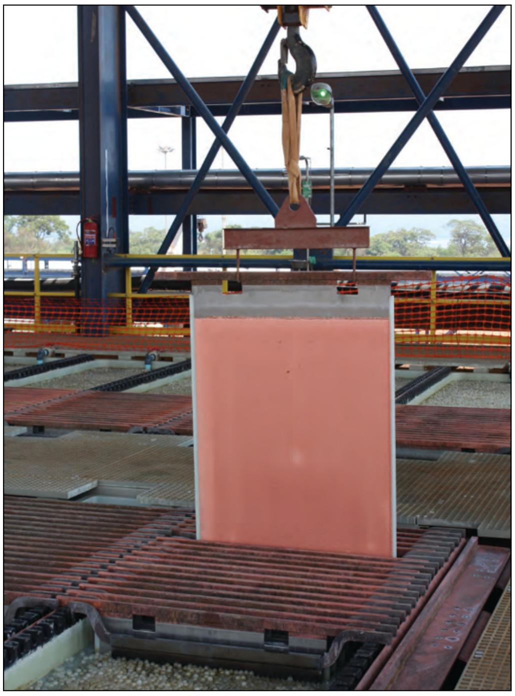

Figure 3.6: Copper cathode from the heap leach operation (Wimberley et al., 2011)

3.1.6. Future

According to Glencore (2018), the remaining mine life for the Mutanda project is estimated in excess of 15 years. However, as stated in (Glencore, 2018), the sulphide ore reserve has been reclassified as probable due to the current uncertain political and increased cost environment in the DRC. On February 8th 2019, it became clear that Glencore is cutting back on the number of expatriate workers, due to a more pessimistic view on the development of the project (Sanderson and Hume, 2019). In April 2019, another company, MMG (a Chinese state-owned company), is reviewing its own production after the DRC-government increased taxes and removed investor safeguards despite industry protests (Clowes, 2019).

In the past, extensive plans have been proposed to expand the current project with more copper and cobalt extraction by using the sulphide ores available in the deposit. However, with the increased risk of being affected by varying degrees of political and economic instability, the future of the project is unsure and by March 2019, no clear prospects for the project can be made.

In August 2019, it became clear that the project is to halt production at the end of 2019, due to a dramatic fall in prices for the cobalt element (Hune and Sanderson, 2019), caused by a surge of supply from the DRC. This downfall that the mining operation is no longer economical viable. Furthermore, Glencore is under investigation by the US Department of Justice over its business practices in the DRC, among other countries. This uncertainty results that the shares in the company have fallen a fifth, alone in this year. Since then, cobalt prices have recovered by almost 40%, but the closing of the Mutanda-project is the main reason for this recovery and it is uncertain how the prices will develop due to a fluctuation demand on, for example, car batteries.

3.2. Electrochemical processes

Electrochemistry is the branch of physical chemistry that investigates the relation between electrical and chemical effects. It is used in the process of electrowinning, which is part of extractive metallurgy and is defined as *"dealing with the extraction of metals from naturally occurring compounds and their refinement to a purity suitable for commercial use"* (Kirk–Othmer, 1978). Most of electrochemistry is focused on studying chemical changes caused by the passage of an electric current, and the creation of an electric current by chemical reactions. This can take place because electricity interacts with the evaluated matter (Fried, 1973).

3.2.1. Electrode reactions

Electrode reactions are a particular sort of chemical reactions that involve the transfer of a charge across the interface between chemical phases. This is most commonly an electron between a conducting solid (an electrode) and a solution phase (an electrolyte). An electrode is an electrical conductor that carries electric current into non-metallic solids, liquids, gases, plasma's or vacuums. The electrodes are typically good electric conductors, but it is not necessary them to be metals. An electrolyte is a substance that becomes an electrically conducting solution when dissolved in, for example, water.

The most simple type of electrode reaction involves only one electron transfer between an inert metal electrode and an ion or molecule in a solution. At the anode the electron passes from the solution phase to the electrode, and in the overall reaction the element is oxidised (equation 3.1). Reversed, at the cathode the electron passes in the opposite direction so that an element in the solution will be reduced (equation 3.2).

$$\mathrm{Co^{2+} - e^- \longrightarrow Co^{3+}} \tag{3.1}$$

$$\mathrm{Cu^{2+} + e^- \longrightarrow Cu^{+}} \tag{3.2}$$

A reaction in the electrolyte or on the electrode can be induced in an electrochemical cell, which can be described as a system containing two electrodes separated by at least one electrolyte phase. By driving the electrode to more negative potentials, the energy of the electrons will be raised. The negative potential can be increased by connecting the electrodes to, for example, a potentiostat.

Adjusting the potential, the electrolyte solution can reach a level high enough to start an electron transfer. This is when electrons travel from the electrode to the solution, which is known as a reduction current (Figure 3.7a). Vice versa, if the potential is reversed a similar phenomenon takes place, where the electrons in the electrolyte will find a more favourable energy on the surface of the electrode, and thus will transfer there. This is known as an oxidation current (Figure 3.7b).

The critical potentials at which these processes take place are known as the standard potentials, E^0, which is a characteristic value related to a particular chemical reaction. In standard conditions it is measured in volts. The more positive the potential is, the more likely it will be reduced. Table 3.4 gives some examples of the standard reduction potentials for cobalt and copper (Vanysek, 2010), measured at a temperature of 25 °C and a pressure of 1 atm.

Table 3.4: Limited overview of Co and Cu standard reduction potentials E^0 (Vanysek, 2010)

Reaction			E^0/V
$\mathrm{Co^{2+} + 2\,e^-}$	$\rightleftharpoons$	Co	−0.28
$\mathrm{Co^{3+} + 1\,e^-}$	$\rightleftharpoons$	$\mathrm{Co^{2+}}$	1.29
$\mathrm{Co(OH)_2^+ + 2\,e^-}$	$\rightleftharpoons$	$\mathrm{Co + 2\,OH^-}$	−0.73
$\mathrm{Cu^{+} + 1\,e^-}$	$\rightleftharpoons$	Cu	0.521
$\mathrm{Cu^{2+} + 1\,e^-}$	$\rightleftharpoons$	$\mathrm{Cu^{+}}$	0.153
$\mathrm{Cu^{3+} + 1\,e^-}$	$\rightleftharpoons$	$\mathrm{Cu^{2+}}$	2.40

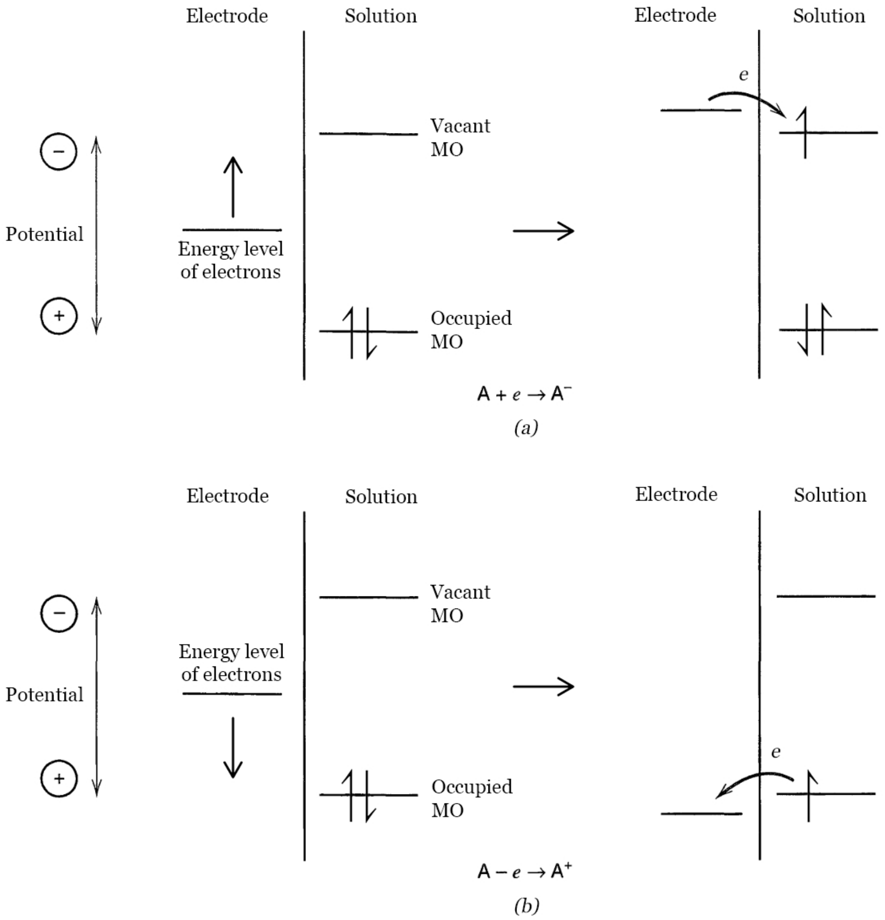
Electrode
Solution
Electrode
Solution
e
Potential
Vacant MO
Energy level of electrons
Occupied MO
A + e → A⁻
(a)
Electrode
Solution
Electrode
Solution
Potential
Vacant MO
Energy level of electrons
Occupied MO
e
A − e → A⁺
(b)

Figure 3.7: Schematic overview of (a) reduction and (b) oxidation process of a species A in solution. The molecular orbitals (MO) if species A shown are the highest occupied MO and the lowest vacant MO (Bard and Faulkner, 2001)

To start such an electron-transfer is only possible when the molecules involved in the electrode reaction are in close vicinity of the electrode. When they are close enough, a multi-step process takes place in the electron-transfer event, for example the reactions shown above. The total conversion of reactant A into product B must occur in a minimum of three steps (Pletcher, 2009):

$$A_{\text{solution}} \xrightarrow{\text{mass transport}} A_{\text{electrode}} \tag{3.3}$$

$$A_{\text{electrode}} \xrightarrow{\text{electron transport}} B_{\text{electrode}} \tag{3.4}$$

$$B_{\text{electrode}} \xrightarrow{\text{mass transport}} B_{\text{solution}} \tag{3.5}$$

The slowest of these steps is the rate delimiting factor for the rate of conversion. There are a lot of electrode reactions, varying from single electron transfer (as seen above) to multi-step processes involving several electrons and the formations of electrochemical bonds.

In general, when the potential is lowered in a particular solution the substance that is reduced first is the oxidant in the couple with the least negative E^0. As an example, using a platinum electrode in an aqueous solution containing 0.01 M each of Fe^{3+}, Cu^{2+}, and Co^{2+} in 1 M HCl, the substance that will be reduced first is Fe^{3+}, because the potential of the reaction is the most positive. Afterwards, Cu^{2+} will be reduced, and lastly Co^{2+} is reduced (Bard and Faulkner, 2001). A schematic overview is shown in figure 3.8.

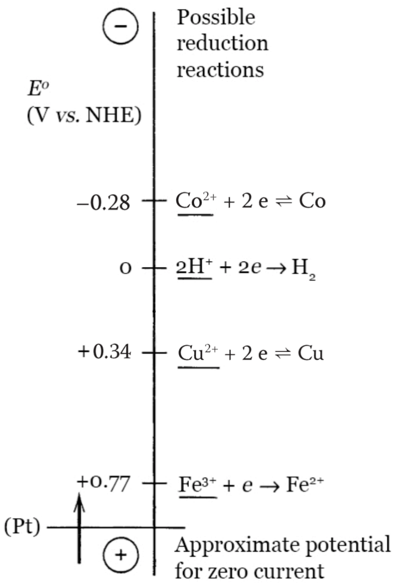
−
Possible reduction reactions
E^o (V vs. NHE)
−0.28
$Co^{2+} + 2e \rightleftharpoons Co$
0
$2H^+ + 2e \rightarrow H_2$
+0.34
$Cu^{2+} + 2e \rightleftharpoons Cu$
+0.77
$Fe^{3+} + e \rightarrow Fe^{2+}$
(Pt)
+
Approximate potential for zero current

Figure 3.8: Potentials for possible reductions of Fe^{3+}, Cu^{2+}, and Co^{2+} at a platinum electrode (Modified from Bard and Faulkner, 2001)

The overall electrode reaction, $O + ne^- \rightleftharpoons R$, is comprised out of multiple steps. Only near the electrode, electrochemical processes can occur (Figure 3.9). The phenomena involved in the electrode reaction are governed by the rates of the processes known as (Bard and Faulkner, 2001):

1. Mass transfer (e.g., of O from the bulk solution to the electrode surface).
2. Electron transfer at the electrode surface
3. Chemical reactions preceding or following the electron transfer.
4. Other surface reactions, such as adsorption, desorption, or crystallisation (electrodeposition).

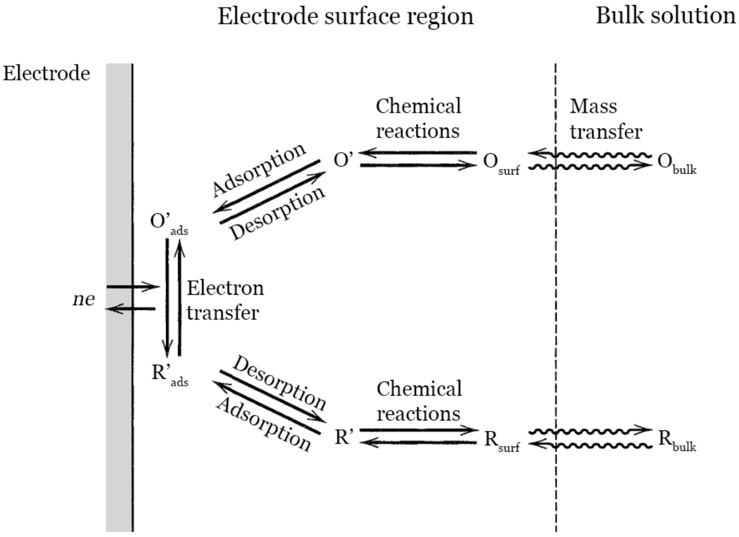
Electrode surface region
Bulk solution
Electrode
Chemical reactions
Mass transfer
Adsorption
Desorption
O'
O_{surf}
O_{bulk}
O'_{ads}
ne
Electron transfer
R'_{ads}
Desorption
Adsorption
Chemical reactions
R'
R_{surf}
R_{bulk}

Figure 3.9: Pathway of a general electrode reaction (Bard and Faulkner, 2001)

3.2.2. Phase formation and growth

In an electrochemical cell, a thin layer of electrodeposited material is formed on the electrode due to the reduction of particulate elements in the solution. Reactions that lead to the formation of a new solid phase on the electrode surface are relatively common, and examples include (Pletcher, 2009):

1. cathodic deposition of metals, *e.g.* Cu, Ni, Co
2. anodic deposition of conducting oxides, *e.g.* PbO_2
3. anodic formation of metals salts, *e.g.* AgCl, $HgSO_4$
4. anodic formation of passivating oxides, *e.g.* TiO_2, Al_2O_3
5. deposition of insulating organic films by electropolymerization or electropainting

The electrochemical potential of the cell has a significant influence on the electrochemical response and the growth and phase formation on the electrode. Also, the deposited material can be of influence on the response of the cell. For example, the formation of an insulating film will, in general, lead to a very low current density and those processes are usually very irreversible (Pletcher, 2009). A more interesting phase formation process can be illustrated by the direct reduction and deposition of a metal onto an electrode. For this research it is interesting to look at the deposition of cobalt from a sodium sulfate (Na_2SO_4) solution, as has been demonstrated by (Matsushima et al., 2006) to result in the following equation:

$$Co^{2+}(aq) + 2\,e^{-} \longrightarrow Co(s) \tag{3.6}$$

Here, the cobalt in solution is reduced to solid cobalt which can be labelled as the direct deposition of cobalt. In others words this is called nucleation, which is the formation of stable centres. In thermodynamics, nucleation is the development of a new phase in a different phase. This happens when a nucleus of atoms or molecules form a new phase and then remain stable. In the electrodeposition of a metal, the nuclei consist of the metal atoms and when the centres are small the ratio of surface area to volume tends to lead to their redissolution (Bockris et al., 1998). To establish the nuclei being large enough to be stable, an overpotential is needed which will drive the electron transfer reaction. In short the (continuous) nucleation involves several distinct stages (Pletcher, 2009), which are illustrated in figure 3.10:

a. nucleation of the new phase
b. growth of the individual metal centres
c. overlap of the growing centres, leading to a complete layer
d. thickening of the complete layer

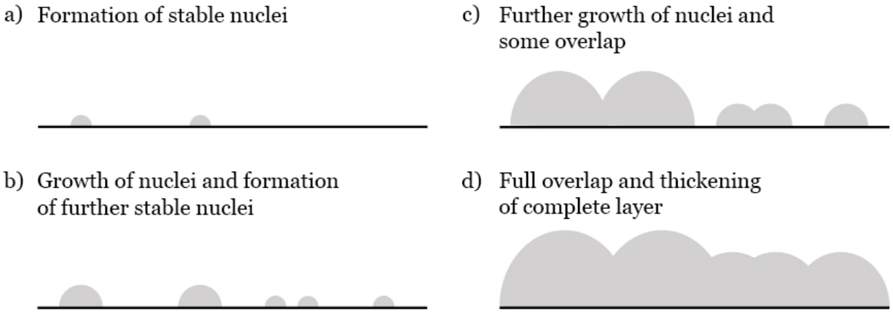
a) Formation of stable nuclei
c) Further growth of nuclei and some overlap
b) Growth of nuclei and formation of further stable nuclei
d) Full overlap and thickening of complete layer

Figure 3.10: Electrodeposition of a metal layer by a mechanism involving progressive nucleation and growth as hemispherical centres (Modified from Pletcher, 2009)

In general, there are two limiting cases of the kinetics of nucleation: *(a)* instantaneous nucleation, in which nucleation occurs at all available sites, and *(b)* progressive nucleation, where the number of centres increases with time, following first order kinetics (Pletcher, 2009). Furthermore, nucleation varies with the used material of the electrode, the used electrolyte, as well as the metal that is deposited. Once the nuclei are created, the individual nuclei will grow with a characteristic shape. In the end, a complete deposition layer will be formed, which eventually will thicken.

3.2.3. Cobalt deposition

For the electrowinning of cobalt, the reaction parameters above give an impression of the number of variables that are (in)directly linked to the electrochemical behaviour of the solution. Within the electrolyte solution, when the potential is changed over time, different reactions will occur. These reactions will either be a reduction or an oxidation, depending on if the potential is moving in the positive or negative direction, and on the standard potential of the substances in the electrolyte. In this section, the electrochemical behaviour of cobalt will be evaluated based on previous research carried out over the past years.

Due to the standard potential being highly negative for cobalt, electrodeposition is almost always accompanied by the discharge of hydrogen ions. This lowers the current efficiency and can be responsible for an increase in the pH-value which will induce the formation of hydroxide. Therefore, overall it is assumed that the formation of two types of solid cobalt product does occur. The reaction follows the steps of direct cobalt reduction and hydrogen evolution, also proposed by Kongstein et al. (1982), Bertazzoli (1997) and Flis-Kabulska (2006). They occur as the following reactions:

$$Co^{2+} + 2\,e \rightleftharpoons Co_{met} \tag{3.7}$$

$$2\,H_2O + Co^{2+} + 2\,e \rightleftharpoons H_2 + Co(OH)_2 \tag{3.8}$$

A secondary process in the electrodeposition of cobalt is the parallel hydrogen evolution reaction (HER), which is likely to cause changes in the structural and morphological properties, and will lower the overall efficiency of the process (Gabe, 1997). The pH could increase due to the electrolysis of water, which causes the formation of hydroxide ions that induce the HER, which is known in general as:

$$H_2O + M{-}H + e^- \longrightarrow M + H_2(ads) + OH^- \tag{3.9}$$

Cui et al. (2006) investigated the electrodeposition of cobalt from aqueous chloride solutions. The research came to the same conclusion as Jeffrey et al. (2000), namely that the deposition of cobalt occurs through direct cobalt reduction (reaction 3.7) and hydrogen evolution (reactions 3.8 and 3.9). Both Pradhan et al. (1997) and Nusheh and Yoozbashizadeh (2010) evaluated both reactions for the electrocrystallisation of cobalt, where is explained that the mechanism of hydrogen evolution is proposed as the cause for a changing pH on the cathode. Both papers assume that at a more acidic pH, the surface is covered by hydrogen that is formed by the HER. This reaction proceeds as follows:

$$Co^{2+} + OH^- \longrightarrow CoOH^+ \tag{3.10}$$

$$H^+ + e^- \longrightarrow H_{ads} \tag{3.11}$$

$$CoOH^+ + H_{ads} + 2\,e^- \longrightarrow Co + OH^- + H_{ads} \tag{3.12}$$

It is suggested that Co^{2+} ions are hydrolysed as shown in reaction 3.10. However, Cui et al. (2006) and Jeffrey et al. (2000) propose that if the pH is increased to 4.0 and 4.5, the reaction mechanism is different compared to reactions 3.10, 3.11 and 3.12. When the pH is increased, OH^- is formed, which means no hydrogen evolution takes place but still the mechanism indicates a further pH rise at the cathode surface during the electrowinning of cobalt. This reaction mechanism proceeds through:

$$Co^{2+} + 2\,OH^- \longrightarrow Co(OH)_2 \tag{3.13}$$

$$Co(OH)_2 + e^- \longrightarrow Co(OH)_{ads} + OH^- \tag{3.14}$$

$$Co(OH)_{ads} + e^- \longrightarrow Co + OH^- \tag{3.15}$$

Matsushima et al. (2006) used CV and EQCM to investigate the electrochemical behaviour and mechanisms of cobalt deposition for $CoSO_4$ and Na_2SO_4 as supporting electrolyte. As seen above, Cui et al. (2006), Pradhan et al. (1997) and Jeffrey et al. (2000) cited different mechanisms for Co electrodeposition through formation of $CoOH^+$ or $CoOH^+$ and $Co(OH)_2$. However, Matsushima et al. (2006) assume that only the direct reduction of cobalt takes place together with the formation of $Co(OH)_2$, which is also shown above in reaction 3.8. A follow up on this paper (Santos et al., 2007) also concludes with a reaction mechanism of direct cobalt reduction (reaction 3.7) as well as the formation of $Co(OH)_2$ (reaction 3.13).

3.3. Cyclic voltammetry

Cyclic voltammetry (CV) is a very popular and powerful electrochemical technique. It is mostly used to investigate the reduction and oxidation processes of molecular species. CV is also popular for initial electrochemical studies of new systems and has proven to be very useful in obtaining information about fairly complicated electrode reactions (Bard and Faulkner, 2001). Each experiment only takes a couple of seconds and the data are presented in a form that allows fast, qualitative interpretation without recourse to calculations (Pletcher, 2009).

In the majority of the experiments it is desired to identify the reactions that are occurring and to begin probing the mechanism and kinetics of a reaction. Therefore, the following phenomena are wished to be monitored (Pletcher, 2009):

- the number of peaks on the forward and reverse scan,
- the shapes of the peaks,
- peak potentials,
- peak current densities,
- charges associated with peaks and charge balance between the peaks,
- differences between a first cycle, a second cycle and multiple cycles.

Here, especially the two peak potentials and two peak currents provide the basis for the diagnostics developed by Nicholson and Shain (1964), which analyses the cyclic voltammetric response. For each electrode reaction a peak will be visible in the voltammogram. In the following subsections, different phenomena and wave characteristics will be investigated which relate to the curves in a cyclic voltammogram.

CV is a reversal experiment in linear scan voltammetry, which is carried out by switching the direction of the scan at a certain time, t = λ. This time is also known as the switching potential, known as E_λ. Mathematically, the used potentials at any time are given by (Bard and Faulkner, 2001):

$$(0 < t \leq \lambda) \qquad E = E_i - vt \tag{3.16}$$

$$(t > \lambda) \qquad E = E_i - 2v\lambda - vt \tag{3.17}$$

Where E is the potential of an electrode versus a reference in V, E_i is initial potential in V and v is the linear potential scan rate in V/s. Figure 3.11a shows the potential/time waveform used for a CV experiment. This potential sweep typically results in a plot of current density (or current) vs. potential, which can be seen in figure 3.11b. To generate such a plot, the potential is swept through the expected potential range in which an electrode reaction will occur. Then, the direction of the scan will be reversed in order to determine whether the product of electron transfer is stable and/or if other reactions can be distinguished.

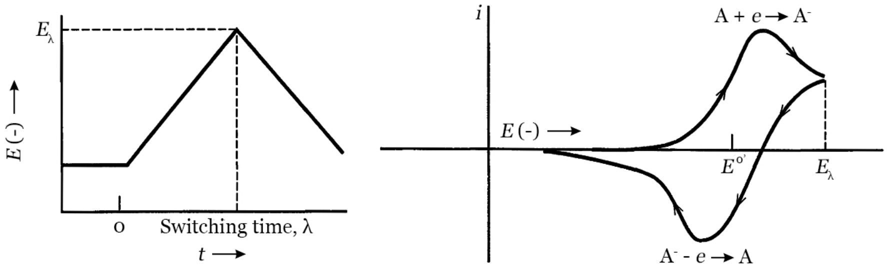

(a) (b)

Figure 3.11: (a) Cyclic potential sweep. (b) Resulting cyclic voltammogram (Bard and Faulkner, 2001)

The cyclic voltammogram is dependent on several factors, which can include the concentration of the reactant, pH, temperature and the material of the electrode. For example, the settings for the initial potential determines the initial concentration profiles for the tested products and reactants, and is chosen at a potential where the current density is equal to zero. Furthermore, the software connected to the potentiostat can regulate several parameters; the potential limits, the direction of the initial scan, the potential scan rate and whether only a first scan or multiple cycles will be recorded.

Mostly, the negative potential scan is chosen for the first half-cycle, starting from a value where it is expected that no reaction will occur. During the reversed scanning direction molecules, generated in the forward half-cycle, are reoxidised, which results in an anodic peak. The characteristic peaks are caused by the creation of a diffusion layer close to the surface of the electrode. These can be understood best by investigating the concentration-distance profiles during the potential sweep. Figure 3.12 shows four concentration gradients for the reactant (C_O) and product (C_R) at several times, which correspond to (Wang, 2006):

a. the initial potential value,

b. the formal potential of the couple during the forward scan,

c. the achievement of a zero-reactant surface concentration, and

d. the formal potential of the couple during the reversed scan.

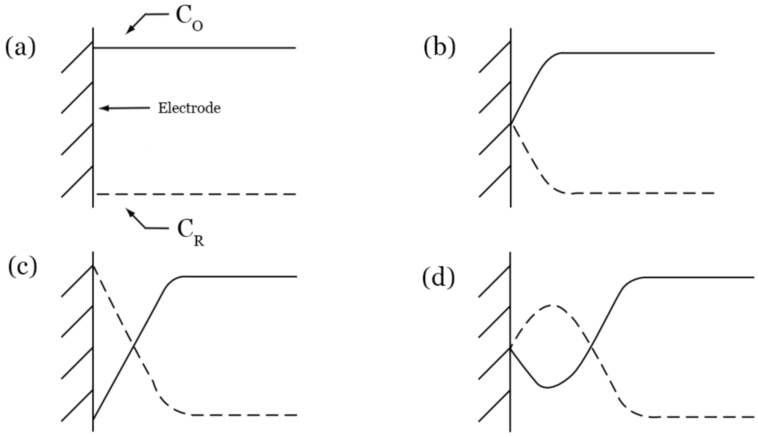

Figure 3.12: Concentration distribution of the oxidised and reduced forms of the redox couple (Wang, 2006)

When electron transfers are compared to chemical reactions, CV can be relevant to provide kinetic characteristics. In a lot of cases, these coupled reactions can be linked to a specific type of mechanism that has been evaluated and described in earlier research. This means that a careful examination of a CV test/experiment can help in evaluating what reaction mechanism is occurring as well as the kinetics of these reactions (Rountree et al., 2018).

3.3.1. Wave characteristics

As can be seen in figure 3.11b, each wave has a distinctive shape that characterises the wave itself. Most important are the peak potential (E_p), half-wave potential ($E_{1/2}$), peak current (I_p) and half-peak potential ($I_{p/2}$), which can be seen in figure 3.13.

The *peak potential* is where the current reaches a maximum or minimum during the experiment. From the peak potential, one can obtain information about, for example, the rate of electron transfer, binding constants or the rate determining step of a multi-step transformation by measuring how the peak potential changes under different circumstances (Graham, 2018). The peak potentials of a reversible wave do not change when different scan rates are used.

The *half-wave potential* is the potential exactly in between the two peak potentials in the cathodic and anodic direction. According to Graham (2018), for a reversible, one electron wave in a cyclic voltammogram measured under standard conditions, the two values of E_p should be ±60 mV apart. The standard potential (E_0) of an analyte is equal to $E_{1/2}$ under standard conditions with a 1 M.

The *peak current* is the maximum current of one wave within a cyclic voltammogram, which is corrected for the baseline of the cyclic voltammogram. For example, if the baseline current before the wave is 3 μA, this must be subtracted from the peak current of the corresponding wave.

The *half peak potential* is the potential at which the current is half of the value of the peak current, also applying a baseline correction. For example, if a wave has a peak current of 4 µA, the $E_{p/2}$ of the wave is the potential at which the current is 2 µA.

In figure 3.13, characteristic points of a cyclic voltammogram can be seen, such as the peak (E_p^a, E_p^c) and the half-peak potentials ($E^a_{p/2}$, $E^c_{p/2}$). These points give a static representation of the voltammogram, therefore it is better to interpret the shape of the whole voltammogram, to get a more extensive view of the electrochemical behaviour (Pletcher, 2009). In red, the direction of the scan is visible. The scan towards a more negative potential is the cathodic scan. The scan in the direction of a positive potential is the anodic scan.

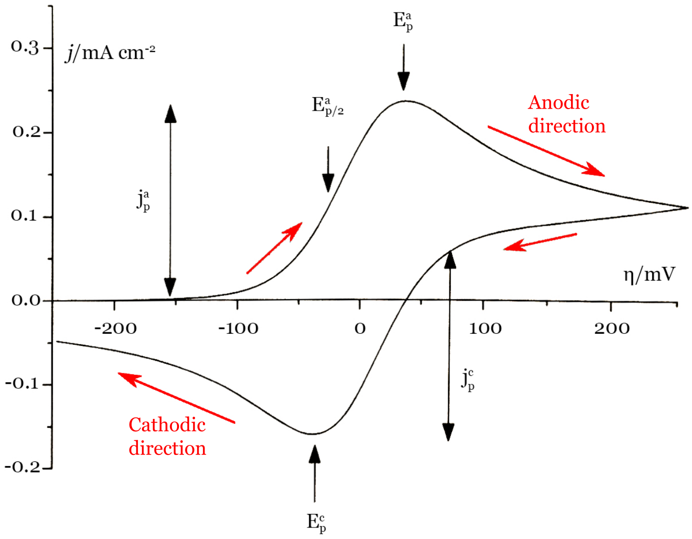

Figure 3.13: Voltammogram to define the symbols used in table 3.5 (Pletcher, 2009)

3.3.2. Electrochemical reversibility

The most common way to characterise features in cyclic voltammogram is by investigating the electrochemical reversibility. Reversibility does not mean what people will often think first; qualifying something as reversible might suggest that an electron can be added to and removed from a redox active molecule. It does not, however, mean this. Electrochemical reversibility describes the rate of electron transfer (Graham, 2018). Different forms exist, which are reversible electron transfer, an irreversible electron transfer, chemical transformations of electron transfer products and quasi-reversible electron transfers.

For a reversible electron transfer, it is assumed that both the reduced and oxidised forms of the solution are stable in the electrolyte and the electron transfer is rapid. This means that the electron transfer is easy and occurs frequently whenever an analyte molecule approaches the electrode. The exact form of the voltammogram is dependent on a variety of parameters, however, during a cycle, for a reversible couple the formal potential is found from equation 3.20. With a trained eye, the shape of a voltammogram for a reversible couple can be examined. More theoretically, it can also be determined with some well known test, which can be found in table 3.5. The clarification of the parameters used in table 3.5 can be found in figure 3.13.

For an irreversible process, the individual peaks are reduced in size and can be widely separated. According to Pletcher (2009), the peak for an oxidation will shift to more positive values and become more drawn out along the potential axis compared to the reversible variant. On the other hand, a peak for the reduction curve will shift towards the negative and will also become more drawn out. In the end, this results in a movement of the oxidation and reduction peaks further out from each other and they become less steep as well.

Overall, peaks for an irreversible reaction are a little less high than the ones for reversible processes, and according to Pletcher (2009), they are less steep and it takes a longer time for the surface concentration of the reactant to be driven down to zero. Irreversible systems can be characterised by a shift of the peak potential which can be quantified by equation 3.22. Figure 3.14 shows two different characteristic curves for a reversible and irreversible redox process.

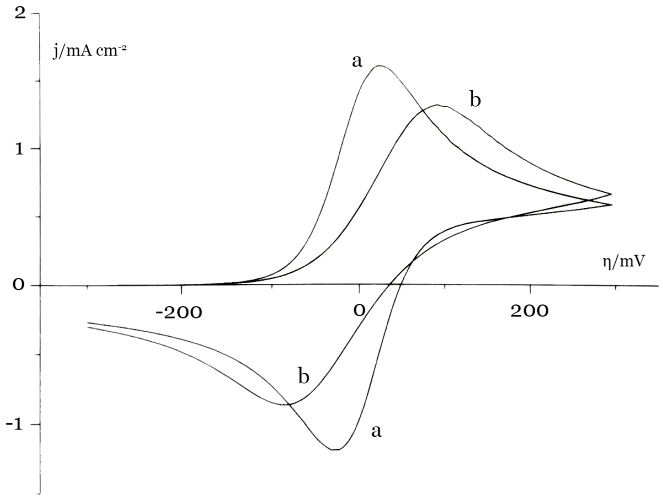

Figure 3.14: Voltammograms for reversible *(curve a)* and irreversible *(curve b)* redox processes (Wang, 2006)

Table 3.5: Tests for the the form of cyclic voltammetric responses for a reversible and irreversible couple at 298 K (Pletcher, 2009)

Experimental measurable	Reversible couple	Irreversible couple
$\Delta E_p = E_p^a - E_p^c$	$\frac{59}{n} mV$	$> \frac{59}{n} mV$ and $f(k_s, v)$
$E_p - E_{p/2}$	$\frac{59}{n} mV$	$\frac{48}{\alpha n} mV$
E_p	Independent of v	Dependent on v
j_p	Proportional of $v^{1/2}$	$v^{1/2}$

A term that is often given to electron transfers that are in between irreversible and reversible systems, is a quasi–reversible system. There is no total agreement on what quantifies quasi-reversible systems from irreversible. However, it must be taken into account that a measured quasi-reversible wave can be reversible, and what looks like a quasi-reversible wave could be a reversible wave measured with an electrode that was polished wrongly.

After applying the tests given in table 3.5, it cannot be said for sure if a process is irreversible, quasi-reversible or reversible. As extra validation to quantify this, when the difference between the cathodic and anodic peak potentials increases with the scan rate, and the average peak potentials ($\left(E_p^c - E_p^a\right)/2$) are constant for different scan rates, the process could be quasi-reversible (Mishra et al., 2015). To validate this, the heterogeneous electron transfer rate constant k_s can be used, proposed by Klingler and Kochi (1981), which makes use of the separation of the cathodic and anodic peaks and is shown as equation 3.18. First, the D_O, α and n can be obtained from the Randles-Sevcik equations where the system can be categorised preliminary.

$$k_s = 2.18\left[D_0\left(\alpha n_\alpha\right)\frac{vF}{RT}\right]^{1/2}\exp\left[\frac{\alpha^2 n_\alpha F}{RT}\left(E_p^c - E_p^a\right)\right] \tag{3.18}$$

Where αn_α is obtained using equation 3.19:

$$\left|E_p^c - E_{p/2}^c\right| = \frac{1.857RT}{\alpha n_\alpha F} \tag{3.19}$$

Using equation 3.18, if $\left[k_s/(v)^{1/2}\right] > 0.11$, the process is reversible. If $0.11 > \left[k_s/(v)^{1/2}\right] > 3.7 \times 10^{-6}$, the process is quasi-reversible and if $3.7 \times 10^{-6} > \left[k_s/(v)^{1/2}\right]$, the process is irreversible.

To summarise, according to García-Miranda Ferrari et al. (2018), the Randles–Ševcik equation (at non standard conditions) for reversible, quasi-reversible and irreversible electrochemical processes are

$$i_p^{rev} = 0.446nFAC^O\left(\frac{nvFD_0}{RT}\right)^{1/2} \tag{3.20}$$

$$i_p^{quasi} = 0.436nFAC^O\left(\frac{nvFD_0}{RT}\right)^{1/2} \tag{3.21}$$

$$i_p^{irrev} = 0.496nFAC^O\left(\frac{(\alpha n_\alpha)\,vFD_0}{RT}\right)^{1/2} \tag{3.22}$$

where for all equations, n is the number of electrons in the electrochemical reaction, i_p is the voltammetric current using the peak in the voltammogram, F is the Faraday constant (C mol^{-1}), v is the scan rate (V s^{-1}), R is the gas constant, T is the temperature in K, A is the area of the electrode (cm^2) and D is the diffusion coefficient (cm^2 s^{-1}), α is the transfer coefficient, and n_α is the number of electrons transferred before the rate determining step.

The diffusion coefficient (D) is generally known for a given pair of species and pairwise for a multi-species system. The higher the value of the diffusion coefficient (of one substance with respect to another), the faster the species will diffuse into each other. α gives an indication of how reactant-like or product-like the state is in terms of the electrical behaviour. The value of α lies between zero and one. If it is close to either of the two extremes (0 or 1), it can be said that the transition state is either very reactant-like or very product-like. See figure 3.15 for a graphical overview with the corresponding voltammograms.

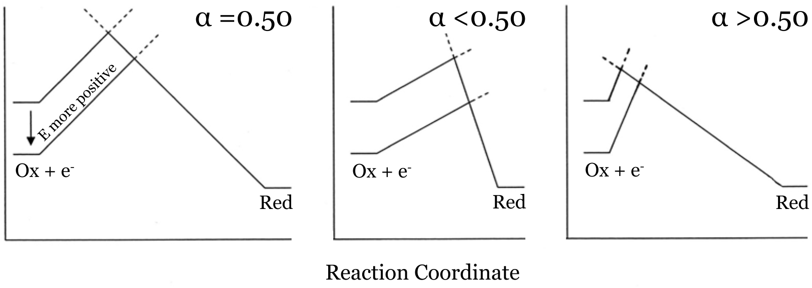

Figure 3.15: The transfer coefficient as an indicator of the symmetry of the voltammograms (Harvey, 1999)

3.3.3. Scan rate

One of the most important input parameters of cyclic voltammogram is the scan rate, which controls how fast the applied potential is scanned. In general, an increasing scan rate leads to a decrease in the size of the diffusion layer. This results in higher currents being observed, which can be seen in figure 3.16. Using the measurements of multiple scan rates of/on/for the some solution, several interesting parameters can be obtained. For electrochemically reversible electron transfer processes, the Randles-Sevcik equation (eq 3.20) is used to describe how the peak current i_p (A) will increase linearly with the square root of the scan rate v (V s^{-1}). The equation can indicate if an analyte is freely diffusing in the solution, which will be explained later on. Furthermore, equation 3.20 can be used to calculate the diffusion coefficient of the evaluated solution.

For this thesis, for almost all tested solutions the value for α, D and k_s are calculated by plotting the square root of the scan rate ($v^{1/2}$) against the peak current of the corresponding voltammogram. The linear dependence of the peak current with the square root of the scan rate is measured with electrochemical probes that are dependent on D. For molecules that adsorb on the electrode the value for alpha will be dependent on the scan rate instead of the square root.

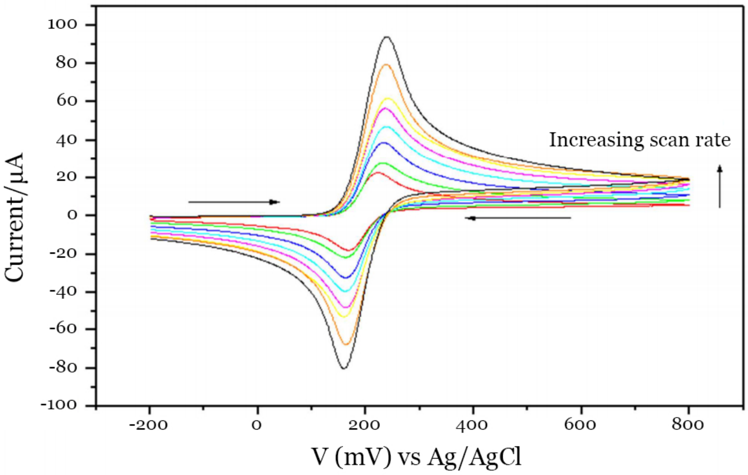

Figure 3.16: Example of voltammograms at different scan rates of 30, 50, 100, 150, 200, 250, 300 and 400 mV/s (Kasa and Solomon, 1964)

3.4. Electrochemical quartz crystal microbalance

The electrochemical quartz crystal microbalance (EQCM) is a measurement tool for quantifying electrodeposition, especially electrochemical parameters and mass changes at the surface of the electrode. The working principle of the EQCM is based on a quartz crystal wafer, which is sandwiched between two electrodes. These are used to induce an electric field in the electrolyte. In this research, the electrodes are made out of platinum, but they are available in a variety of other metals. A schematic overview can be seen in figure 3.17.

The EQCM uses the basic principles of the piezoelectric effect, which was discovered 1880. It was discovered that a mechanical stress applied to the surfaces of multiple crystals, which also included quartz, afforded a corresponding electrical potential across the crystal whose magnitude was proportional to the applied stress (Buttry and Ward, 1992). Afterwards, the piezoelectric effect was verified by application of a voltage across these crystals which resulted in a corresponding mechanical strain. This effect is the basis of the EQCM.

The electric field that is created produces a mechanical oscillation in the bulk of the wafer inside the EQCM. When surface reactions occur, a small mass change is involved, which in this case can cause perturbation of the resonant frequency of the crystal oscillator. Due to electrodeposition, a frequency change (Δf) is observed which relates to a positive mass change (Δm), which can be used in the *Sauerbrey equation*, established in 1959 (Sauerbrey, 1959).

$$\Delta f = -\frac{2\Delta m n f_0^2}{A\sqrt{\mu\rho}} \tag{3.23}$$

For this equation, n is the overtone number, f_0 is the base resonant frequency of the crystal (each EQCM has its own characteristic resonant frequency), A is the area (cm^2), and μ is the shear modulus of quartz (equal to 2.95×10^{11} gcm^{-1}s^{-1}). With the help of this formula, frequency changes can be converted to mass changes on the electrode surface. As can be seen in equation 3.23, the negative sign indicates a decrease in mass corresponding to an increasing in the frequency, and the other way around.

The EQCM is a very sensitive and accurate measuring tool that can detect mass changes as small as 1 ng/cm^2. This can be used for investigation of the deposition or dissolution of surface layers and other chemical phenomena. In this research EQCM resonator will be used as one of the electrodes that is in contact with the electrolyte solution in the electrochemical cell. This allows to measure the potential and the frequency changes simultaneously.

When the thickness of a deposited layer is minimal compared with the thickness of the microbalance, mass changes of <0.05% of the crystal mass commonly can be achieved (Wang, 2006). It has already been proved that using the combination between the EQCM with a scanning electrochemical microscopy can be used for studying the dissolution of various thin films (Cliffel and Bard, 1998), which also will be done in this thesis.

An example of the output of an EQCM measurement can be seen in figure 3.18, which is also known as a gravimetric curve of the electrodeposited material measured in the -1100 until -700 mV potential range. As can be seen, the potential is varying back and forth to increase the deposited material on the electrode. This can be concluded, since a frequency decrease can be observed from ±1600 Hz to almost zero. As stated before, a frequency decrease is equal to an increase of mass on the quartz crystal.

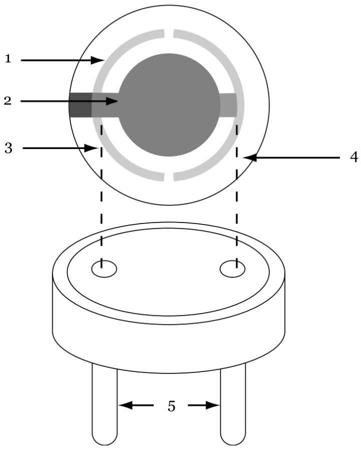

Figure 3.17: Quartz crystal microbalance: (1) the quartz crystal; (2) the (platinum) electrode; (3,4) connecting metal wires; (5) the base. (Wang, 2006)

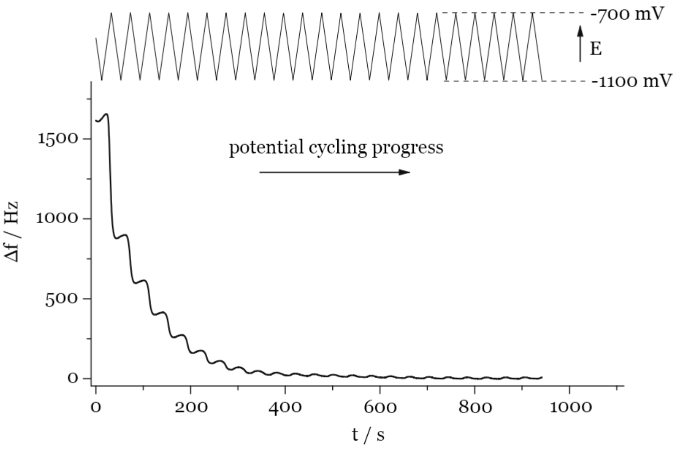

Figure 3.18: Example of an EQCM output presenting a frequency change as a function of time of potential cycling. The applied potential changes are depicted at the top of the figure. The used solution is a 1 M KOH_{aq} solution measured at a scan rate of 20 mV s^{-1} (Grdeń et al., 2009)

For this thesis, besides the mass increase another valuable parameter can be obtained using the EQCM-technique. When the Sauerbrey equation is combined with Faraday's law, the number of electrons involved in the reaction can be calculated, which can be seen in equation 3.24. Using this formula, the species involved in the electrochemical reactions can be evaluated by plotting the frequency variations (Δf) as a function of the charge consumed during the reaction (Q) within the electrolyte.

$$\Delta f = -\left(\frac{KM}{Fz}\right)Q \;\rightarrow\; \frac{M}{z} = \left|\frac{d\Delta f}{dQ}\right|\left(\frac{F}{K}\right) \tag{3.24}$$

Where K is the experimental mass coefficient, in this research equal to 9.335×10^8, F is the Faraday constant, M is the molar mass of the deposit, z is the number of electrons involved and $|d\Delta f/dQ|$ is equal to the slope of the frequency versus charge curve obtained by the EQCM-technique. With the help of the graph, the electrochemical behaviour and reactions of the electrolyte can be evaluated.

The characteristic M/z values for reaction can be calculated by dividing the molar mass of the created substances (right of the arrow in a chemical reaction), by the number of electrons involved in the reaction. According to Matsushima et al. (2006), OH^- does not participate in the molar mass of the solution. Table 3.6 gives an overview of the expected reactions that will occur during the experiments in this thesis. Using the characteristic M/z values can give a good insight in the electrochemical activity of the solutions. For copper, the M/z values can increase up to 140, then slowly decrease to 120 and finally decrease to circa 80 indicating that Cu reduction does not occur from the free ion, but instead via the adsorption of another compound (Zhao et al., 2017).

Table 3.6: Characteristic M/z values for reactions used for this thesis

Reaction equation	Electrons involved (z)	Molar mass (M)	M/z
$Co^{2+}_{(aq)} + 2\,e^- \longrightarrow Co(s)$	2	58.93	29.50
$Co^{2+}_{(aq)} + 2\,H^+ + 4\,e^- \longrightarrow Co(s) + H_2(ads)$	4	60.95	15.24
$Co^{2+}_{(aq)} + 2\,H_2O + 4\,e^- \longrightarrow Co(s) + 2\,OH^- + H_2(g)$	4	59.20	14.80
$Cu^{2+}_{(aq)} + 2\,e^- \longrightarrow Cu(s)$	2	63.50	31.75
$Fe^{3+}_{(aq)} + 1\,e^- \longrightarrow Fe^{2+}_{(aq)}$	1	55.84	55.84

3.5. Effects on the electrochemical behaviour of cobalt

Cobalt is one of the world's most valuable elements, and despite the fact that most of the world's cobalt is produced by electrowinning, there is very little fundamental knowledge of this process (Jeffrey et al., 2000). The aim for most of the mineral recovery of cobalt is to produce a high quality deposit through an optimised current efficiency and a minimised power consumption. However, nowadays the most popular electrowinning recovery process for cobalt uses a sulfate medium, which is not efficient (Jeffrey et al., 2000). This section will discuss several parameters that influence the electrochemical behaviour of cobalt.

3.5.1. Temperature

While investigating the electrochemical behaviour, it becomes clear that temperature can effect parameters such as the current density within the electrolyte solution. Figure 3.19 shows the effects of temperature on cobalt depositions and stripping in a solution of boric acid in demineralised water. It was also discovered by Elsherief (2003) that an increase in temperature activates the dissolution of cobalt. It can be said that the temperature has an influence on the deposition and dissolution of the cobalt reaction, where increasing the temperature appears to improve the reaction of the deposition. The downside is that more energy would be required in order to reach this temperature for the electrolyte solution. Also, it was found that the hydrogen evolution reaction occurs more readily at higher temperatures, which is not in favour of the optimal conditions for cobalt electrodeposition.

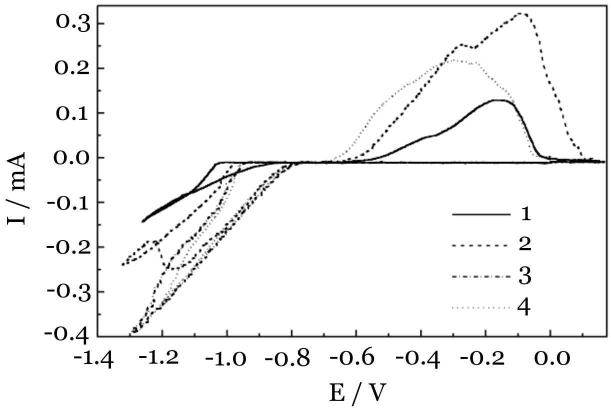

Figure 3.19: Voltammograms for cobalt deposition and stripping in 60 g l^{-1} Co + 30 g l^{-1} boric acid, 20 mV s^{-1} at various temperatures; (1) 20, (2) 40, (3) 50 and (4) 60 °C (Elsherief, 2003)

In figure 3.19, the differences in the anodic and cathodic peaks are visible. The higher the temperature, the higher the current is, where a temperature of 40 °C gives the highest peak at around 0.3 mA. In the negative direction of the current, the peaks for characterising the deposition parameters can be found. Here, clear differences can be seen for an increasing temperature. Temperatures of 20, 40, 50 and 60 °C have an increasing negative starting point of the cobalt reaction. This can be interesting to investigate for this project, but more research is needed to make sure the costs for increasing the temperature will be covered with the revenue from an increase in cobalt deposition.

Pradhan et al. (1997) says that temperature always plays an important role during the electrowinning of cobalt, because it increases the current yield and decreases the energy requirement. Das and Subbaiah (1984) suggests that the best operation conditions of an electrochemical cell is 60 °C or above. For the study performed by Pradhan et al. (1997), an increase in current efficiency with temperature for different concentrations of zinc showed linearity, where the concentration of zinc was not taken into account. Furthermore a decrease in the power consumption was observed when the temperature was increased. Lupi and Pilone (2001) suggest that a 60 °C bath temperature produces low power costs and good quality deposits of cobalt on the electrodes within a sulfate acid medium.

Further research was carried out by Santos et al. (2007) for the effects of temperature on Co electrodeposition in the presence of boric acid. The research consisted of evaluating the cyclic voltammogram in combination with the EQCM. Their research indicated that the mechanism of cobalt electrodeposition changed when the temperature was increased in a sulfate solution where boric acid was added as a buffer. They recorded that at 25 °C only direct cobalt reduction takes place, where at 48 °C, $Co(OH)_2$ could be observed. They also stated that for high temperatures the desorption mechanism is greater, which will lead to an increase of the surface area of the electrode. This makes it possible that $Co(OH)_2$ can be created.

3.5.2. pH-value

As with different temperatures, the pH-value of the electrolyte is an important parameter to influence the reaction kinetics of cobalt electrodeposition. It is clear that the calculated peak current is a function of the pH-value, where cobalt deposition occurs more readily at higher pH values (Jeffrey et al., 2000). Furthermore, it is worth noting that experiments performed in an unbuffered solution show an even more significant change in the dependence on the pH-value. At higher pH-values, hydrogen evolution starts to occur. This mechanism is shown in equation 3.25.

$$\begin{aligned} Co^{2+} + H_2O &\rightleftharpoons CoOH^+ + H^+ \\ CoOH^+ + e^- &\rightleftharpoons CoOH \\ CoOH + H^+ + e^- &\rightleftharpoons Co + H_2O \end{aligned} \tag{3.25}$$

Jeffrey et al. (2000) states that with increasing the pH, the current efficiency is increased due to both enhancement of cobalt deposition and the reduction in hydrogen evolution. The pH cannot be increased too much, because this would result in more resistance in the solution and the acidity would become to high and the electrochemical process cannot be continued properly. Zhang et al. (2002) shows that for oxidation of Mn(II) out of cobalt and nickel the reaction is strongly dependent on the pH. Below pH 3 almost no oxidation will occur and as the pH is increase, the reaction is seen to be strongest at pH 6. This gives no implication for the conditions in the research, but makes clear that pH is indeed a very important factor.

Increasing the pH too much is not favourable for the reaction, but lowering it too much is bad as well. Nemtoi et al. (2009) discovered that for the electrodeposition of Fe, Co and Ni from aqueous solutions, at strong acid pH values ($pH \leq 1$) there will be no deposition of Fe, Co or Ni in sulfate solutions because there is an intense release of hydrogen. The optimal pH range was defined to be within a pH of 3.00 to 5.50, where lower values create hydrogen release and higher values allow the creation of vast amounts of metal hydroxides, which is not favourable.

Schwarzacher et al. (2007) evaluated the influence of pH on the deposition of cobalt within a 0.02 M $CoSO_4$ + 0.1 M Na_2SO_4 electrolyte with and without the addition of boric acid, H_3BO_3. It was discovered that when using a sufficiently low pH of 3.1, the Co metal deposits on the cathode using reaction 3.26. When the pH was increased to 5.75, the deposit molar mass suggested a possible co-deposition of Co hydroxide and Co metal. When boric acid was added to the electrolyte, the formation of Co hydroxide was prevented, probably caused by the buffer solution which prevents a drastic increase in pH near the electrode, caused by the reaction shown in equation 3.27 (Schwarzacher et al., 2007).

$$Co^{2+} + 2\,e \rightleftharpoons Co_{met} \tag{3.26}$$

$$2\,H_2O + Co^{2+} + 2\,e \rightleftharpoons H_2 + Co(OH)_2 \tag{3.27}$$

To confirm the theory shown above, Matsushima et al. (2006) stated that using a pH of 3.33, an absence of cobalt hydroxide in a 0.1 M $CoSO_4 \cdot 5\,H_2O$ solution, with 1.53 M Na_2SO_4 as supporting electrolyte was used. Cobalt hydroxide was formed (equation 3.27) when the pH was increased above 4.10. This hydroxide was formed by the hydrogen evolution reaction (HER). They also concluded that the CV in combination with the EQCM is a good and useful in situ tool for investigating the effects of pH and polarisation time on the electrode surface during metal deposition.

3.5.3. Concentration

Another influence on the electrochemical behaviour of cobalt is its concentration. Different concentrations of cobalt in electrolyte solutions have been evaluated for their electrochemical behaviour. Elsherief (2003), for instance, evaluated various concentrations of 5, 20, 40 and 60 g/l in a solution of 30 g/l boric acid. The voltammograms obtained showed that increasing the concentration of cobalt causes a gradual increase in the current on the cathodic side of the diagram. He also denote that as the cobalt concentration increases, the current density changes to a more positive potential, which denotes an increase in the deposition of cobalt.

Overall, the cyclic voltammograms show that as the concentration of cobalt increases, the area covered by the anodic curve is larger. This indicates that there may be an increase in the cobalt deposition efficiency. Lupi and Pilone (2001) suggest that for nickel-cobalt electrowinning from a sulfate acid electrolyte, an increase of the cobalt concentration in solution will increase the current efficiency, with a maximum energy consumption with 4 g/L Co.

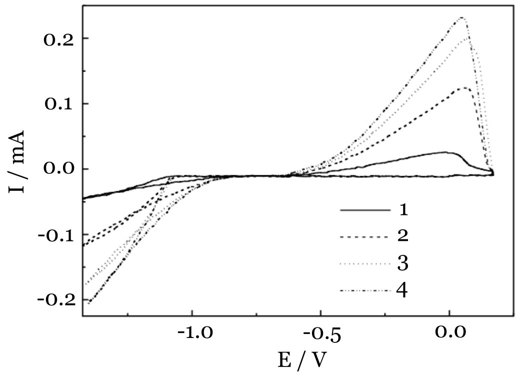

Figure 3.20: Voltammograms for cobalt deposition and stripping in various cobalt concentrations + 30 g l^{-1} boric acid, pH 4 solutions at 20 °C and 20 mV s^{-1}. Cobalt conc.: (1) 5, (2) 20, (3) 40 and (4) 60 g l^{-1} (Elsherief, 2003)

Also, more variations of additives and supporting substances are added to the solution at different concentrations. Zhang et al. (2002) investigated different concentrations of manganese added to the electrolyte, Cao et al. (2019) looks at different levels of chloride concentrations and Nemtoi et al. (2009) investigated several concentrations of $CoSO_4$, $NiSO_4$ and $FeSo_4$. In all of these studies it was found that changing the concentration of the cobalt or other additions will influence the electrochemical behaviour of cobalt. Therefore, for all different variations of electrolytes research is needed to select its optimal environment for electrodeposition.

3.5.4. Magnetic fields

The formation of layers due to electrodeposition can be influenced by the magnetic fields (B), which can influence the structure and morphology. This process can then change the properties of the electrodeposited layers in multiple ways. Krause et al. (2004) investigated the effect of magnetic fields on the electrodeposition of cobalt, in which the main objective was to explore which effects are generated by a homogeneous B-fields of different strength and orientation during the electrodeposition of cobalt. To do this, a combination of CV and EQCM was used.

The used electrolyte was 0.01 M $CoSO_4$ with an addition of 0.1 M Na_2SO_4 as the supporting electrolyte. The measured pH value of the solution was 3. Four different orientations of the magnetic field where investigated, two parallel to the electrode surface (A and B in figure 3.21) and two perpendicular to the surface (C and D in figure 3.21).

Two different effects of a magnetic field were observed that influenced the electrodeposition of cobalt. These are the magnethohydrodynamic (MHD) effect caused by the Lorentz force, and decreasing deposition of the electrolyte, which can be attributed to the actions of the (para)magnetic force. The Lorentz forces where only measured for the perpendicular orientations to the flow of the ions inside the electrochemical cell. Here, an increase of the deposition rate was observed with an increasing strength of the magnetic field (Krause et al., 2004). A decreasing deposition rate was measured for B-fields that where parallel orientated, which means they were perpendicular to the surface of the electrode. This was also confirmed by Yu et al. (2015).

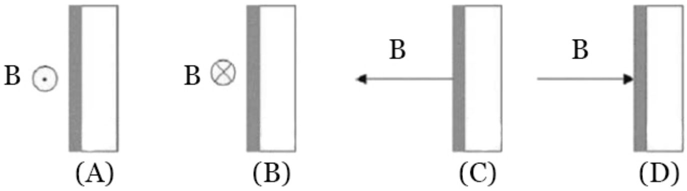

Figure 3.21: B-field relative to the electrode configurations (Krause et al., 2004)

Furthermore, Mięko≴ et al. (2018) investigated the effects of a constant magnetic field (CMF) on electrolysis for cobalt alloys. Magnetic fields were used ranging from 0 to 1.2 T, directed both perpendicular and parallel to the surface of the electrode, for which they mainly used cobalt sulfates. It was observed that electrodeposited alloys in the presence of a magnetic field were much smoother than in the absence of the field, which indicates that the electrodeposited material does not show any cracks. It was also observed that the content of the cobalt increases under CMF. The CMF had no influence on the content of ingredients in the different alloys, so no other substances are electrodeposited.

It has been shown that the chemical composition of alloys at magnetic fields of 0 T, 200 mT, 600 mT and 1200 mT were obtained, where % wt. is the weight percentage of the elements in the alloys. For example, for a Co-Mo alloy, the weight percentage of the cobalt component increased from 57.9% at 0 T, to 68.7% at 1200 mT, which is a significant increase of the yield.

Even though these studies have shown that a(n) (constant) electric field can increase the yield of cobalt electrodeposition, unfortunately this will not be tested within this thesis. A suitable setup is not available, and even then it would not be possible within the time period. However, it is interesting to continue further research on the influence of magnetic fields and investigate the potential to increase the cobalt electrodeposition using this method.

3.5.5. Additives and impurities

In electrochemical cells on an industrial scale there is a high chance impurities will occur. The probable impurities that are associated with a cobalt electrolyte are Cu^{2+}, Ni^{2+}, Fe^{2+}, Zn^{2+}, Mg^{2+}, Fe^{3+}, Al^{3+}, PO_4^{3-}, AsO_4^{3-}, etc (Pradhan et al., 1997) . Elsherief (2003) investigated the presence of common plant impurities, such as zinc, copper and iron. It is likely that these impurities will be present when using real samples from a mining site. These impurities have a negative effect on the cathode quality, the current efficiency and on the crystal structure of the electrodeposited cobalt.

First Elsherief (2003) evaluated the effects of zinc, which is shown in figure 3.22a. Here it can be seen that the anodic current peak increases up to a zinc addition of 300 ppm. If the zinc concentration is increased further, the peak current decreases. When 800 ppm of zinc is added, the current loses more then half of its original peak current compared to when no zinc was added to the solution.

This can be clarified due to the more negative potential of zinc compared with the potential of cobalt: the difference is ± 0.5 V. Therefore, it is expected that the cobalt will deposit earlier than the zinc in this solution. When an electric field is induced in the cell, zinc cations will move towards the electrode, building up near the cathode surface, making it difficult for the cobalt ion to approach the electrode (Elsherief, 2003). This reduction, however, is also observed when small amounts of zinc are present in the solution.

Furthermore, Pradhan et al. (1997) concludes that the presence of zinc in the cobalt electrolyte causes a fall in current efficiency in the temperature range of 0 to 80 °C, where the drop in current efficiency is higher when the temperature is lower. It is also discovered that the power consumption is relative low at a higher temperature than when the experiment is executed at a lower temperature. Overall, the presence of zinc causes an increase in current density which decreases the current efficiency, and an increase in power consumption.

The same applies to the addition of copper, for which the cyclic voltammogram can be seen in figure 3.22b. Different to the electrochemical behaviour with the addition of zinc, the addition of copper makes the anodic peak current increase gradually. It is shown that for an increasing concentration of copper, the peak will also increase. The dissolution of cobalt begins at a lower negative potential when the copper concentrations increase, which indicates that the cathodic current efficiency increases with increasing copper concentration (Elsherief, 2003).

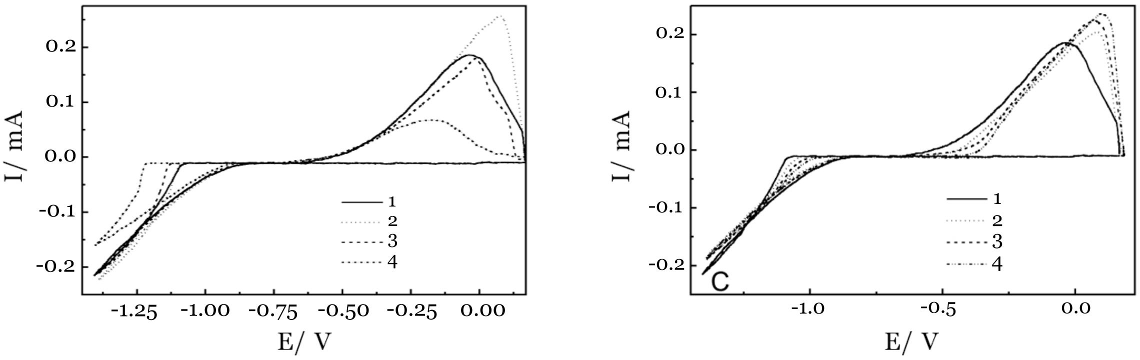

(a) Zinc conc.: (1) 0, (2) 300, (3) 500 and (4) 800 ppm

(b) Copper conc.: (1) 0, (2) 50, (3) 300 and (4) 800 ppm

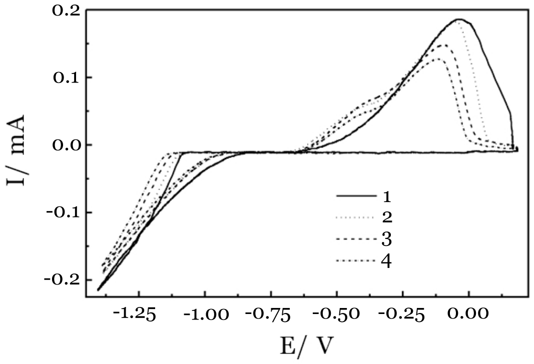

(c) Iron conc.: (1) 0, (2) 100, (3) 250 and (4) 400 ppm

Figure 3.22: Voltammograms for cobalt deposition and stripping in 60 g/l Co + 30 g/l boric acid, in presence of various (a) zinc, (b) copper and (c) iron concentrations at 100 mV/s, 20 °C (Elsherief, 2003)

For iron, the cyclic voltammogram can be seen in figure 3.22c. Here, the anodic current of the cobalt dissolution starts at a less positive potential, where the anodic peak decreases when the iron concentration is increased. Also, a gradual decrease in the anodic current peak indicates that the current efficiency in the cathodic process decreases with an increase in the iron concentration (Elsherief, 2003). When iron is present in the electrolyte, it is expected that hydrogen evolution will happen in the direct area of the cathode.

Overall, impurities will change the electrochemical behaviour of cobalt in an electrolyte solution. They exert an adverse effect on the current efficiency as it does upon the morphology and purity of the cobalt deposits (Elsherief, 2003). As is demonstrated with the addition of zinc, copper and iron, the profile of the cyclic voltammogram will be different. However, it is still hard to develop theories about the current efficiency and the deposition rates, since they cannot be read easily form these curves. This would require extra research in the future.

3.6. Simulated cyclic voltammetry

Besides chemical experiments, computer simulations of CV-data can be helpful to obtain additional information on the redox couple. Physical experiments using electrodes and electrolytes give the best answer to the electrochemical behaviour, however simulation can be useful for determining what effects changes to certain parameters will induce. Analysing the shape of the curve, peak shifts and amplitudes between the first cycle successive scans in the obtained cyclic voltammogram is an important key in providing useful information on the mechanisms of the electrochemical reaction (Semenova et al., 2018). The mechanisms that should be investigated properly are the flow rate, scan rate, varying supporting electrolyte, current density and the position of the electrode on the CV measurements (Adesokan et al., 2016). This can be modelled using Microsoft Excel and MATLAB.

3.6.1. Microsoft Excel

Brown (2015) developed a hands on simulator written in Microsoft Excel. The model investigates different potentials from the starting potential to the switching potential and vice-versa. To model this, many input parameters are needed to create the simulated output of the CV. First, the heterogeneous rate constants for the redox couple need to be calculated. Concentration gradients will be induced, which will result in diffusion. These concentration changes along the electrode surfaces must be calculated in order to know the diffusion coefficient. Parameters such as transfer coefficient, diffusion coefficients, potential values, faradaic current, fluxes for the oxidised and reduced forms, homogeneous rate constants, number of electrons, experiment time, temperature and scan rate are all needed to create a simulated cyclic voltammogram.

Excel is used to investigate parameters such as the scan rate, rate constant and different values for E_1 and E_2, which are different electronic couples for multiple redox reactions in one CV plot. Redox couples with a fast electron transfer tend to have a large value for k, where irreversible systems tend to have small values for k. As an example, cyclic voltammograms for different scan rates can be seen in figure 3.23a. The differences for a low k (irreversible system) and a high k (reversible system) is shown in figure 3.23b.

The same is investigated for different mechanisms of the reactions. Looking at two or more combined EC-mechanisms, it can be concluded that they require two separate values for the number of electrons (most of the times one or two), which controls the final shape of the overlapping waves in the cyclic voltammogram. When combining two wave forms, a so-called ECEC-mechanism is generated, where two homogeneous reactions remove portions of the two reduced components (Brown, 2015). These two redox couples both have a different formal potential, which can be changed in the model. If $E_1 < E_2$, a single two electron wave is generated located at the average value for E. When $E_1 > E_2$, two one-electron waves are generated. Both settings are shown in figure 3.23c.

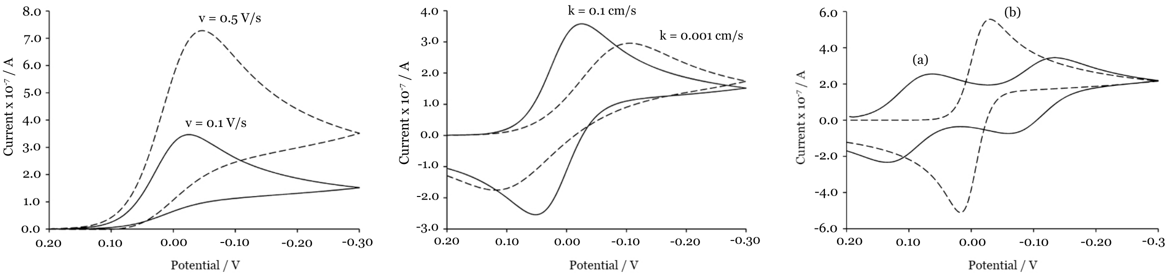

(a) Scan rate (v)

(b) Standard heterogeneous rate constant (k)

(c) Setting for first and second analogous couple in a series ($E_1 < E_2$)

Figure 3.23: Effect of changing different parameters *(a, b, c)* within graphical CV simulation (Brown, 2015)

3.6.2. MATLAB

Another way to create CV simulations is using MATLAB. (Wang et al., 2017) has developed an open-source user-friendly voltammetry simulator that requires no specific computational skills, besides some basic knowledge of MATLAB. The main features of this model are the reaction mechanisms, where four different mechanisms can be tested. Simulation parameters such as the initial concentration of the reactant, concentration, diffusion coefficient and temperature can be evaluated. The same outputs for a regular cyclic voltammogram as in figure 3.23 can be achieved, but on top of that the dynamical concentration profiles next to the electrodes can be generated. The profiles for two different times are shown in figure 3.24.

According to (Wang et al., 2017), in both profiles it can be seen that the oxidation reaction has consumed the reactant at the surface of the electrode, after which the current will be limited by the rate of transport and the reduction rate towards the working electrode. This limitation is shown in the cyclic voltammogram as a peak current. When the reaction is reversed, the reversed reaction of the oxidant into a reduction form gives a characteristic cathodic peak current. When the scan rate is higher (figure 3.24a), the concentration differs from the electrolyte to the surface over a more narrow region, which results in a larger current.

Attia (2018) also created a simulation tool for CV for a better understanding of the fundamentals of electrochemistry. It is based on the theories that can be found in Bard and Faulkner (2001), Appendix B. This model was tested in this thesis with the Excel spreadsheet in section 3.6.1. The model has the same functionality as the MATLAB model above, but this one can also be used online.

Overall, the simulation of CV can help to compare simulations and thus investigate the importance of certain parameters which can be changed in the physical experiments to gain better knowledge and understanding of the electrochemical behaviour of electrolytes.

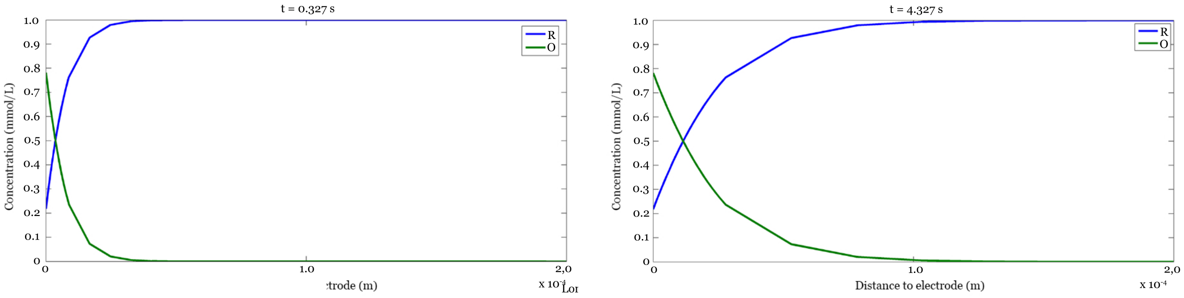

(a) **(b)**

Figure 3.24: Snapshots of diffusion profiles for the reversible electron transfer reaction at 32.7 mV (when the peak currents occur): (a) scan rate = 1 V/ s; (b) scan rate = 0.1 V/s (Wang et al., 2017)

4

Experimental setup and procedures

For the experiments carried out in order to obtain the results to answer the research questions, several experimental setups and procedures are used. All equipment has vital parts that can influence the electrochemical behaviour of the cobalt-electrolyte solution. This chapter evaluates the used equipment with their most important parts, together with important procedures that can influence the results of the experiments. The used equipment is based on the techniques evaluated in chapter 3. At the end of this chapter, the used experimental setup and parameters are given to introduce how the results are obtained.

4.1. Electrochemical cell

Using CV, an electrochemical cell is an essential part of the experiment. Normally, a vessel or beaker used in these experiments is called the electrochemical cell, which can be seen in figure 4.1. In the figure, all the different parts of the cell are shown. The most important parts are the working, counter and reference electrodes together with the electrolyte solution. Such a setting is also called a three-electrode cell and is commonly used in controlled-potential experiments, such as cyclic voltammetry (Wang, 2006). These four parts form the most valuable of the electrochemical experiment. To dissolve solvents into the electrolyte, a magnetic stirrer can be added to the setup, which is not shown in the figure. In the following sections the roles and influences of the four main elements on the experiments will be described.

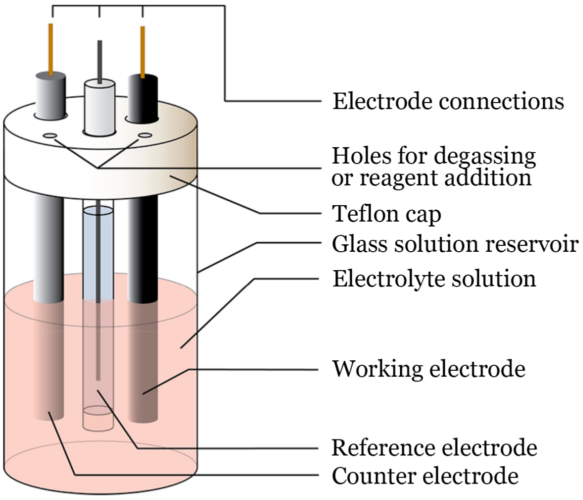
Electrode connections
Holes for degassing or reagent addition
Teflon cap
Glass solution reservoir
Electrolyte solution
Working electrode
Reference electrode
Counter electrode

Figure 4.1: Schematic representation of an electrochemical cell for cyclic voltammetry experiments (Rountree et al., 2018)

4.1.1. Electrolyte solution

While performing a CV experiment a migration of electrons occurs in a solution. Mostly a supporting electrolyte, called a salt, is dissolved in the solvent to reduce the resistance of the solution (Rountree et al., 2018). This combination of the solvent and the supporting electrolyte is, in most papers, called the "electrolyte solution". The supporting electrolyte is required to be highly soluble in the chosen solvent, is chemically inert and can be purified.

Furthermore, the choice of the solvent is primarily focused on the solubility of the analyte and its redox activity. Most important is that the solvent should not react with the chosen analyte and that it is not possible that the solvent can have an electrochemical reaction within the selected potential range, nor most preferably over a much wider range (Wang, 2006). For the supporting electrolyte, a buffer solution is useful for CV, since the pH influences the results of the experiment.

4.1.2. Working electrode

The working electrode (WE) carries out the electrochemical reaction that will be investigated. A current will flow through this electrode with the help of a potentiostat (section 4.2.1) as a function of the reference electrode (section 4.1.4). The most important parameter is that the material needs to be inert to make sure it will not take place in any reaction within the electrolyte solution. Different electrode materials will create different voltammograms, because they change the electron transfer kinetics. This makes it important to use the same material over multiple experiments to reduce measurement errors.

For this research a standard platinum working electrode (figure 4.3) is used with a purity of 99.95%. The outside diameter of the electrode is 6mm, where the working area is equal to 3mm ± 4%. The isolation is made out of polyether ether ketone (PEEK), which is a colourless organic thermoplastic polymer.

4.1.3. Counter electrode

The working electrode provides a potential through the electrolyte solution. When the potential is applied, a reaction will occur and a current begins to flow. The main use of the counter electrode is to complete the electrical circuit. When a reduction begins at the working electrode, an oxidation will occur at the counter electrode (CE). To insure the electrode has no impact on the reactions, an inert material is chosen.

For this research a standard platinum counter electrode (figure 4.4) is used with a purity of 99.95% with a length of 57mm. The wire diameter is equal to 0.5mm and the total surface area is ± 0.7 cm^2.

4.1.4. Reference electrode

A reference electrode (RE) has a well defined and stable equilibrium potential. It is used by the working electrode in combination with the potentiostat and the software to determine a reference point against which the potential of other electrodes can be measured. This can be seen in the plots, where the applied potential is compared with the potential of the reference electrode. The most common reference electrodes are the saturated calomel electrode (SCE), standard hydrogen electrode (SHE), and the AgCl/Ag electrode (Rountree et al., 2018).

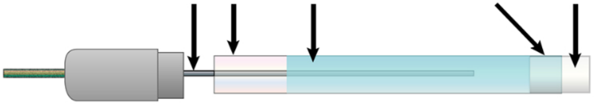

Figure 4.2: Schematic overview of the used reference Ag/AgCl electrode (Rountree et al., 2018)

For this research a Ag/AgCl reference electrode (figure 4.5) is used in combination with an ion permeable porous glass (IPPG) junction. The height is 78mm with a diameter of 6mm. The electrolyte in the reference electrode is a 3 M NaCl solution. This reference electrode consists out of silver wire in the solution containing an Na$^+$ salt, here a NaCl solution.

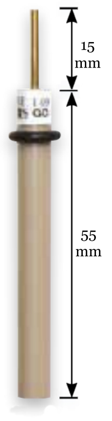

Figure 4.3: Standard type platinum working electrode

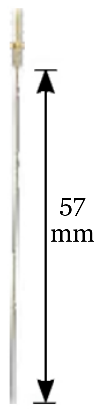

Figure 4.4: Platinum counter electrode

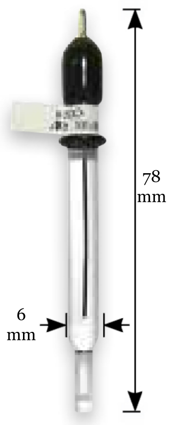

Figure 4.5: Small size Ag/AgCl reference electrode with 3 M NaCl electrolyte

4.1.5. Electrode polishing

The working, counter and reference electrodes will be used multiple times for similar experiments. In order to produce reliable and reproducible results (data) from the CVs, a well-polished working electrode is essential. Working electrodes should be polished directly before use, because even a few hours exposure to air will degrade the quality of the electrode surface and inhibit electron transfer. This will result in strange and unwanted features on the CV (Graham, 2018).

For this research, a PK-3 electrode polishing kit ordered from Bio-Logic is used, which is distributed by BAS Inc. The contents consist out of 20 ml of 0.05 µm polishing alumina, 10 ml 1 µm polishing diamond, 10 alumina polishing pads, 10 diamond polishing pads and one replacement glass plate for the kit.

To polish the working electrode, put some diamond paste (provided with the kit) on the polishing pad on the glass plate and drip 2-3 drops of polishing diamond on the pad, adding 2-3 drops of distilled water. The electrode is pressed on the pad at a right angle, and polished in a motion of drawing "8" shapes for a few minutes. Afterwards, the diamond pad needs to be replaced with the alumina polishing pad witch is moisturised with distilled water. Add 2-3 drops of polishing alumina and polish the electrode in the same method mentioned before until the mirror surface is regenerated. Rinse the electrode surface with distilled water and let the surface dry in the air.

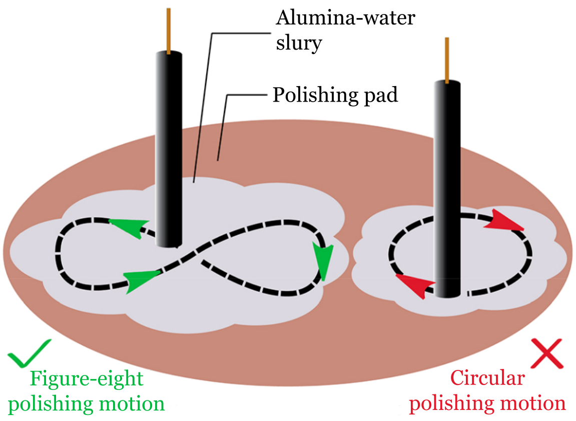

Figure 4.6: Schematic overview of how to polish a working electrode correctly (Rountree et al., 2018)

4.2. Equipment

Besides the parts needed for making the electrochemical cell, special equipment is needed to obtain the results from the CV and EQCM experiments. This section will describe the main principles and basic information of the techniques used for the research.

4.2.1. Potentiostat

For this research, a Bio-Logic SP-200 potentiostat (see Figure 4.7) is used. The SP-2XX series are known for their state-of-the-art modular research grade potentiostats with remarkable specifications, which include a flexible and modular potentiostat design. Furthermore, these are so-called "floating" instruments, which means that they can be used with grounded cells and autoclaves. The SP-200 offers a floating mode, analog filtering and a built-in calibration board, which makes it possible to use range of methods for electrochemical analysis. Figure 4.8 shows a schematic diagram of used potentiostat.

Figure 4.7: Bio-Logic SP-200 potentiostat

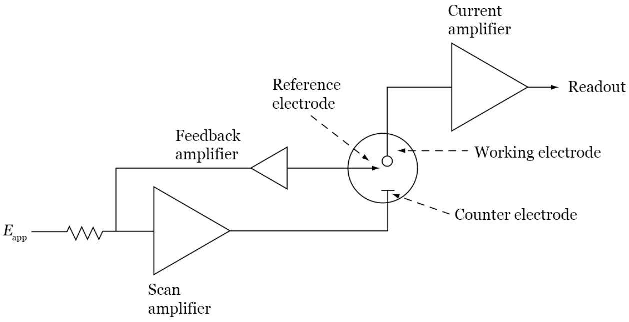
Current
amplifier
Readout
Reference
electrode
Feedback
amplifier
Working electrode
Counter electrode
E_{app}
Scan
amplifier

Figure 4.8: Schematic diagram of a three-electrode setup (Wang, 2006)

4.2.2. Electrochemical quartz crystal microbalance

For this research, the Seiko QCM922A is used (see Figure 4.9). This device offers high speed, and high sensitivity measurements of mass changes in electrochemistry. The instruments interface to potentiostats, flow cells etc., and include resonance frequencies from 5 MHz to 30 MHz, with 0.01 Hz resolution. For this research a 9.0 MHz platinum resonator electrode is used in combination with a lead wire, polished to a standard finish. Figure 4.10 shows a schematic diagram of used microbalance, where the added oscillator and frequency counter can be seen. These parts are added compared to a single potentiostat.

Figure 4.9: Seiko EG&G Quartz Crystal Microbalance (EQCM)

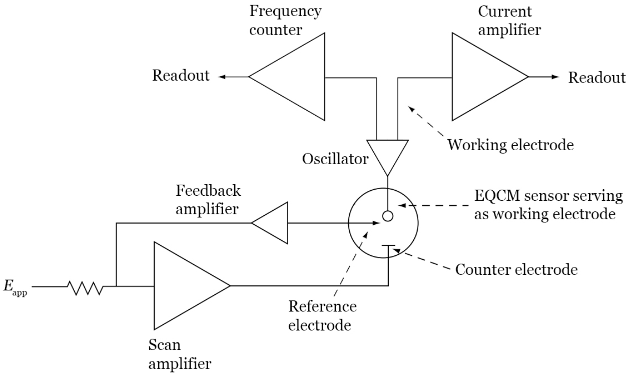
Frequency
counter
Current
amplifier
Readout
Readout
Working electrode
Oscillator
Feedback
amplifier
EQCM sensor serving
as working electrode
Counter electrode
E_{app}
Reference
electrode
Scan
amplifier

Figure 4.10: Schematic diagram of a three-electrode potentiostat including the EQCM (Modified from: Wang, 2006)

When the QCM is combined with with a potentiostat, it can be used as an electrochemical quartz crystal microbalance (EQCM). Combining this equipment can give valuable information about the electrochemical behaviour using the cyclic voltammetry technique, as well as the mass changes at the working electrode. The Quartz Crystal Resonator is placed in the dip cell that is used as the working electrode. The signal from the QCM resonator is sent to the SP-200 potentiostat and both CV and EQCM measurements are handled in EC-lab. An overview of the setup is shown in figure 4.11.

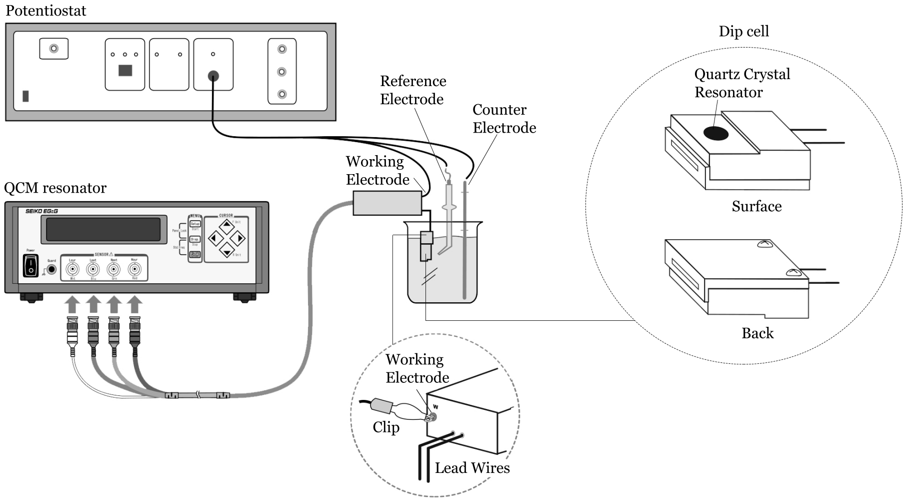

Figure 4.11: Schematic representation of the setup for a EQCM measurement (Modified from: Princeton Applied Research, 2007)

4.2.3. EC-Lab

To control the SP-200 potentiostat and Seiko EQCM, EC-Lab software is used. This is a common platform for controlling potentiostats, which enables the user to control several potentiostats from a single interface view. A variety of techniques is available. CV will be used the most in this research. For each technique, the corresponding parameter settings are shown as a series of boxes representing the building blocks of the experiment. This makes the software straight forward and easy to use. EC-Lab has an advanced external device configuration menu that can be configured to control and record data from a separate instrument, where in this case the EQCM will be used. The general interface is shown in figure 4.12, where a the setup for a CV experiment is shown. To begin a CV experiment, several parameters must be inserted (BioLogic, 2019):

- Set E_{we} sets the starting potential vs. reference electrode potential or vs. the open circuit potential (E_{oc}) or the previous controlled potential (E_{ctrl}) or measured potential (E_{meas}).
- Scan E_{we} with dE/dt sets the first potential sweep with measurement and data recording conditions which allows the user to set the scan rate in V/s, mV/s or mV/mn.
- To vertex potential E_1 sets the first vertex potential value vs. reference electrode potential or vs. the open circuit potential (E_{oc}) or vs. the potential of the previous experiment (E_i).
- Reverse scan to vertex E_2 runs the reverse sweep towards a second limit potential.
- Repeat n_c repeats the scan from E_i to E_1 and to E_2, n_c time(s). Note that the number of repetition does not include the first sequence: if $n_c = 0$ then the sequence will be run once; if $n_c = 1$ the sequence will be run twice, etc.
- Measure <I> over the last ... % selects the end part of the potential step (from 1 to 100%) for the average current (<I>) calculation.
- Record <I> averaged over N = ... voltage steps averages N current values on N potential steps, in order to reduce the data file size and smooth the trace.

- E range enables the user to select the potential range and to adjust the potential resolution according to the experiment.
- I range enables the user to select the current range. For controlled voltage techniques three kinds of current range are available on EC-Lab software: Auto, Auto Limited and fixed current ranges.
- Bandwidth enables the user to select the bandwidth (damping factor) of the potentiostat regulation.
- End scan to E_f gives the possibility to end the potential sweep or to run a final sweep with a limit E_f.

With the EC-lab software it is possible to connect external equipment and combine measurements from both CV and EQCM in one plot. The SP-200 potentiostat is provided with two auxiliary analog inputs. The instrument records two analog voltages as auxiliary signals. A specific menu in the EC-Lab software is created to modify the recorded signals in terms of label and unit to be the same as the original signals measured by the external device.

According to application note #15 (BioLogic, 2009), within EC-lab a special external device tab can be chosen. First, select the selected input channel used on the potentiostat in order to handle the right input signal. In device type select QCM and select "Seiko EG&G QCM922" as the device name. Analog Input 1 is now calibrated to record the frequency variations in Hertz. In these conditions, the entire potential range (0-10 V) is calibrated for the entire frequency or resistance range. No further conversion are needed, since the software will covert the E/V output to Δf displayed in Hz.

Afterwards, when the data output file is saved, the frequency can be converted to mass change with the help of the Sauerbrey equation by using the Analysis menu and selecting "Process Data". On the process window, the user must define the resonant frequency used for the experiment (obtained by calibration) and select "Delta(mass)/g" for calculations.

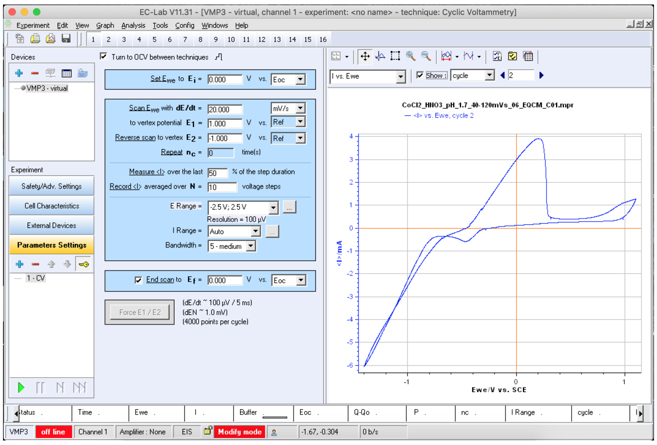
EC-Lab V11.31 - [VMP3 - virtual, channel 1 - experiment: <no name> - technique: Cyclic Voltammetry]
Experiment Edit View Graph Analysis Tools Config Windows Help
Devices
VMP3 - virtual
Experiment
Safety/Adv. Settings
Cell Characteristics
External Devices
Parameters Settings
1 - CV
I vs. Ewe
Show
cycle
CoCl2_HNO3_pH_1.7_40-120mVs_06_EQCM_C01.mpr
<I> vs. Ewe, cycle 2
<I>/mA
Ewe/V vs. SCE
Status Time Ewe I Buffer Eoc Q-Qo P nc I Range cycle
VMP3 off line Channel 1 Amplifier : None EIS Modify mode -1.67, -0.304 0 b/s

☑ Turn to OCV between techniques

Set E_{we} to E_i = 0.000 V vs. Eoc

Scan E_{we} with dE/dt = 20.000 mV/s
to vertex potential E_1 = 1.000 V vs. Ref
Reverse scan to vertex E_2 = -1.000 V vs. Ref
Repeat n_c = 0 time(s)

Measure <I> over the last 50 % of the step duration
Record <I> averaged over N = 10 voltage steps

E Range = -2.5 V; 2.5 V
Resolution = 100 µV
I Range = Auto
Bandwidth = 5 - medium

☑ End scan to E_f = 0.000 V vs. Eoc

Force E1 / E2
(dE/dt ~ 100 µV / 5 ms)
(dEN ~ 1.0 mV)
(4000 points per cycle)

Figure 4.12: Bio-Logic EC-Lab software including a CV-curve

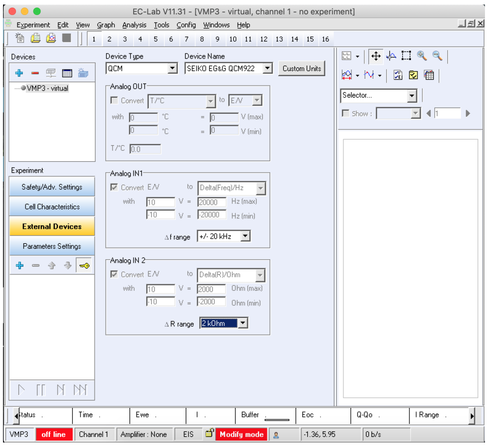
EC-Lab V11.31 - [VMP3 - virtual, channel 1 - no experiment]
Experiment Edit View Graph Analysis Tools Config Windows Help
Devices
VMP3 - virtual
Experiment
Safety/Adv. Settings
Cell Characteristics
External Devices
Parameters Settings
Custom Units
Selector...
Show
Status Time Ewe I Buffer Eoc Q-Qo I Range
VMP3 off line Channel 1 Amplifier : None EIS Modify mode -1.36, 5.95 0 b/s

Device Type: QCM
Device Name: SEIKO EG&G QCM922

Analog OUT
☐ Convert T/°C to E/V
with 0 °C = 0 V (max)
0 °C = 0 V (min)
T/°C 0.0

Analog IN1
☑ Convert E/V to Delta(Freq)/Hz
with 10 V = 20000 Hz (max)
-10 V = -20000 Hz (min)
Δf range +/- 20 kHz

Analog IN 2
☑ Convert E/V to Delta(R)/Ohm
with 10 V = 2000 Ohm (max)
-10 V = -2000 Ohm (min)
ΔR range 2 kOhm

Figure 4.13: External device configuration window

4.3. Experimental parameters

As seen in section 5.1, theoretically, different parameters have different influences on the behaviour of the voltammogram. To get a better and wider understanding of the reactions happening in the solution the following sections investigate the reaction parameters of man-made solutions, synthetic and ores from the Democratic Republic of Congo (DRC). This section evaluates the experimental parameters used for the experiments and how they are decided.

Using the knowledge from the mining overview, literature review and the experimental setup, all the involved parameters can be determined and used to obtain the results. The experiments were carried out in a glass cell, which contains a three-electrode setup. For the regular CV-measurements, the working electrode (WE) was a platinum (Pt) counter electrode. For the EQCM-measurements, the WE was a 9 MHz quartz crystal coated with a Pt film in contact with the electrolyte. The surface area of the resonator was A = 0.197 cm^2. The counter electrode (CE) was a Pt wire and all potentials are referred to a Ag/AgCl reference electrode. The resonance frequency shift was measured with a Seiko EG&G quartz crystal microbalance. The electrochemical measurements were conducted using a Bio-Logic SP200 potentiostat, which for the EQCM measurements is coupled to the socket of the resonator.

Both synthetic and DRC samples were leached using 0.5 M HNO_3. Gürmen and Friedrich (2004) investigated the best leaching conditions for the recovery of cobalt using acid leaching, and obtained the the optimal conditions, which were used for the experiments in this thesis. The ores were leached at 25 °C for two hours in a 0.5 M HNO_3 solution using a stirring speed of 900 round per minutes. At a higher temperature, the rate of cobalt leaching decreases. The leaching rate will also decrease when the HNO_3-concentration increases. A solid liquid ration of 0.75 grams per 60 mL was used, which can also be written as a S/L-ratio of 0.0125. The corresponding recovery curves are shown in figure 4.14.

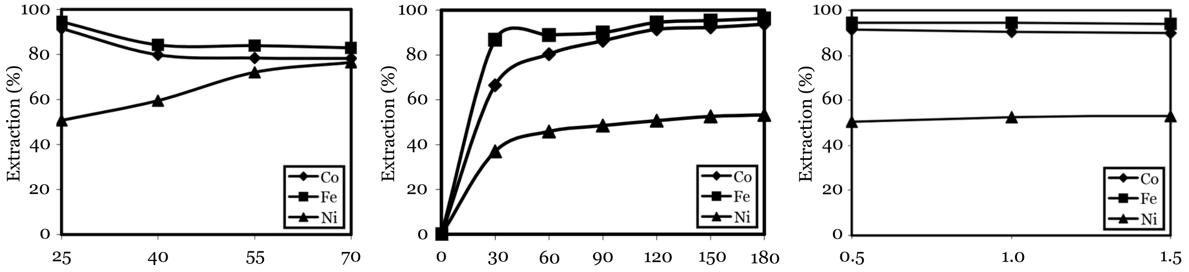

(a) Temperature (°C) (b) Reaction time (min), T = 25 °C (c) Acid concentration (M), T = 25 °C

Figure 4.14: Extraction percentages for cobalt, iron and nickel for different (a) temperatures, (b) reaction times and (c) HNO_3 concentrations (Modified from Gürmen and Friedrich, 2004)

For these conditions, the dissolution of cobalt is supposed to be as high as 91.5%. With a leaching time of two hours, the dissolution of cobalt is calculated to be 90.5%. Using an acid concentration of 0.5 M HNO_3, the extraction is 96% and with a stirring rate of 900 rpm, the extraction will be 92%. Using these parameters, it is expected to reach an overall extraction of 73%. Mohanty et al. (2018) investigated the extraction of copper, which was evaluated to be 79% for 1 M HNO_3 solution and 93% for 2 M HNO_3 solution. Extrapolation of these two points revealed that the estimated recovery for a 0.5 M HNO_3 solution can be assumed to be 65%.

5

Results

To understand the behaviour of a cyclic voltammogram, a sensitivity analysis using a cyclic voltammetry model can give an insight in how a diagram output changes when certain parameters change without performing any experiments in the lab. To do this, the behaviour of chemical reactions within the electrolyte solution, often the peak potentials with the scan rate of the diagrams are evaluated.

After the CV-simulations, several chemical compositions are evaluated to get an insight in the electrochemical behaviour of copper and cobalt elements when they occur in a more purified form. To do so, a 0.05 $CoCl_2$ solution to evaluate the electrochemical behaviour of pure cobalt in a solution is used. The same experiment is carried out with the addition of a 0.5 M HNO_3 solution to investigate a change in the CV and EQCM curves, because the synthetic and DRC-ores are also tested in the same environment. The same is done for a 0.05 M $CoSO_4$ and 0.05 M $CuSO_4$ solution to evaluate differences between two cobalt-bearing solutions and a pure copper solution.

After this, a combined solution of 0.05 M $CoCl_2$ and 0.05 M $CuSO_4$ is tested with and without the addition of HNO_3. This is done to investigate how the CV and EQCM curves variate when both substances are mixed in one solution. Both copper and cobalt occur in the DRC-ores and it is likely that both elements will leach using HNO_3, and will therefore be observed by both CV and EQCM experiments.

The last experiments include the synthetic and ores from the DRC. They are first leached in 0.5 M HNO_3 under conditions discussed in section 4.3. Afterwards they are evaluated using CV and EQCM experiments in acidic and alkaline environments to investigate their electrochemical behaviour and relevance to the other experiments.

5.1. Sensitivity analysis using CV-modelling

In this section, a sensitivity analysis presented for five different reaction parameters; the diffusion coefficient, initial concentration, the activity coefficient, the number of electrons involved in the reaction, and the temperature of the solution. First, the changes of the voltammogram are discussed, where after the change and relation of the peak potentials will be evaluated, using a graphical comparison. To generate the cyclic voltammograms, a mathematical model in MATLAB is used, created by Attia (2018), based on Appendix B of Bard and Faulkner (2001). After this section, the results continue with "real" experiments.

5.1.1. Diffusion Coefficient

The diffusion coefficient is a constant that measures the molar flux and the gradient in the concentration of the investigated electrolyte. For this constant, the higher the coefficient, the faster the two species will diffuse into each other and the faster the reaction occurs. With the help of the model, five values for the diffusion coefficient are evaluated. These values are 1.00×10^{-4}, 1.00×10^{-5}, 1.00×10^{-6}, 1.00×10^{-7} and 1.00×10^{-8} cm^2 s^{-1}. The output for the voltammograms are shown in figure 5.1. Figure 5.2 shows the peak densities for the investigated diffusion coefficients. Note that the x-axis is displayed as a logarithmic scale.

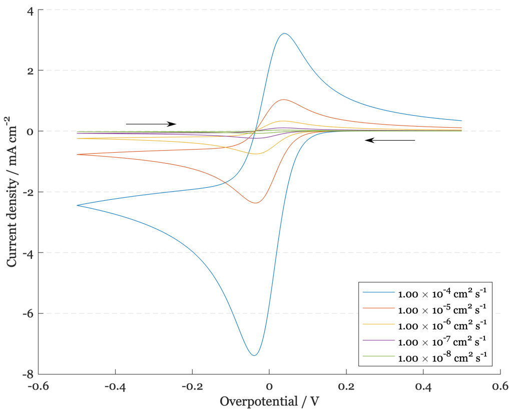

Figure 5.1: Modelled cyclic voltammograms for different values of the diffusion coefficient (D)

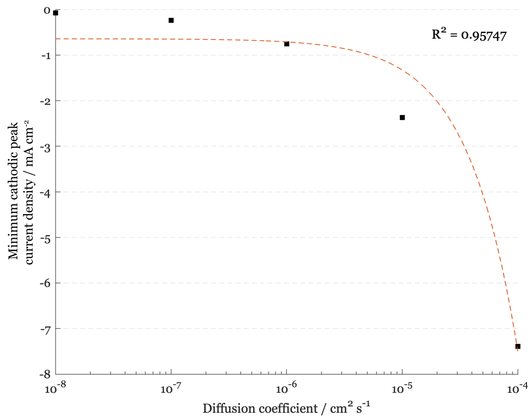

Figure 5.2: Cathodic peak current (V_{min}) vs. diffusion coefficient (D). X-axis is displayed as logarithmic scale

From figure 5.1, it can be seen that with a decreasing diffusion coefficient, the current densities of the peaks will become smaller. The shape of the voltammogram will stay approximately the same, since no major differences are observed. As mentioned above, the higher the diffusion coefficient, the easier and faster a reaction will occur. For a value for D of 1.00×10^{-4} cm^2 s^{-1}, the density peak is the highest, which indicates that if peaks increase, the reactions in the electrolyte solution will occur faster than when a smaller peak is observed. The applied overpotential will stay the same for different values for D, which indicates that this has no influence on the overpotential of the electrolyte. From figure 5.2 *(logarithmic x-axis)*, it can be concluded that there is a linear relationship between D and the peak of the current density. A trendline is plotted against the peak potentials, where a value for R^2 of 0.9575 is obtained.

5.1.2. Initial concentration

While making the electrolyte solution, the main task is to select an initial concentration to start the experiments. For analysing different electrolytes, it makes sense to investigate the initial concentrate and how the voltammograms will change in order to decide how much analyte is needed for a single experiment. If the output of higher initial concentrations is significantly better, higher concentrations will be used, which also means that more chemical compositions are needed. If lower concentrations give similar outputs, this is favourable since less chemical compositions are needed, and costs can be lowered. With the help of the model, five values for the initial concentration are evaluated. These values are 0.50, 1.00, 1.50, 2.00 and 2.50 mol cm^{-3}. The output for the voltammograms are shown in figure 5.3. Figure 5.4 shows the peak for the current densities for the investigated initial concentrations of the electrolyte.

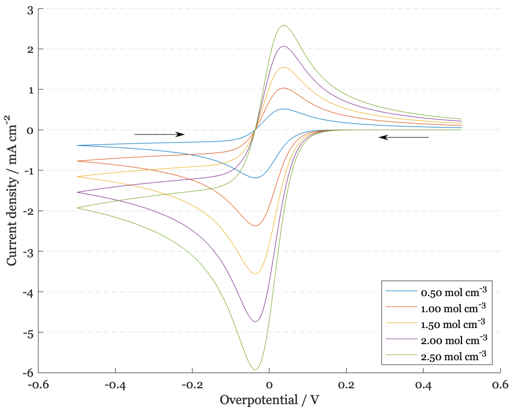

Figure 5.3: Modelled cyclic voltammograms for different values of the initial concentration (C_O)

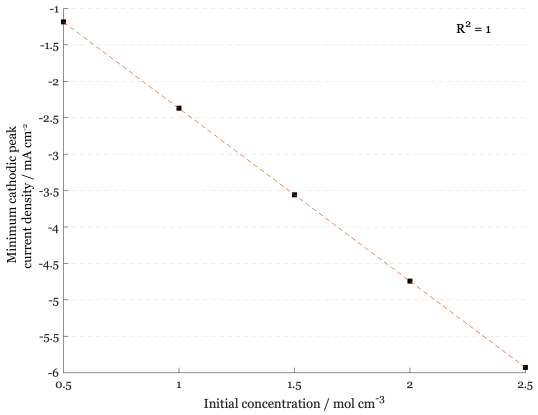

Figure 5.4: Cathodic peak current (V_{min}) vs. initial concentration (C_O)

From figure 5.3, it can be seen that with an increasing initial concentration, the current density of the peaks will increase. The shape of the voltammogram does not change significantly and the values for the overpotential remain constant. This indicates that for analytical research of the voltammograms, the initial concentration of the solution is not a limiting factor, as cyclic voltammetry experiments are mainly carried out for the value of the overpotential. Therefore a minimal initial concentration is needed to obtain information about the electrochemical behaviour of the solution. Furthermore, the changes in current density are larger when compared with the other parameters investigated in this section. From figure 5.4, it can be concluded that there is a perfect linear relationship between C_O and the peaks of the current density. A trendline is plotted against the peak potentials, where a perfect value for R^2 of 1.00 is obtained.

5.1.3. Charge-transfer coefficient

The charge-transfer coefficient or transfer coefficient (α) is a measure for the symmetry of the voltammogram. The optimal value for $\alpha$is 0.5, which indicates that the left and right hand side of the voltammogram are symmetrical. For a value lower than 0.5, the voltammogram is more skewed to the right and for values higher than 0.5, the voltammogram is more skewed to the left. Typical values for αlie between 0.3 and 0.7. If a measured voltammogram does not show any symmetry, the charge-transfer coefficient can explain differences in the shape of the plot. With the help of the model, five values for the charge-transfer coefficient are evaluated. These values are 0.01, 0.25, 0.50, 0.75 and 0.99. The transfer coefficient does not have any dimension. The output for the voltammograms are shown in figure 5.5. Figure 5.6 shows the peak for the current densities for the investigated charge-transfer coefficients of the electrolyte.

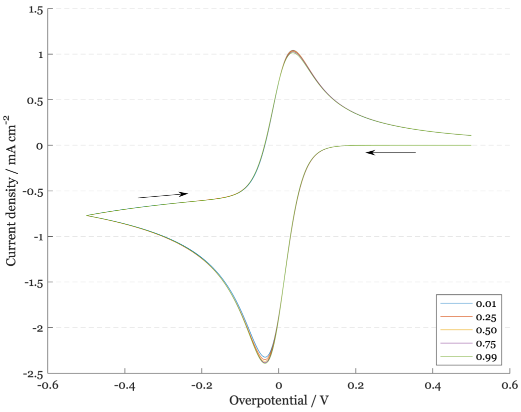

Figure 5.5: Modelled cyclic voltammograms for different values of the charge-transfer coefficient (α)

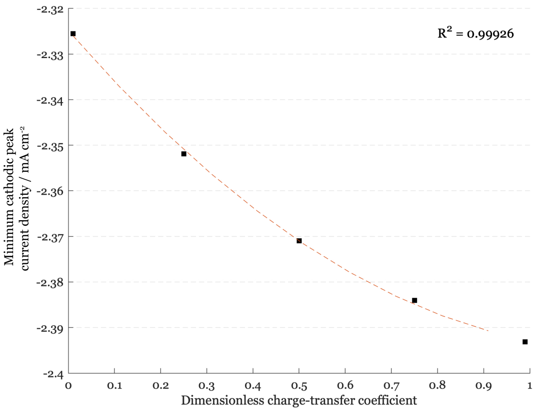

Figure 5.6: Cathodic peak current (V_{min}) vs. charge-transfer coefficient (α)

In figure 5.5, it can be seen that the different values for αhave minor influence on the shape of the voltammogram. For a higher transfer coefficient, the peak of the current density will increase slightly. However, between the minimum (0.01) and maximum (0.99) value for α, the current densities for the peaks differ less than 0.1 mA cm^{-2}. The values for the over-potentials stay constant when the values for αdiffer. This indicates that the charge-transfer coefficient has minor influence on the behaviour of the cyclic voltammogram. From figure 5.6, it can be concluded that there is an exponential relationship between $\alpha$and the peaks of the current density. A trendline is plotted against the peak potentials, where an almost perfect value for R^2 of 0.99 is obtained.

5.1.4. Number of electrons transferred

In the electrolyte solution, the redox reactions can involve different numbers of electrons. For example, the reaction $Co^{2+} + 2\,e^- \longrightarrow Co(s)$ involves two electrons. Using the model, five values for the number of electrons transferred are evaluated. These values are 1, 2, 3, 4 and 5. The number of electrons that are involved do not have any dimension. The output for the voltammograms are shown in figure 5.7. Figure 5.8 shows the peak for the current densities for the investigated charge-transfer coefficients of the electrolyte.

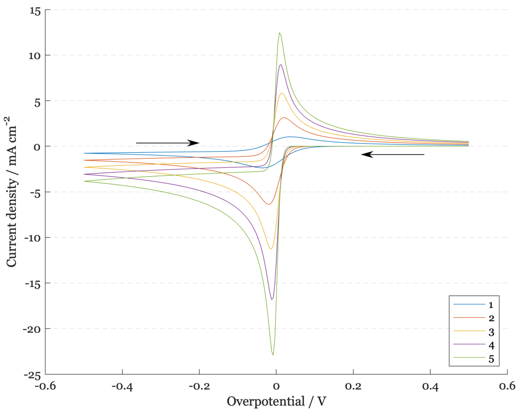

Figure 5.7: Modelled cyclic voltammograms for different values of the number of transferred electrons (n)

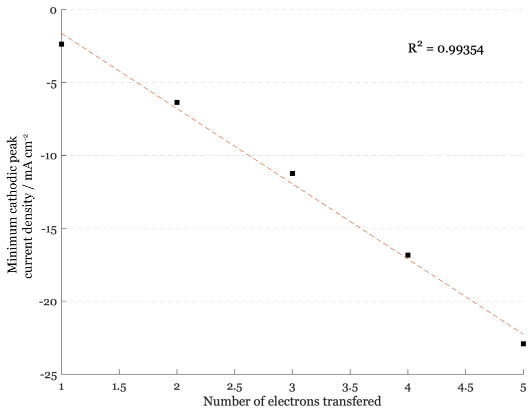

Figure 5.8: Cathodic peak current (V_{min}) vs. number of transferred electrons (n)

Typical values for the number of electrons that are involved are 1, 2 or 3. However, to show the effect of higher amounts and to create a better analysis using the trendline, values of 4 and 5 are also included in the plot shown above. As can be seen in figure 5.7, when the number of transferred electrons increase, the current density peaks increase significantly. Between the lowest (1) and highest (5) number of electrons transferred, a difference of more than 20 mA cm^{-2} is observed. This indicates that this parameter has a major influence on the behaviour of the voltammogram. The peaks increase, but the value for the overpotential remains constant, which indicates that the number of electrons does not effect the characteristic overpotential for the electrolyte. From figure 5.8, it can be concluded that there is a linear relationship between n and the peaks of the current density. A trendline is plotted against the peak potentials, where an almost perfect value for R^2 of 0.99 is obtained.

5.1.5. Temperature

Temperature is an important parameter for cyclic voltammetry experiments. Generally, an increase in temperature results in accelerating the deposition process and the promotion of a substance at the electrode of the cell. It can also change the kinetic parameters such as the diffusion coefficient and adsorption parameters. For the deposition of species, it is important to know what the differences are for variable temperatures. If a reaction is more efficient for a higher temperature, this does not directly say that this is more favourable. If a solution needs to be heated to a certain temperature, this will result in extra heating costs which can be less favourable in the end. Five temperatures are evaluated, 283.15, 298.15, 323.15, 348.15 and 363.15 K. These temperatures are equal to 10, 25, 50, 75 and 90 °C. The output for the voltammograms are shown in figure 5.9. Figure 5.10 shows the peaks for the current densities for the investigated temperatures.

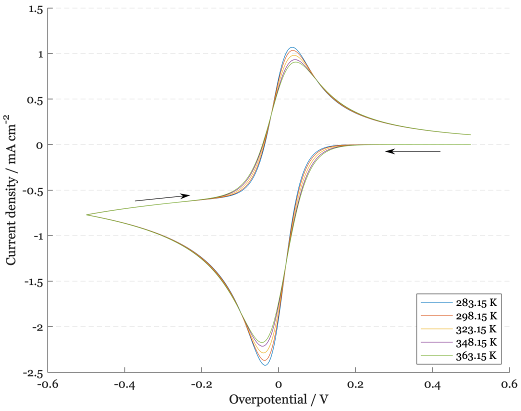

Figure 5.9: Modelled cyclic voltammograms for different values of the temperature (T)

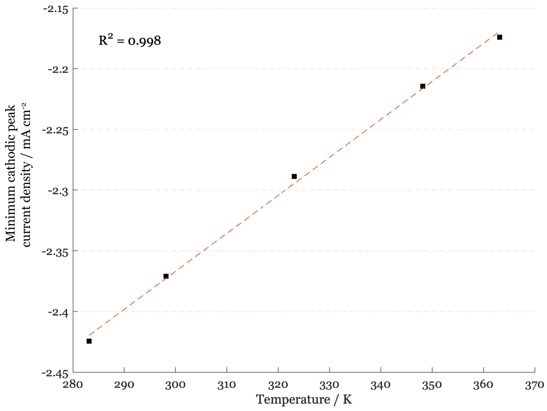

Figure 5.10: Cathodic peak current (V_{min}) vs. temperature (T)

As shown in figure 5.9, the voltammograms do not differ significantly when the temperature is changed. When the temperature is increased, the peak of the current density decreases. This is in contrast to the previous parameters, where an increase of the parameters resulted in an increase in the peak potential. The maximum or minimum peak do not vary much when the temperature is changed. The differences between the lowest (298.15 K, 25 °C) and highest (363.15 K, 90 °C) temperature is less than 0.30 mA cm^{-2}. This indicates, that if solely the temperature is changed, no major changes are observed in the voltammogram. From figure 5.10, it can be concluded that there is a linear relationship between T and the peaks of the current density. A trendline is plotted against the peak potentials, where an almost perfect value for R^2 of 0.99 is obtained.

5.2. Cobalt chloride

As a first experiment, the reduction and oxidation mechanisms of cobalt chloride ($CoCl_2$) are evaluated. For this experiment $CoCl_2 \cdot 6\,H_2O$ was used, produced by BDH Chemicals Ltd. The used electrolyte was produced only with $CoCl_2$ and demineralised water by stirring the mixture at room temperature until a homogeneous red/pinkish coloured liquid was formed, which is mixed as a 0.05 M chCoCl2 solution. A single voltammogram of the solution for $\nu = 50\ \mathrm{mV\,s^{-1}}$ is shown in Figure 5.11.

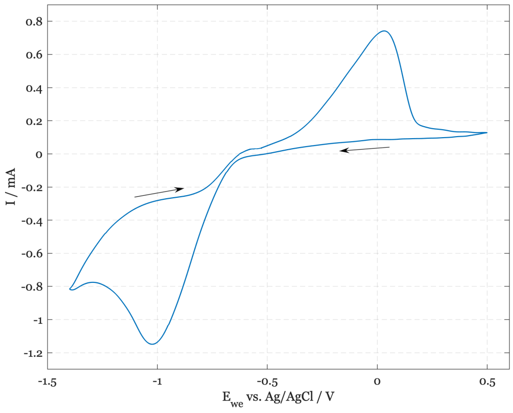

Figure 5.11: Single voltammogram using 0.05 M $CoCl_2$ at 298K, $\nu = 50\ \mathrm{mV\,s^{-1}}$

Figure 5.12 shows the voltammograms for different scan rates of the solution, which makes it possible to obtain the reaction parameters. Two major peaks are visible, at the cathodic scan around -1.10 V and on the anodic direction of the scan at 0.10 V. The current densities of the cathodic peaks are plotted in figure 5.13, where a linear relationship is visible. Using this data, the value for α is equal to 0.11, the diffusion coefficient is $8.82 \times 10^{-6}\ \mathrm{cm^2\,s^{-1}}$, and k_s is $1.48 \times 10^{-6}\ \mathrm{cm\,s^{-1}}$, which indicates the reaction is irreversible. During the reduction phase in the cathodic direction of the scan a black greyish deposit was observed at the electrode and probably induced by the reduction of cobalt.

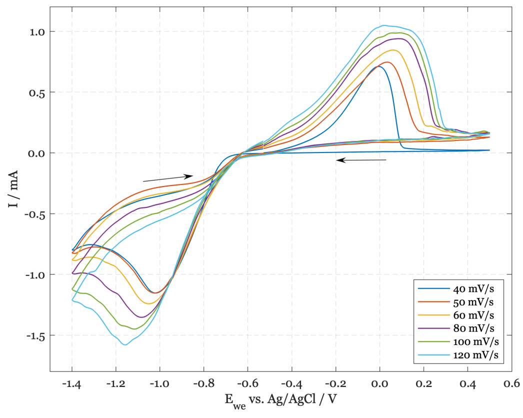

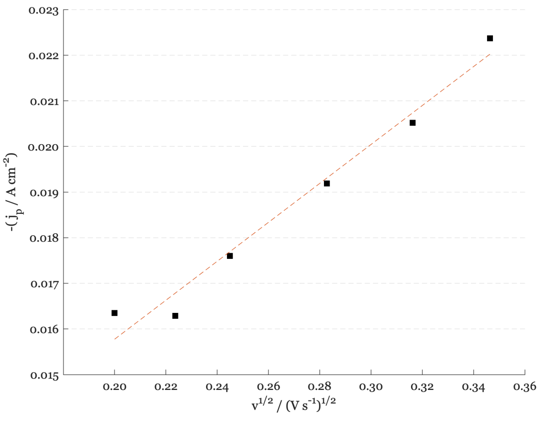

Figure 5.12: Voltammogram for 0.05 M $CoCl_2$ at 298 K under different scan rates at pH of 5.80

Figure 5.13: Cathodic peak current densities of voltammogram for 0.05 M $CoCl_2$ at 298 K under different scan rates

When CV measurements are combined with the EQCM, a convenient tool is used to investigate the electrochemical reactions; changes in the frequency can be converted to mass changes using the Sauerbrey equation. To investigate its behaviour and to show the presence of cobalt can proven, potentiodynamic (changing potential) and potentiostatic (constant potential) measurements are carried out.

In figure 5.14, two cycles of the CV are shown together with frequency change on the quartz resonator. When the CV shows a reduction process when current (I) is below 0 mA, a decrease in frequency is visible. Particle deposition at the quartz resonator make the frequency decrease due to an increase in mass on the surface of the electrode. During an oxidation process, when the current peak (I_p) is shown, an increase in frequency change is visible. Using the Sauerbrey equation, the frequency changes are converted to mass change, what can be seen in figure 5.15. The Sauerbrey equation reverses the graph and creates a y-axis displayed as µg.

Figure 5.15 shows that the mass at the electrode starts at 0 µg and increases after the first cycle to ± 24 µg. Then an oxidation phase is introduced, which starts a mass decrease to ± 10 µg. This also indicates that this reaction is not reversible, since after one cycle, the electrodeposited materials are not completely reduced. Otherwise, the mass diagram will show a continues cycle of the mass increase and decrease. After the second cycle, a maximum mass of ± 34 µg is generated, which indicates a change in mass per unit area of 173 µg cm^{-2}. Figure 5.14 shows a deposit of cobalt building up at the electrode surface, something that is also visible at the surface of the electrode after the experiment had finished.

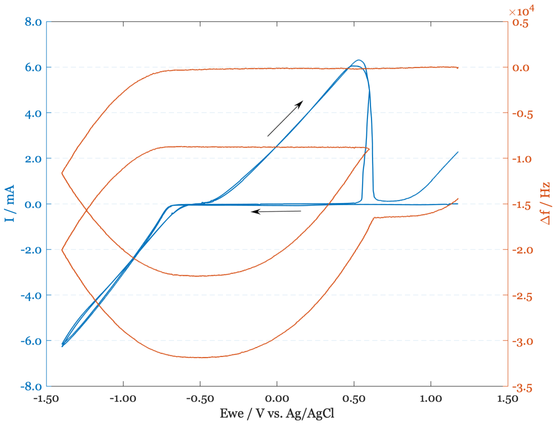

Figure 5.14: Cyclic voltammogram (—) for 0.05 M $CoCl_2$ solution and corresponding frequency change (—)

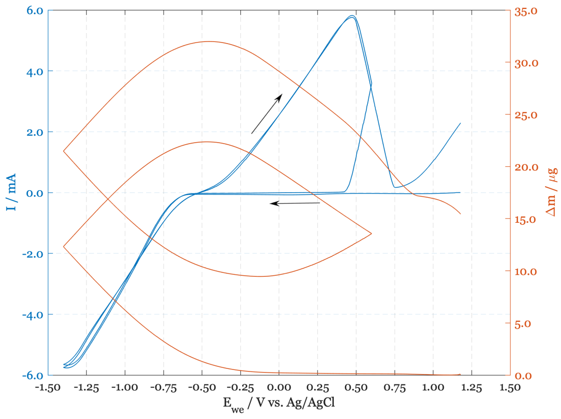

Figure 5.15: Cyclic voltammogram (—) for 0.05 M $CoCl_2$ solution and corresponding mass change (—)

In this experiment, the only possible option for the electrodeposited material is cobalt, since only a $CoCl_2$ solution is used. However, in following experiments mixed chemicals will be tested. Therefore, this section can be seen as an introduction. Figure 5.16 shows the frequency versus charge curve. Different slopes can be seen, which with the help of equation 3.24 can be converted into the molar mass divided by the amount of electrons involved. Every slope has a characteristic value for the reaction taking place in the electrolyte.

The pH of the solution was measured to be 5.80. Matsushima et al. (2006) suggests that when using a pH above 4.00, no water molecules are visible in the reactions and direct electrodeposition of cobalt will occur. Table 5.1 shows the values for M/z, the molar mass divided by the number of electrons involved, for different potential ranges shown in figure 5.14. This confirms that no hydrogen reaction is involved, since the value for M/z of H_2O is equal to 9.00, when two electrons are considered. The direct electrodeposition of cobalt is $Co^{2+}(aq) + 2\,e^- \longrightarrow Co(s)$. The molar mass of cobalt is 58.93 u, so the M/z value is equal to 58.93 divided by 2, which results in an $M/z_{(Co)}$ equal to 29.53, considering two electrons involved. The same value applies for the direct dissolution of cobalt.

From the values in table 5.1, it can be seen that all values are close to $M/z_{(Co)}$ of 29.5. An optimal and perfect value is not reached, which is most likely due to current efficiency that is lower than 100%. The current efficiency of the reactions from table 5.1 can be calculated to vary between 73 and 88%. So overall it is proved that the element involved in the reaction is cobalt and that analysis of the EQCM data during the deposition of cobalt concluded that no hydrogen was involved in one of the reactions. It is proved that this technique is a powerful tool to investigate elements involved in the reactions and what effects changes in the electrolyte will have on the plots of the CV and EQCM measurements.

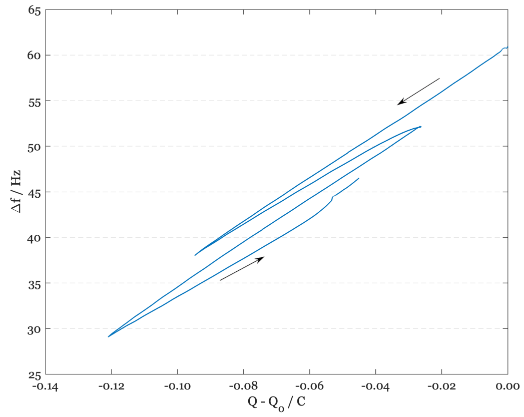

Figure 5.16: Frequency variation as a function of charge

Table 5.1: M/z found by fitting the slope of the frequency versus charge for cobalt deposition of $CoCl_2$ solution at pH= 5.80

pH	Potential range (V)			M/z ($g mol^{-1}$)
5.80	1.20	to	−1.40	25.2 ± 0.5
	−1.40	to	−0.67	25.0 ± 0.5
	−0.67	to	0.47	22.3 ± 0.5
	0.47	to	−1.40	24.4 ± 0.5
	−1.40	to	−0.52	26.0 ± 0.5
	−0.52	to	0.62	21.5 ± 0.5

5.3. Cobalt chloride in nitric acid

For the liberation of cobalt from the ores coming from the Mutanda mining operation discussed in section 5.8, a diluted HNO_3 solution is used to leach the ore. To investigate the influence and differences of the $CoCl_2$ solution tested in the previous section, HNO_3 is added to investigate differences between both setups. Figure 5.17 shows the voltammograms for different scan rates of the solution.

Two major peaks are visible, at the cathodic scan around -1.10 V and on the anodic direction of the scan at 0.10 V. The current densities of the cathodic peaks are plotted in figure 5.18, where a linear relationship is visible. Using this data, the value for α is equal to 0.12, the diffusion coefficient is $6.15 \times 10^{-6}\,cm^2\,s^{-1}$, and k_s is $1.48 \times 10^{-6}\,cm\,s^{-1}$, which indicates the reaction is quasi-reversible.

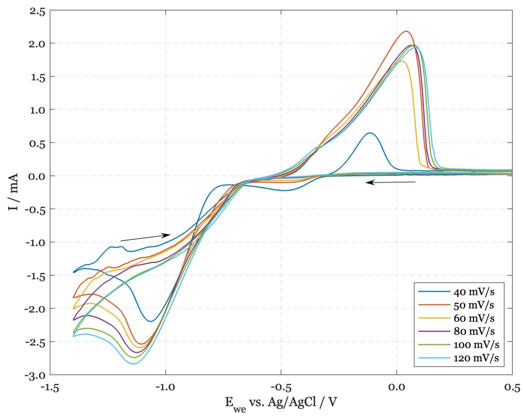

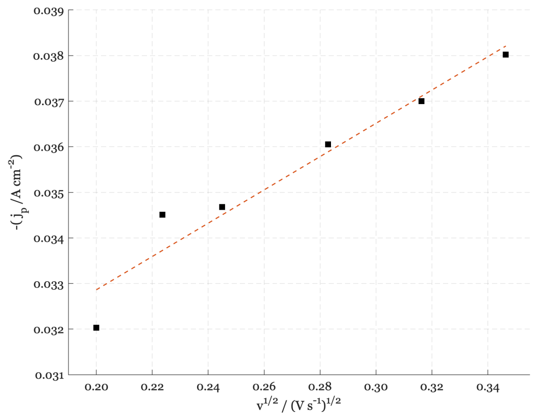

Figure 5.17: Cyclic voltammogram using a 0.05 M $CoCl_2$ in 0.5 M HNO_3 at 298 K under different scan rates

Figure 5.18: Cathodic peak current densities of voltammogram in 0.05 $MCoCl_2$ in 0.5 M HNO_3 at 298 K

Using the EQCM, the deposition rate of the solution is shown in figure 5.19. During the scan in the cathodic direction, the mass increases to a maximum of 18.4 µg, which indicates a change in mass per unit area of 93.9 µg cm^{-2}. After the mass increase, during the anodic peak the mass reduces back to 0 grams at 0.50 V. Using the values for M/z is used to determine the involved reactions. These values can be seen in table 5.2. Since the pH is low, the deposition of cobalt with adsorbed hydrogen is expected to be seen/found, which has a characteristic M/z value of 15.3. Between the 1.10 to 0.80 V and -0.25 to -0.69 V window this reaction is present. The large drop in the cathodic direction in figure 5.19 is characterised by an M/z value of 41.6, which is closer to 29.5, the M/z value for direct cobalt electrodeposition.

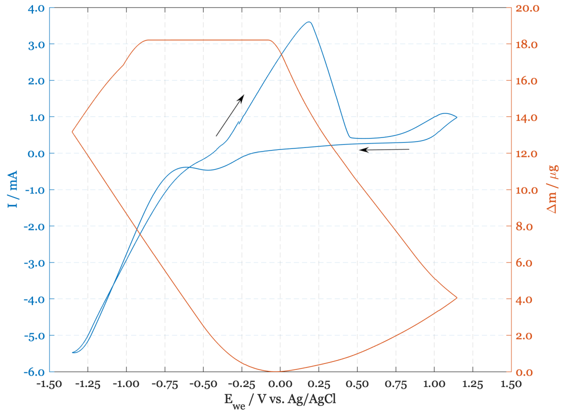

Figure 5.19: Cyclic voltammogram (—) for 0.5 M $CoCl_2$ solution in 0.5 M HNO_3 and corresponding mass change (—)

Table 5.2: M/z values for cobalt deposition of 0.05 M $CoCl_2$ added with HNO_3 up to pH = 1.70

pH	Potential range (V)			M/z ($g\,mol^{-1}$)
1.70	−0.32	to	0.06	0.1 ± 0.5
	0.06	to	0.28	39.3 ± 0.5
	0.28	to	0.81	115.5 ± 0.5
	0.81	to	1.10	49.1 ± 0.5
	1.10	to	0.80	14.8 ± 0.5
	0.80	to	−0.25	64.1 ± 0.5
	−0.25	to	−0.69	16.3 ± 0.5
	−0.69	to	−1.31	41.6 ± 0.5
	−1.31	to	−1.40	0.1 ± 0.5
	−1.40	to	−0.32	0.1 ± 0.5

5.4. Cobalt sulfate

To confirm the electrochemical behaviour of cobalt, $CoSO_4$ is investigated in the same way as $CoCl_2$ in section 5.3. In this section, the voltammograms of $CoSO_4$ are evaluated, which can be seen in figure 5.20. Figure 5.21 shows the cathodic peak current densities. For this solution, no experiments are carried out with the EQCM-technique, because no extra valuable information will be obtained from these figures. The behaviour of $CoSO_4$ in HNO_3 did not show significant differences.

As with the $CoCl_2$ solution, two major peaks are visible: at the cathodic scan around -1.10 V and on the anodic direction of the scan at 0.10 V. From the cathodic peaks, the current densities are plotted in figure 5.21. A linear relationship is visible. Using this graph, the value for α is equal to 0.09, the diffusion coefficient is $1.10 \times 10^{-6}\,cm^2\,s^{-1}$, and k_s is $3.48 \times 10^{-7}\,cm\,s^{-1}$, which indicates the reaction is irreversible.

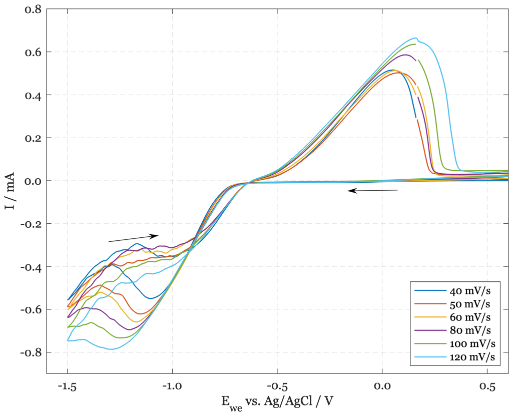

Figure 5.20: Cyclic voltammogram of 0.1 M $CoSO_4$ for varying scan rates between 40 and 120 mV/s at 298 K

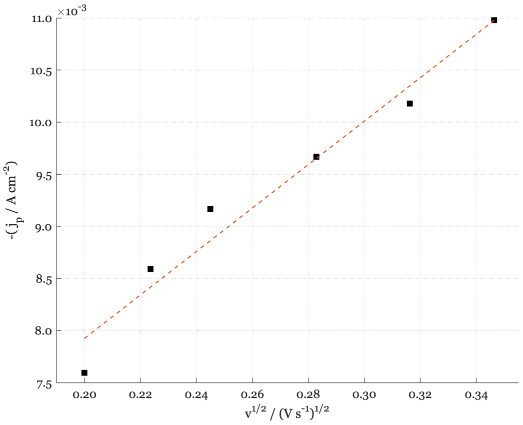

Figure 5.21: Cathodic peak current densities of CV curve for 0.05 M $CoSO_4$ at 298 K for different scan rates

5.5. Copper sulfate

When HNO_3 is used as a leaching agent for the Mutanda ores, large quantities of copper will be available from the mineral. The copper in these minerals will dissolve together with the cobalt bearing minerals and will form a leach solution. To explain possible peaks of copper deposition and dissolution in section 5.8, a solution of $CuSO_4$ is evaluated. As in the previous sections, a solution of 0.1 M $CuSO_4$ is tested for varying scan rates to obtain the electrochemical reaction parameters. For this solution, no experiments are carried out with the EQCM-technique, because no extra valuable information will be obtained from these figures.

Figure 5.22 shows the voltammogram for $CuSO_4$, where two major peaks are observed. One in the cathodic direction of the scan at -0.45 V and one in the anodic direction of the scan around 0.78 V. These peaks are related to the direct deposition (cathodic) and dissolution (anodic) of copper at the surface of the electrode since this is the only element available. To obtain the reaction parameters, the cathodic peaks are plotted against the square root of the scan rate, shown in figure 5.23. A linear relationship is visible, which gives reliable reaction parameters. Using this graph, the value for α is equal to 0.09, the diffusion coefficient is $1.02 \times 10^{-7}\ \mathrm{cm^2\,s^{-1}}$, and k_s is $3.50 \times 10^{-8}\ \mathrm{cm\,s^{-1}}$, which indicates the reaction is irreversible.

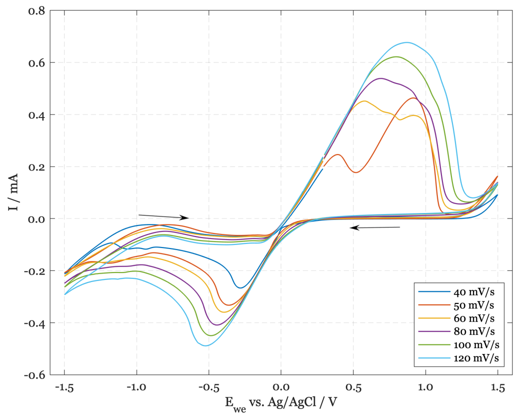

Figure 5.22: Cyclic voltammogram of 0.1 M $CuSO_4$ for varying scan rates between 40 and 120 mV/s at 298 K

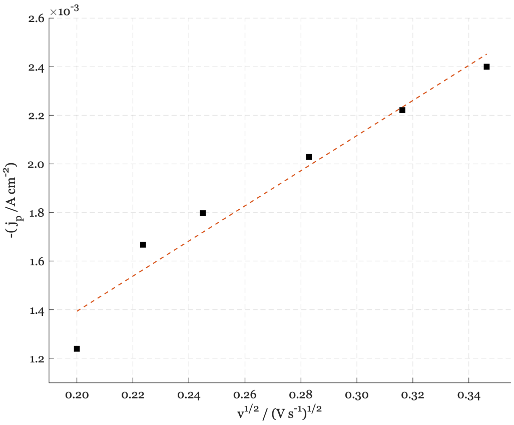

Figure 5.23: Cathodic peak current densities of CV curve for 0.05 M $CuSO_4$ at 298 K for different scan rates

Because the leaching will occur in acidic conditions, the voltammogram of a 0.1 M $CoSO_4$ in a solution of 0.5 M HNO_3 is evaluated in the potential window from -0.60 V to 1.00 V. This window is smaller than the CV done without adding HNO_3 because no distinctive peaks were observed in figure 5.24 and the cathodic peak will decrease into infinity. Figure 5.24 shows the voltammogram, which has similarities wtih the characteristic voltammogram for a 0.5 M HNO_3 solution. Compared to figure 5.22, no peaks are observed around the -0.50 V and 0.80 V potential, which explains that no reactions involving copper, or any other element, occur within the solution. One reason that no active species is observed, is that the concentration of acid was to high or that the concentration of the $CuSO_4$ was too low to start a reaction in the solution. In section 5.8 it will become clear whether copper is observed at all, since the EQCM is used in order to detect a mass increase at the electrode and possibly discover the characteristic M/z values for (direct) deposition of copper solids.

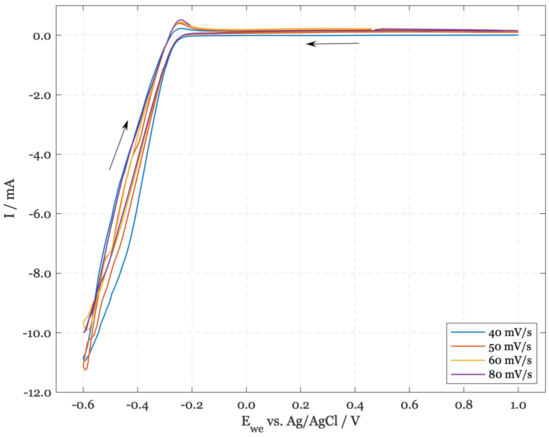

Figure 5.24: Cyclic voltammogram of 0.1 M $CuSO_4$ in 0.5 M HNO_3 for varying scan rates between 40 and 80 mV/s at 298 K

5.6. Cobalt chloride with copper sulfate

Because copper and cobalt bearing elements are present in the minerals together, it is expected that during the leaching procedure both copper and cobalt will dissolve and enter the solution. The experiment with both $CoCl_2$ and $CuSO_4$ is used to distinguish the differences in the voltammogram compared to solution with only $CoCl_2$ or $CuSO_4$. The experiments are carried out using both CV and EQCM, as well as at pH levels above and below 4.00 (5.60 and 1.50), which according to literature is supposed to be the threshold copper/cobalt dissolution with adsorbed hydrogen.

Figure 5.25 shows the voltammogram for $CoCl_2$ and $CuSO_4$ at pH 5.60, where three peaks are observed in the cathodic direction of the scan. The first peak is observed around 0.00 V, the second around -0.20 V and the last one, only for the 40 mV/s scan, at -1.10 V. These peaks are related to the deposition of copper and cobalt, which will be confirmed by the EQCM later. In the anodic direction of the scan, one major peak is visible around 0.35 V. The scan for 30 mV/s shows two anodic peaks at 0.25 V and 0.60 V.

To obtain the reaction parameters, the cathodic peaks are plotted against the square root of the scan rate, shown in figure 5.26. A linear relationship is visible for the last five points, whereas the first does not fit in the trendline. This gives reaction parameters that are less reliable. Using this graph, the value for α is equal to 0.25, the diffusion coefficient is $4.34 \times 10^{-8}\,cm^2\,s^{-1}$, and k_s is $1.66 \times 10^{-8}\,cm\,s^{-1}$, which indicates the reaction is irreversible.

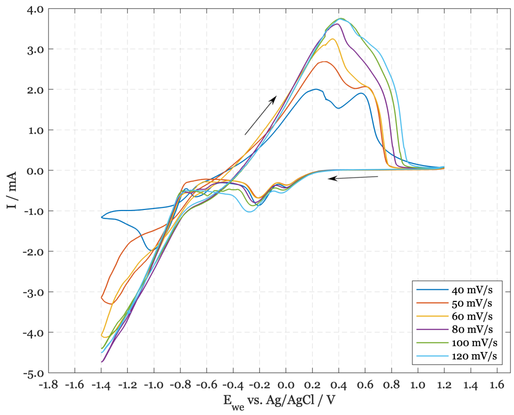

Figure 5.25: Voltammogram for 0.05 M $CuSO_4$ and 0.05 M $CoCl_2$ for scan rates between 40 and 120 mV/s at pH 5.6

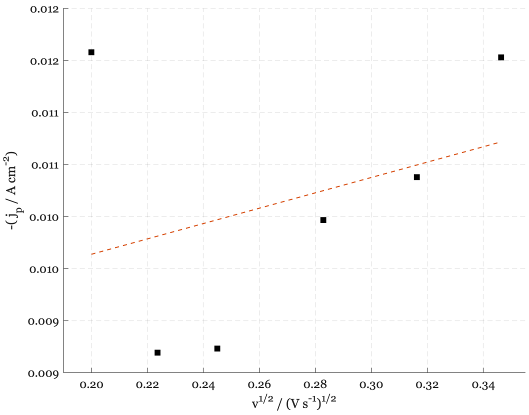

Figure 5.26: Cathodic peak current densities of CV curve for 0.05 M $CuSO_4$ and 0.05 M $CoCl_2$ at pH 5.6

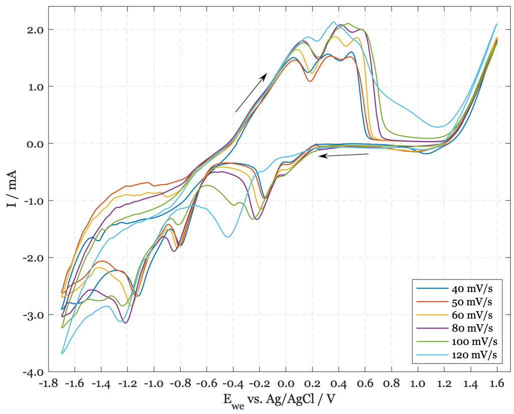

Figure 5.27: Voltammogram for 0.05 M $CuSO_4$ and 0.05 M $CoCl_2$ for scan rates between 40 and 120 mV/s at 298 K at pH 1.5

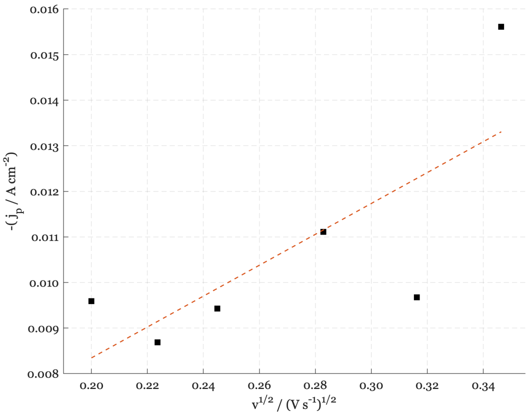

Figure 5.28: Cathodic peak current densities of CV curve for 0.05 M $CuSO_4$ and 0.05 M $CoCl_2$ at pH 1.5

The same procedure is repeated for the solution at a pH of 1.50. Figure 5.27 shows the voltammogram for $CoCl_2$ and $CuSO_4$, where three distinctive peaks are observed in the cathodic direction of the scan. The first peak is observed around 0.15 V, the second around -0.80 V and the last at -1.10 V. These peaks are related to the deposition of copper and cobalt, which will be confirmed by the EQCM later. It is expected that one of the peaks is characteristic for the hydrogen evolution reaction (HER), due to the acidic conditions. In the anodic direction of the scan, two peaks are visible. The first around 0.18 V, and the second around 0.40 V.

To obtain the reaction parameters, the cathodic peaks are plotted against the square root of the scan rate, shown in figure 5.28. A linear relationship is visible for the first five points, whereas the last does not fit perfectly in the trendline. This gives reaction parameters that are less reliable. Using this graph, the value for α is equal to 0.25, the diffusion coefficient is $6.61 \times 10^{-8}\,\mathrm{cm^2\,s^{-1}}$, and k_s is $5.60 \times 10^{-9}\,\mathrm{cm\,s^{-1}}$, which indicates the reaction is irreversible.

To distinguish reactions involving copper and cobalt, the M/z values are used to identify the reaction in the solution. Figures 5.29 and 5.30 show the voltammogram combined with Δm for respectively a pH level of 5.60 and 1.50. The curves show similarities, with both two peaks in the cathodic direction of the scan at 1.00 V and around -0.50 V. The peaks for the pH 1.50 are higher and at -1.10 V, the current for pH 1.50 is also more negative than for pH 5.60. The curves for Δm are also similar in shape. The maximum deposition is 16.3 μg for pH 5.60, which indicates a change in maximum mass per unit area of $83.2\,\mathrm{\mu g\,cm^{-2}}$. The maximum deposition is 23.3 μg for pH 1.50, which indicates a change in maximum mass per unit area of $118.7\,\mathrm{\mu g\,cm^{-2}}$. This means that for a pH of 1.50 the rate of deposition is higher and therefore more effective.

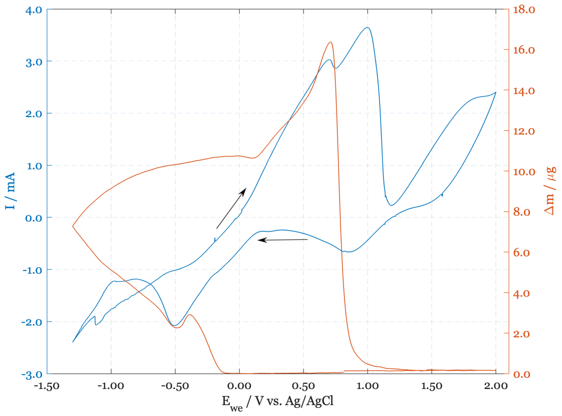

Figure 5.29: Cyclic voltammogram (—) for 0.05 M $CuSO_4$ and 0.05 M $CoCl_2$ at pH 5.60 and corresponding curve for Δf (—)

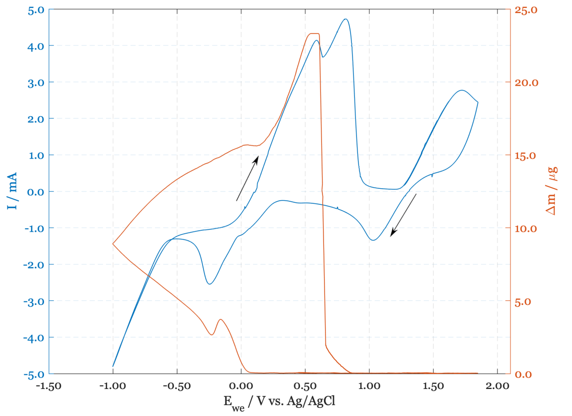

Figure 5.30: Cyclic voltammogram (—) for 0.05 M $CuSO_4$ and 0.05 M $CoCl_2$ at pH 1.50 and corresponding curve for Δm (—)

In the voltammograms, three distinctive peaks in the cathodic direction are visible around 0.50 V, -0.30 V and -1.10 V. Using EQCM, three measurements are carried out using chronoamperometry, which is the measurement of the current response to a constantly applied potential. A constant potential for these three points is applied for 60 seconds. For this type of experiment, it is expected the the values for M/z over time will become constant and will approach the characteristic values for the selected species known from the literature.

Table 5.3 shows the M/z values for the data obtained from figures 5.29 and 5.30. At a potential of 0.50 V, from 0 to 29 seconds, the M/z value stays around $20.0\,\mathrm{g\,mol^{-1}}$, after which, from 29 to 30 seconds, it increases to around $25.8\,\mathrm{g\,mol^{-1}}$. This approaches the characteristic M/z value for direct cobalt deposition, which is $29.5\,\mathrm{g\,mol^{-1}}$. At a potential of -0.30 V, from 0 to 4 and 12 to 60 seconds, the M/z value stays relative low, around 2.0 to $10.9\,\mathrm{g\,mol^{-1}}$, where between 4 to 12 seconds it increases up to $39.2\,\mathrm{g\,mol^{-1}}$. This approaches the characteristic M/z value for direct copper deposition, which is $31.8\,\mathrm{g\,mol^{-1}}$ or higher in mixed solutions. For the potential of -1.10 V, all values from 0 to 60 seconds stay relatively constant around $20.0\,\mathrm{g\,mol^{-1}}$. This seems to approach the characteristic M/z value for direct cobalt deposition. However only a small peak is visible in figure 5.29. This peak and value could correspond to direct cobalt deposition. That is, however, unlikely since the peak at 0.50 V is more distinct and therefore more reliable.

Only for the solution with pH 5.60 chronoamperometry is used for this research, because it gives a better impression of the M/z values during the complete process of CV creating the voltammogram, instead of a static potential, and comparing both techniques the obtained M/z values are similar.

Table 5.3: M/z for 0.05 M $CoCl_2$ and 0.05 M $CuSO_4$ solution at pH = 5.60 using chronoamperometry for constant potentials of 0.50 V, -0.30 V and -1.10 V

Potential (V)	Time range (s)			M/z ($g\,mol^{-1}$)
0.50	0	to	16	19.2 ± 0.5
	16	to	29	20.5 ± 0.5
	29	to	60	25.8 ± 0.5
−0.30	0	to	4	2.0 ± 0.5
	4	to	12	39.2 ± 0.5
	12	to	60	10.9 ± 0.5
−1.10	0	to	3	20.0 ± 0.5
	3	to	13	20.8 ± 0.5
	13	to	47	19.0 ± 0.5
	47	to	60	17.0 ± 0.5

Next, the complete evaluated potential range from -1.30 V to 1.50 V, the M/z values for pH 5.60 and 1.50 are shown respectively in tables 5.4 and 5.5, where no chronoamperometry (constant potential), but regular CV (varying potential) is used. For both tables, the most important values are those for the cathodic peaks in the voltammograms, where reduction reactions occur. At pH 5.60, this is between 1.10 V and 0.50 V, and around -0.50 V. Table 5.4 shows that for the first window, no significant reaction occurs, where in the second window an M/z value around 23.6 $g\,mol^{-1}$ is observed. This is a little below the characteristic value of direct cobalt deposition. It can, however, be assumed that this reaction takes place at that interval, because it can be assumed that the current efficiency is not 100%. No clear peak is observed for copper deposition, but for values above 30.0 $g\,mol^{-1}$, it can be assumed this reaction is occurring. This indicates that copper deposition is happening in the -0.13 V to -0.48 V interval.

At pH 1.50, conditions are acidic, but peaks are observed around 1.0 V, and between -0.10 V and -0.50 V. Table 5.5 shows that for the first window, no significant reaction occurs, where in the second window an M/z value around 20.3 $g\,mol^{-1}$ is observed. This is a little below the characteristic value of direct cobalt deposition. However, from -0.93 V to -0.68 V the M/z value is 10.6 $g\,mol^{-1}$. The M/z value for cobalt deposition with adsorbed hydrogen is 15.2 $g\,mol^{-1}$. Therefore, it is assumed that cobalt deposition with hydrogen adsorption is occurring around the interval, because it can be assumed that the current efficiency is not 100%. No clear peak is observed for copper deposition, but for values above 30.0 $g\,mol^{-1}$, it can be assumed this reaction is occurring, since this is associated with copper, mentioned in chapter 3. This indicates that copper deposition is happening in the -0.27 V to -0.21 V and -0.21 V to 0.10 V intervals.

Table 5.4: M/z for 0.05 M $CoCl_2$ and 0.05 M $CuSO_4$ solution at pH = 5.60

pH	Potential range (V)			M/z ($g\,mol^{-1}$)
5.60	0.80	to	−0.13	0.8 ± 0.5
	−0.13	to	−0.48	75.3 ± 0.5
	−0.48	to	−1.30	23.6 ± 0.5
	−1.30	to	−0.14	11.2 ± 0.5
	−0.14	to	0.55	24.2 ± 0.5
	0.55	to	0.72	39.4 ± 0.5
	0.72	to	1.03	27.9 ± 0.5
	1.03	to	2.00	0.6 ± 0.5
	2.00	to	0.80	0.6 ± 0.5

Table 5.5: M/z for 0.05 M $CoCl_2$ and 0.05 M $CuSO_4$ solution at pH = 1.50

pH	Potential range (V)			M/z ($g\,mol^{-1}$)
1.50	0.37	to	−0.12	47.3 ± 0.5
	−0.12	to	−0.93	20.3 ± 0.5
	−0.93	to	−0.68	10.6 ± 0.5
	−0.68	to	−0.27	24.4 ± 0.5
	−0.27	to	−0.21	64.6 ± 0.5
	−0.21	to	0.10	77.0 ± 0.5
	0.10	to	1.80	0.1 ± 0.5
	1.80	to	0.37	0.1 ± 0.5

In tables 5.4 and 5.5, more M/z values are shown that are not involved in the labelling reactions that involve copper or cobalt. This research focuses on the cathodic peaks, which indicate a chemical reaction involving the reduction of an element. Peaks and potential ranges with a positive value are related to the oxidation of the reactions. In theory, the values for M/z for corresponding reduction and oxidation peaks are similar, however in reality, in most of the cases this cannot be achieved due to external factor influences on the electrochemical behaviour of the reactions.

5.7. Synthetic samples

With the help of partners within the CoG^3-project, two synthetic samples made by Longborough University are evaluated. These are synthetic oxyhydroxide samples doped with 8.00 and 10.00 mol% of cobalt. The ideal formulae are $Fe_{0.92}Co_{0.08}OOH$ and $Fe_{0.90}Co_{0.10}OOH$. The synthesis of both samples is shown in table 5.6. Using these samples, the theoretical input can be calculated, whereafter the yield can be observed on the electrode using the EQCM and the amount of precipitate on the surface of the electrode.

Table 5.6: Overview of the synthesis of the synthetic samples

Sample No.	Synthesis:			Amount (g)
	Temperature	Aging time	Dopant level	
SD069	70 °C	11 days	10 mol$^{\%}$ Co	1.0007
SD073	70 °C	11 days	8 mol$^{\%}$ Co	1.0027

Using the ideal formulae, the amount of cobalt in the solutions can be calculated. The the subtotal molar mass of the samples SD069 and SD073 are respectively 89.16 and 89.10 $g\,mol^{-1}$. The subtotal mass percentage of cobalt in these samples is 6.61% for SD069 and 5.29% for SD073. For both leaching solutions 0.5 grams is used, which indicates that the amount of cobalt is 0.0330 g for SD069 and 0.0265 g for SD073. These amounts are valid for the samples before leaching, which also has a large influence on the electrochemical behaviour of the solution. After leaching it is not known what the recovery percentage will be, which makes the measurements less reliable in the end. In the following subsection, both samples are analysed using CV and EQCM, after which their M/z values will be evaluated to select the involved reactions within the solution.

5.7.1. SD069

Both samples are tested at pH levels of 5.60 and 1.10. The solution is leached using HNO_3 for 45 minutes, which causes an acidic condition of pH 1.10. Using a 3 M NaOH solution, the pH was increased to 5.60, which is above the threshold of pH 4.00, the level at which it is assumed the deposition of cobalt will occur with adsorbed hydrogen, which decreases the reaction efficiency. This section evaluates the synthetic samples containing 10 mol% cobalt. Figure 5.31 shows the voltammogram and corresponding Δm of the solution at pH 5.60. Two small peaks in the cathodic direction of the scan are observed around 0.20 V and -0.10 V, after which a drop in the current will set in around -0.50 V. The mass at the electrode increases after 0.40 V to a maximum of 1.53 µg, which indicates a change in mass per unit area of 7.81 $\mu g\,cm^{-2}$.

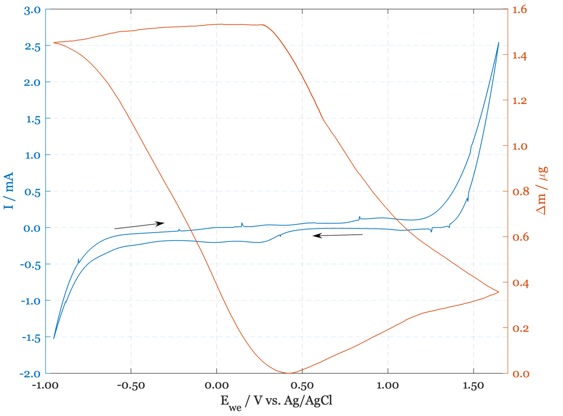

Figure 5.31: CV (—) for SD069 synthetic sample in 0.5 M HNO_3 at pH 5.60 and corresponding curve for Δm (—)

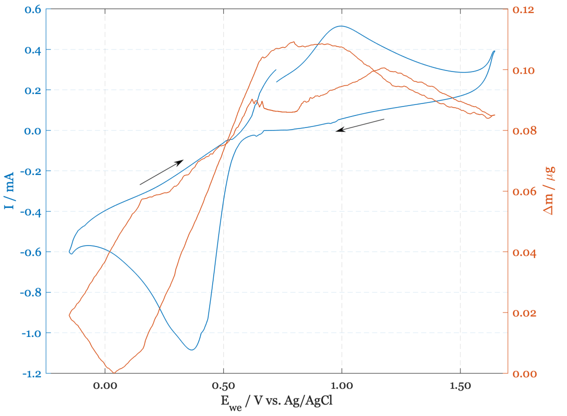

Figure 5.32: CV (—) for SD069 synthetic sample in 0.5 M HNO_3 at pH 1.10 and corresponding curve for Δm (—)

Figure 5.32 shows the voltammogram and corresponding Δm of the solution at pH 1.10. One large peak is observed between 0.50 V and 0.10 V, after which a small drop in the current will begin at -0.10 V. The mass at the electrode increases after 0.00 V to a maximum of 0.11 µg, which indicates a change in mass per unit area of 0.56 $\mu g\,cm^{-2}$. This indicates such a small mass increase that it can be assumed that no deposition has taken place at the surface of the electrode using a pH of 1.10.

Using the values for M/z, the reactions in the solution can be evaluated. Table 5.7 shows the M/z values for the solution at pH 5.60. Two small peaks are visible around 0.20 V and -0.10 V. Looking at the M/z values the second peak can be attributed to the direct deposition of cobalt with an M/z of 29.4 $g\,mol^{-1}$. This indicates the other peak is involved in the reduction of Fe^{3+} to Fe^{2+}, which has a characteristic M/z value of 55.8. Table 5.8 shows the M/z values for the solution at pH 1.10. One peak is visible in around 0.25 V, which looking at the M/z values cannot be attributed to the direct deposition of cobalt or the reduction of iron. The peak indicates an M/z value of 4.2 $g\,mol^{-1}$, which cannot be assigned to any specific reaction involving cobalt or iron.

Table 5.7: M/z for SD069 in 0.5 M HNO_3 solution at pH = 5.60

pH	Potential range (V)			M/z ($g\,mol^{-1}$)
5.60	0.58	to	1.27	71.4 ± 0.5
	1.27	to	1.65	2.2 ± 0.5
	1.65	to	1.24	1.2 ± 0.5
	1.24	to	0.36	92.4 ± 0.5
	0.36	to	0.18	48.9 ± 0.5
	0.18	to	−0.67	29.4 ± 0.5
	−0.67	to	0.58	1.9 ± 0.5

Table 5.8: M/z for SD069 in 0.5 M HNO_3 solution at pH = 1.10

pH	Potential range (V)			M/z ($g\,mol^{-1}$)
1.10	0.68	to	1.38	3.8 ± 0.5
	1.38	to	1.60	1.7 ± 0.5
	1.60	to	0.45	12.0 ± 0.5
	0.45	to	−0.20	4.2 ± 0.5
	−0.20	to	0.68	8.5 ± 0.5

Figures 5.33 and 5.32 show six and twelve consecutive cycles of the solutions at pH 5.60 and 1.10. At a pH of 5.60, the amount of deposited material increases with each cycle, where at pH 1.10 a minimal increase is observed which can be neglected. For pH 5.60, after twelve cycles 5.80 µg is deposited on the electrode surface of the EQCM, which indicates a change in mass per unit area of 29.6 $\mu g\,cm^{-2}$. This concludes that deposition is occurring at pH 5.60, where no reaction mechanisms are observed for pH 1.10.

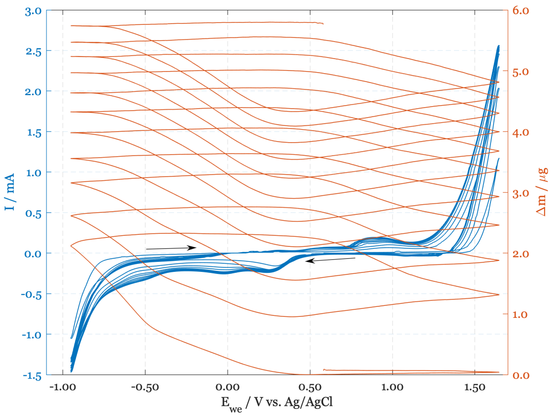

Figure 5.33: CV (—) for SD069 synthetic sample in 0.5 M HNO_3 at pH 5.60 and corresponding curve for Δm (—) after 12 cycles

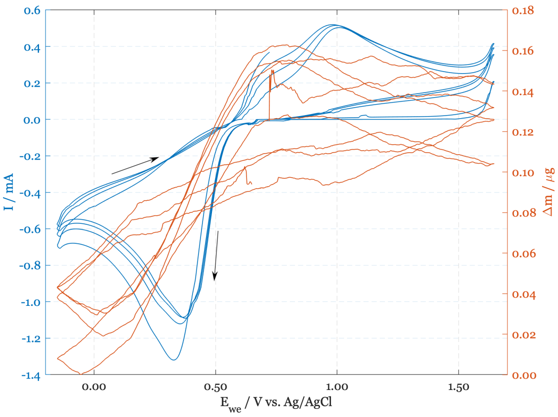

Figure 5.34: CV (—) for SD069 synthetic sample in 0.5 M HNO_3 at pH 1.10 and corresponding curve for Δm (—) after 6 cycles

5.7.2. SD073

This section evaluates the synthetic samples containing 8 mol% cobalt. Figure 5.35 shows the voltammogram and corresponding Δm of the solution at pH 5.60. In total, three peaks in the cathodic direction of the scan can be seen. The first small peak can be seen around 0.80 V, after which two larger peaks are observed around -0.30 V and -0.70 V. The mass at the electrode increases after 1.00 V to a maximum of 0.052 µg, which indicates a negligible change in mass per unit area of 0.27 $\mu g\,cm^{-2}$. Therefore, it can be assumed that no deposition has taken place at the surface of the electrode of the EQCM.

Figure 5.36 shows the voltammogram and corresponding Δm of the solution at pH 1.10. One large peak is observed between 0.45 V and 0.15 V, after which a small drop in the current begins at -0.10 V. The mass at the electrode increases after 0.10 V to a maximum of 0.13 µg, which indicates a change in mass per unit area of 0.66 $\mu g\,cm^{-2}$. This indicates such a small mass increase that it can be assumed that no deposition has taken place at the surface of the electrode at a pH of 1.10.

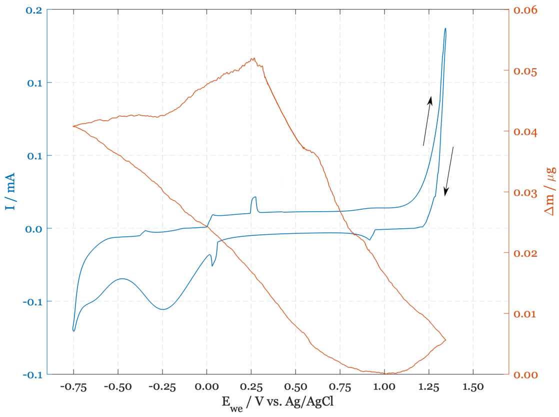

Figure 5.35: CV (—) for SD073 synthetic sample in 0.5 M HNO_3 at pH 5.60 and corresponding curve for Δm (—)

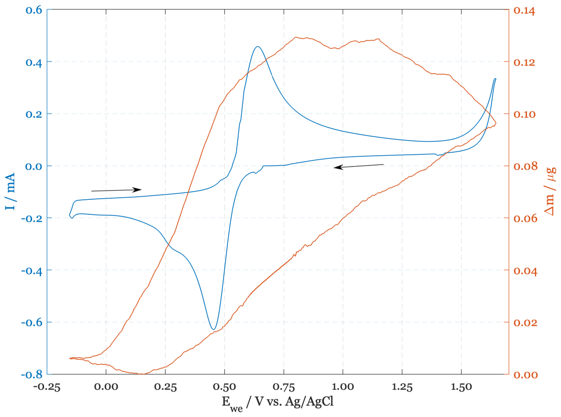

Figure 5.36: CV (—) for SD074 synthetic sample in 0.5 M HNO_3 at pH 1.10 and corresponding curve for Δm (—)

Using the values for M/z, the reactions in the solution can be evaluated. Table 5.9 shows the M/z values for the solution at pH 5.60. Three peaks are visible, around 0.75 V, -0.30 V and -0.70 V. Looking at the M/z values, the first peak can be attributed to the direct deposition of cobalt with an M/z of 30.6 $g\,mol^{-1}$. This indicates that the other peaks are involved in the reduction of Fe^{3+} to Fe^{2+}, which is not visible in the characteristic M/z values. Table 5.10 shows the M/z values for the solution at pH 1.10. One distinctive peak is visible around 0.40 V, which, looking at the M/z values, can be assigned to the direct deposition of cobalt with an M/z value of 28.8 $g\,mol^{-1}$, as the typical M/z value for cobalt deposition is 29.5 $g\,mol^{-1}$.

Table 5.9: M/z for SD073 in 0.5 M HNO_3 solution at pH = 5.60

pH	Potential range (V)			M/z ($g\,mol^{-1}$)
5.60	0.38	to	1.12	23.7 ± 0.5
	1.12	to	1.30	3.9 ± 0.5
	1.30	to	1.21	3.8 ± 0.5
	1.21	to	0.01	30.6 ± 0.5
	0.01	to	−0.43	3.4 ± 0.5
	−0.43	to	−0.80	5.1 ± 0.5
	−0.80	to	0.38	8.3 ± 0.5

Table 5.10: M/z for SD073 in 0.5 M HNO_3 solution at pH = 1.10

pH	Potential range (V)			M/z ($g\,mol^{-1}$)
1.10	0.65	to	1.60	22.2 ± 0.5
	1.60	to	0.55	45.4 ± 0.5
	0.55	to	0.17	28.8 ± 0.5
	0.17	to	−0.20	2.5 ± 0.5
	−0.20	to	0.65	5.1 ± 0.5

Figures 5.37 and 5.38 show 12 consecutive cycles of the solutions at pH 5.60 and 1.10. For both pH values, the amount of deposited material at the electrode is minimal, which indicates that no increase is observed. For pH 5.60, after 12 cycles 0.12 µg is deposited on the electrode surface of the EQCM, which indicates a change in mass per unit area of 0.61 $\mu g\,cm^{-2}$. This is a significantly small amount that can therefore be neglected. For pH 1.10, after 12 cycles 0.25 µg is deposited on the electrode surface of the EQCM, which indicates a change in mass per unit area of 2.19 $\mu g\,cm^{-2}$, which can also be neglected. This indicates that mass increase does not occur at both pH 5.60 and 1.10.

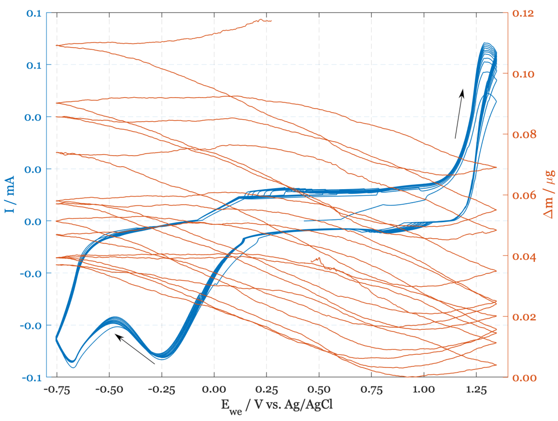

Figure 5.37: CV (—) for SD073 synthetic sample in 0.5 M HNO_3 at pH 5.60 and corresponding curve for Δm (—) after 12 cycles

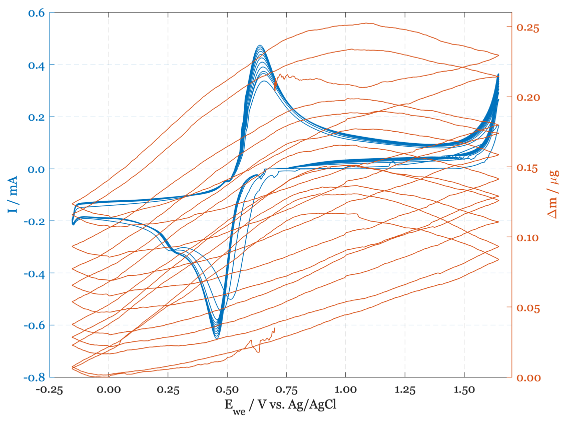

Figure 5.38: CV (—) for SD073 synthetic sample in 0.5 M HNO_3 at pH 1.10 and corresponding curve for Δm (—) after 12 cycles

5.8. Mutanda samples

In this section, samples of cobalt bearing material are analysed using both CV and EQCM techniques in order to determine if the electrochemical responses of different quantities of cobalt bearing minerals have an influence on the shape of the voltammograms and changes in the Δm. The used samples originate from the DRC within the Mutanda mining operation, which was evaluated in chapter 3. From different samples within the structures of the Mutanda region, six samples are selected based on their grades of carrollite and heterogenite. These minerals, especially carrolite, are cobalt bearing minerals which make the ores suitable for cobalt mining. Figure 5.39 shows small sample bags used in these experiments with their Mutanda mining code (MMxxxx) and lab code (18GL3x) used within the laboratory's of Camborne School of Mines.

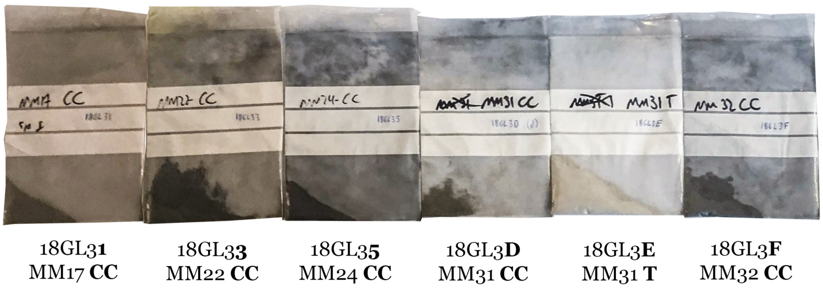

Figure 5.39: Overview of the used samples for the experiments in this section

The samples are selected from a range of 11 samples used by Tijsseling (2017) in an MSc-thesis carried out within the same CoG^3-project. In that research, Quantitative Evaluation of Minerals by Scanning Electron Microscopy (QEMSCAN) was used in order to select the tested samples. QEMSCAN is a method to quantitatively analyse ore and to provide reliable mineralogical and mineral analysis (Gottlieb et al., 2000). It is considered to be an automated image analysis tool, but provides much more information, such as quantitative chemical, mineralogical and textural data, accompanied by compositional maps on micron-scale (Goodall et al., 2005).

The samples of figure 5.39 were selected based on QEMSCAN analyses focusing on the mineral mass percentage. First, the samples with the highest and lowest percentage of carrollite were selected, after which four other samples were gradually selected between the minimum and maximum. Chalcopyrite and bornite are other abundant minerals which can be of influence, so different grades for these minerals were also selected. Of all minerals that are characterised using QEMSCAM, only carrollite and heterogenite contain cobalt. However, the mineral mass percentages of heterogenite varied between trace minerals and 0.01%. This indicates that this mineral will have minor influence on the electrochemical behaviour of cobalt.

Table 5.11 shows an overview of the mineral mass (%) of the samples. Looking at carrollite, sample 18GL3F has the highest mineral mass of 64.09%, where sample 18GL3E contains the lowest percentage with 0.65%. In between, four samples with grades of 46.74% (18GL31), 36.24% (18GL33), 29.51% (18GL35) and 24.39% (18GL3D) were selected. The grades of heterogenite are small and can therefore be neglected. On the other hand, 18GL33 and 18GL35 contain high fractions of bornite, which contains iron and can therefore show the same electrochemical behaviour as the synthetic samples in section 5.7. As mentioned in table 3.1 the overall cobalt and copper grade per sample is circa 1.38% and 3.74%, fluctuating with the carrollite mass percentage.

Table 5.11: Overview of mineral mass (%) of the analysed samples from the Mutanda mining operation

Mineral	CSM Lab Code					
	18GL3F	18GL31	18GL33	18GL35	18GL3D	18GL3E
Carrollite	64.09	46.74	36.24	29.51	24.39	0.65
Heterogenite	0.01	0.00	0.00	0.00	0.00	0.00
Chalcopyrite	3.55	16.13	1.09	1.22	28.95	1.53
Bornite	15.51	0.16	49.32	53.37	0.33	0.01
Pyrite	0.06	4.21	0.04	0.18	0.07	0.01
Dolomite	5.05	0.19	2.24	5.17	2.14	14.22
Fe Dolomite / Ankerite	0.08	0.03	0.08	0.05	0.09	0.40
Quartz	6.15	16.91	3.68	7.12	17.42	25.00
K-feldspar	0.17	9.48	0.01	0.01	10.17	23.82
Muscovite / Illite	0.02	2.67	0.00	0.01	3.48	4.32
Chalcocite	0.28	0.05	2.20	1.47	0.02	0.00
Phlogopite	0.05	0.08	0.00	0.00	5.80	15.10
Magnesiochlorite	1.99	0.28	3.95	0.80	4.12	10.57
Mg silicates	2.13	0.02	0.20	0.14	0.04	0.09
Others	0.87	3.05	0.96	0.95	2.99	4.27

Figure 5.40 shows a graphical interpretation of the data from table 5.11. Here, from the left to right, a clear decrease in carrolite grade is visible for the selected samples. Also the higher grades of bornite for 18GL31 and 18GL33 are visible. Sample 18GL3E shows a wider variety of minerals that are more equally distributed, with relatively even grades of dolomite, quartz, k-feldspar, phlogopite and magnesiochlorite. Because this sample contains almost no carrolite, the electrochemical behaviour is expected to be different.

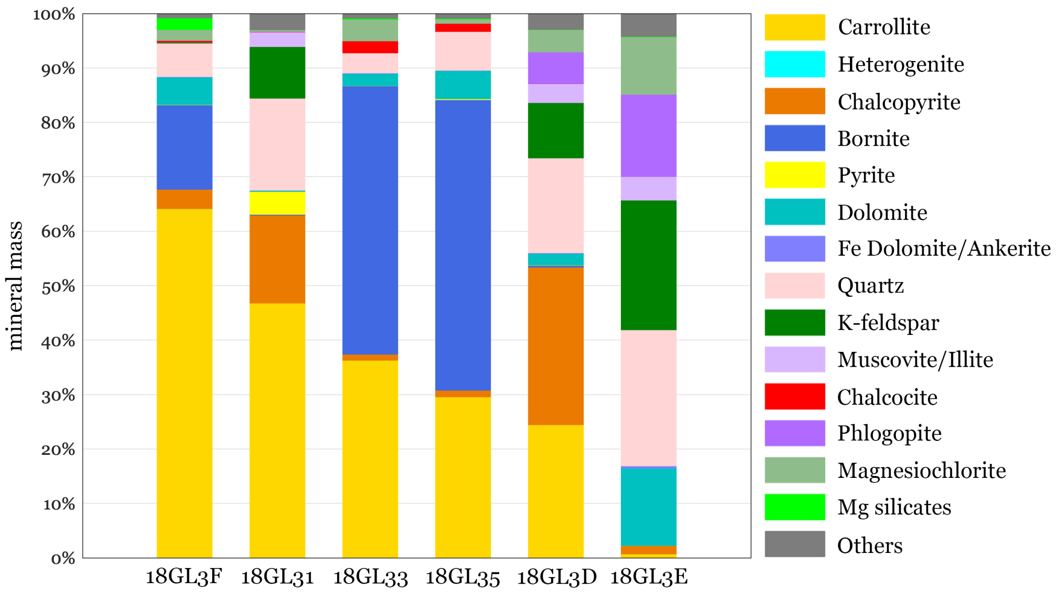

Figure 5.40: Mineral mass for the six chosen samples from the Mutanda mining operation with an increasing grade of cobalt-bearing Carrolite and Heterogenite

In the following sections, all samples will be evaluated using cyclic voltammetry and EQCM to obtain the reaction parameters, whereafter the M/z values are evaluated to discover the reactions taking place inside the electrolyte solution. This is done from the highest to the lowest carrollite mass percentage.

5.8.1. 18GL3F

In this section, the voltammograms, Δm-curve and M/z values of sample 18GL3F are evaluated, after which the cathodic and anodic peak potentials are discussed and the kinetic reaction parameters are calculated. The minerals in this sample with the largest mineral mass are carrollite (64.09%) and bornite (15.51%). The other minerals have a contribution lower then 10.00% to the total mineral mass. The voltammogram of this sample is shown in figure 5.41. Here, a large drop is visible in the cathodic direction of the scan between -0.15 V and -0.80 V. Two peaks are visible in the anodic direction of the scan around 0.15 V and 1.20 V. Table 5.12 shown the peaks of visible in the voltammogram with the corresponding applied voltage.

Table 5.12: Peak characteristics for the 18GL3F sample

Peak	Current density peak (mA)	Applied voltage (V)
Cathodic	−26.53	−0.80
Anodic (1^{st})	3.80	0.21
Anodic (2^{nd})	1.01	0.98

Using the cathodic peaks of the scan rates from 40 to 120 mV/s shown in figure 5.41, the current densities of the peaks are plotted against the square root of the scan rate in figure 5.42. Here, an acceptable linear relationship is visible. Using this graph, the reaction parameters for cobalt deposition are estimated, where α is estimated to be equal to 0.37, the diffusion coefficient is $5.73 \times 10^{-6}\,\mathrm{cm^2\,s^{-1}}$, and k_s is $3.24 \times 10^{-2}\,\mathrm{cm\,s^{-1}}$, which indicates the reaction is quasi-reversible.

Using the EQCM, a voltammogram together with a mass change curve is generated, shown in figure 5.43. Here a similar voltammogram as in figure 5.41 is visible. From the figure, it can be seen the a mass increase starts from circa 0.25 V in the cathodic direction of the scan, which keeps increasing up to around -0.10 V in the anodic direction of the scan. In this window a maximum mass of 2.93 µg is deposited at the surface of the electrode. This indicates a maximum change in mass per unit area of $14.9\,\mathrm{\mu g\,cm^{-2}}$.

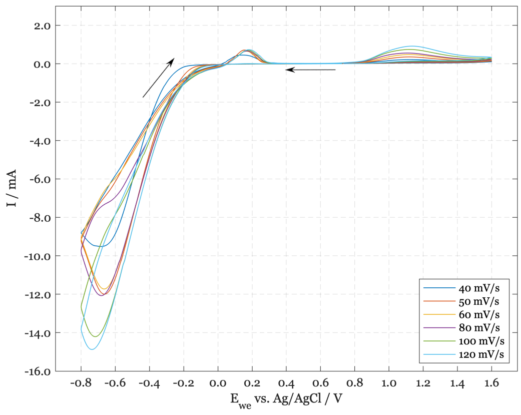

Figure 5.41: Voltammogram for 0.75 g 18GL3F in 0.5 M HNO_3 for scan rates between 40 and 120 mV/s at 298 K at pH 1.1

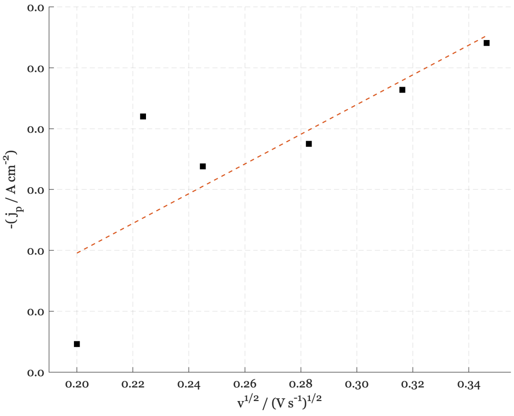

Figure 5.42: Cathodic peak current densities of CV curve for 0.75 g 18GL3F in 0.5 M HNO_3 at pH 1.1

Using the graph of Δf versus ΔQ obtained using the EQCM method, the M/z values are calculated and compared with the voltammogram and the characteristic values for M/z according to the literature. Table 5.13 shows the M/z values for the graphs visible in figure 5.43. Two windows with a distinctive M/z value can be observed, from 0.72 V to -0.29 V and from -0.11 V to 0.23 V. For the other potential ranges, an M/z value lower than four is observed, which indicates no active reactions are occurring at that potential range. For 0.72 V to -0.29 V, the deposition of cobalt with adsorbed hydrogen is active, with an observed M/z value of 11.3 $\mathrm{g\,mol^{-1}}$, which is close to the characteristic value of 14.80 $\mathrm{g\,mol^{-1}}$. For -0.11 V to 0.23 V, the direct reduction of copper is active, having a observed M/z value of 34.2 $\mathrm{g\,mol^{-1}}$, where during copper dissolution the M/z value has a characteristic value close to 31.8 $\mathrm{g\,mol^{-1}}$ or higher. This concludes that both copper and cobalt are electrochemically active.

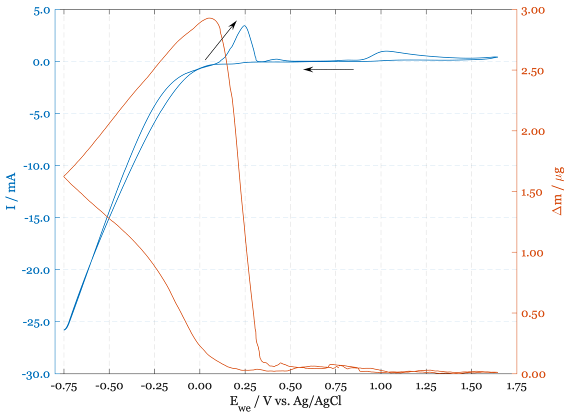

Figure 5.43: Cyclic voltammogram (—) for 18GL3F sample in 0.5 M HNO_3 at pH 1.10 and corresponding curve for Δm (—)

Table 5.13: M/z for 18GL3F sample in 0.5 M HNO_3 solution at pH = 1.10

pH	Potential range (V)			M/z ($g mol^{-1}$)
1.20	0.72	to	−0.29	11.3 ± 0.5
	−0.29	to	−0.80	0.4 ± 0.5
	−0.80	to	−0.48	0.1 ± 0.5
	−0.48	to	−0.11	2.0 ± 0.5
	−0.11	to	0.23	34.2 ± 0.5
	0.23	to	1.60	0.0 ± 0.5
	1.60	to	0.72	1.5 ± 0.5

5.8.2. 18GL31

In this section, the voltammograms, Δm-curve and M/z values of sample 18GL31 are evaluated, after which the cathodic and anodic peak potentials are discussed, and the kinetic reaction parameters are calculated. The minerals in this sample with the largest mineral mass are carrollite (46.74%), chalcopyrite (16.14%) and quartz (16.91%). The other minerals have a contribution lower then 10% to the total mineral mass. The voltammogram of this sample is shown in figure 5.44. Here, one large drop is visible in the cathodic direction of the scan between -0.4 V and -0.8 V, and two smaller peaks are visible in the anodic direction of the scan around 0.10 V and 1.10 V. Table 5.14 shows the peaks visible in the voltammogram with the corresponding applied voltage. For the cathodic peak, no clear peak wave is visible, so the minimum current is indicated as the current density peak.

Table 5.14: Peak characteristics for the 18GL31 sample for ν = 100 mV/s

Peak	Current density peak (mA)	Applied voltage (V)
Cathodic	−16.69	−0.80
Anodic (1^{st})	0.48	0.16
Anodic (2^{nd})	1.09	0.71

Using the cathodic peaks of the scan rates from 40 to 120 mV/s shown in figure 5.44, the current densities of the peaks are plotted against the square root of the scan rate in figure 5.45. Here, a linear relationship is visible for the first and last four points. The second point of the measurements is not in line with the plotted trendline. Using this graph, the value for α is estimated to be equal to 0.49, the diffusion coefficient is 1.04×10^{-10} $cm^2 s^{-1}$, and k_s is 4.27×10^{-5} $cm s^{-1}$, which indicates the reaction is quasi-reversible.

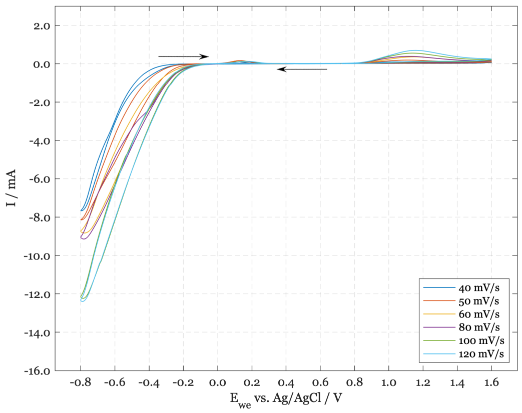

Figure 5.44: Voltammogram for 0.75 g 18GL31 in 0.5 M HNO_3 for scan rates between 40 and 120 mV/s at 298 K at pH 1.1

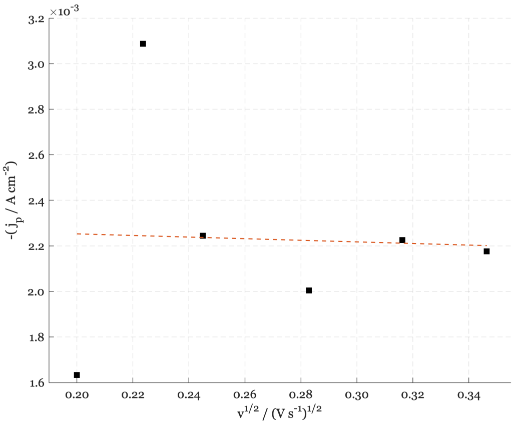

Figure 5.45: Anodic peak current densities of CV curve for 0.75 g 18GL31 in 0.5 M HNO_3 at pH 1.1

Using the EQCM, a voltammogram together with a mass change curve is generated, shown in figure 5.46. Here a similar voltammogram as in figure 5.44 is shown. From the figure, it can be seen that Δm starts from circa 1.10 V in the cathodic direction of the scan, which keeps increasing up to around -0.20 V in the anodic direction of the scan. In this window a maximum mass of 0.54 µg is deposited at the surface of the electrode of the EQCM. This indicates a maximum change in mass per unit area of 2.75 $\mu g\,cm^{-2}$.

Using the graph of Δf versus ΔQ obtained using the EQCM method, the M/z values are calculated and compared with the voltammogram and the characteristic values for M/z according to the literature. Table 5.15 shows the M/z values for the graphs visible in figure 5.46. Two windows with a clear M/z value can be observed, from 0.67 V to -0.22 V and from -0.15 V to 0.75 V. For the other windows an M/z value close to zero is observed, which indicates no active reactions are happening in that potential range. For 0.67 V to -0.22 V, the deposition of cobalt with adsorbed hydrogen is active, with an observed M/z value of 16.0 $g\,mol^{-1}$, which is close to the characteristic value of 15.2 $g\,mol^{-1}$. For -0.15 V to -0.75 V, the deposition of copper is active, with an observed M/z value of 68.7 $g\,mol^{-1}$, where during copper deposition M/z can increase up to values close to 80 $g\,mol^{-1}$. This concludes that both copper and cobalt are active at potentials between 0.35 V and -0.70 V.

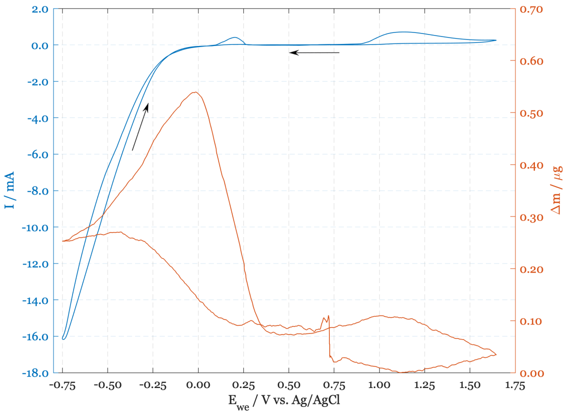

Figure 5.46: Cyclic voltammogram (—) for 18GL31 sample in 0.5 M HNO_3 at pH 1.20 and corresponding curve for Δm (—)

Table 5.15: M/z for 18GL31 sample in 0.5 M HNO_3 solution at pH = 1.10

pH	Potential range (V)			M/z ($g\,mol^{-1}$)
1.20	0.67	to	−0.22	16.0 ± 0.5
	−0.22	to	−0.80	0.1 ± 0.5
	−0.80	to	−0.55	0.4 ± 0.5
	−0.55	to	−0.15	0.9 ± 0.5
	−0.15	to	0.75	68.7 ± 0.5
	0.75	to	1.60	0.2 ± 0.5
	1.60	to	0.67	0.1 ± 0.5

5.8.3. 18GL33

In this section, the voltammograms, Δm-curve and M/z values of sample 18GL33 are evaluated, after which the cathodic and anodic peak potentials are discussed, and the kinetic reaction parameters are calculated. The minerals in this sample with the largest mineral mass are carrollite (36.24%) and bornite (49.32%). The other minerals have a contribution lower then 10% to the total mineral mass. The voltammogram of this sample is shown in figure 5.47. Here, one large drop is visible in the cathodic direction of the scan between -0.30 V and -0.80 V, and two peaks are visible in the anodic direction of the scan around 0.20 V and 1.15 V. Table 5.16 shows the peaks visible in the voltammogram with the corresponding applied voltage.

Table 5.16: Peak characteristics for the 18GL33 sample

Peak	Current density peak (mA)	Applied voltage (V)
Cathodic	−28.09	−0.80
Anodic (1^{st})	7.33	0.29
Anodic (2^{nd})	0.42	1.09

Using the cathodic peaks of the scan rates from 40 to 120 mV/s shown in figure 5.47, the current densities of the peaks are plotted against the square root of the scan rate in figure 5.48. Here, an acceptable linear relationship is visible. Using this graph, the reaction parameters for cobalt deposition are estimated. α is estimated to be equal to 0.77, the diffusion coefficient is $1.85 \times 10^{-6}\,cm^2\,s^{-1}$, and k_s is $2.74 \times 10^{-8}\,cm\,s^{-1}$, which indicates the reaction is irreversible.

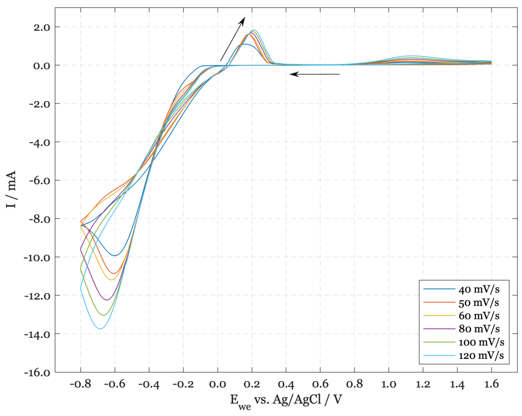

Figure 5.47: Voltammogram for 0.75 g 18GL33 in 0.5 M HNO_3 for scan rates between 40 and 120 mV/s at 298 K at pH 1.1

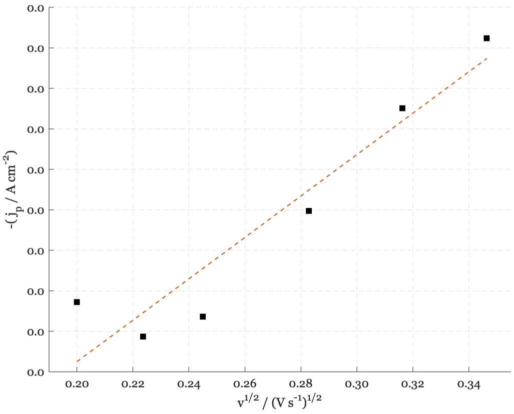

Figure 5.48: Cathodic peak current densities of CV curve for 0.75 g 18GL33 in 0.5 M HNO_3 at pH 1.1

Using the EQCM, a voltammogram together with a mass change curve is generated, shown in figure 5.49. Here a similar voltammogram compared to figure 5.47 is visible. From the figure, it can be seen that a mass increase starts from circa 0.25 V in the cathodic direction of the scan, which keeps increasing up to around -0.10 V in the anodic direction of the scan. In this window a maximum mass of 7.46 µg is deposited at the surface of the resonator, which indicates a maximum change in mass per unit area of 38.0 $\mu g\,cm^{-2}$.

Using the graph of Δf versus ΔQ obtained using the EQCM method, the M/z values are calculated and compared with the voltammogram and the characteristic values for M/z according to the literature. Table 5.17 shows the M/z values for the graphs visible in figure 5.49. Two windows with a distinctive M/z value can be observed, from 0.67 V to -0.27 V and from 0.08 V to 0.34 V. For the other windows an M/z value lower than five is observed, which indicates no active reactions are occurring at that potential range. For 0.67 V to -0.27 V, the deposition of cobalt with adsorbed hydrogen is active, with an observed M/z value of 16.0 $g\,mol^{-1}$, which is close to the characteristic value of 15.2 $g\,mol^{-1}$. For 0.08 V to 0.34 V, the dissolution of cobalt is active, having an observed M/z value of 30.3 $g\,mol^{-1}$, where during cobalt dissolution the M/z value is close to 29.5 $g\,mol^{-1}$ according to the literature. This concludes that only cobalt is active at the potential around 0.25 V.

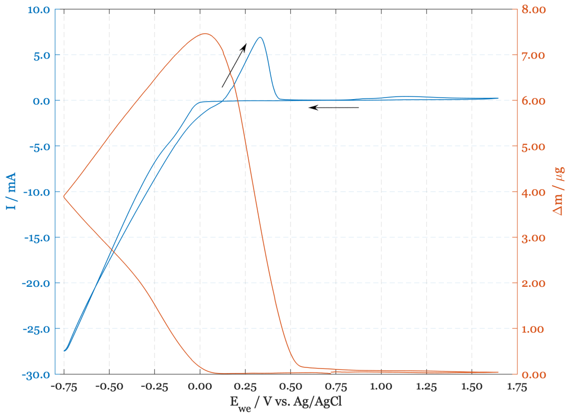

Figure 5.49: Cyclic voltammogram (—) for 18GL33 sample in 0.5 M HNO_3 at pH 1.10 and corresponding curve for Δm (—)

Table 5.17: M/z for 18GL33 sample in 0.5 M HNO_3 solution at pH = 1.10

pH	Potential range (V)			M/z ($g\,mol^{-1}$)
1.20	0.67	to	−0.27	11.1 ± 0.5
	−0.27	to	−0.42	2.9 ± 0.5
	−0.42	to	−0.80	1.0 ± 0.5
	−0.80	to	−0.31	1.4 ± 0.5
	−0.31	to	0.08	3.9 ± 0.5
	0.08	to	0.34	30.3 ± 0.5
	0.34	to	1.60	1.1 ± 0.5
	1.60	to	0.67	1.0 ± 0.5

5.8.4. 18GL35

In this section, the voltammograms, Δm-curve and M/z values of sample 18GL35 are evaluated, after which the cathodic and anodic peak potentials are discussed and the kinetic reaction parameters are calculated. The minerals in this sample with the largest mineral mass are carrollite (29.51%) and bornite (53.37%). The other minerals have a contribution lower then 10.00% to the total mineral mass. The voltammogram of this sample is shown in figure 5.50. Here, one small peak is observed around -0.20 V and a large drop is visible in the cathodic direction of the scan between -0.40 V and -0.80 V. Two peaks are visible in the anodic direction of the scan around 0.20 V and 1.15 V. Table 5.18 shows the peaks visible in the voltammogram with the corresponding applied voltage.

Table 5.18: Peak characteristics for the 18GL35 sample

Peak	Current density peak (mA)	Applied voltage (V)
Cathodic	−27.58	−0.80
Anodic (1st)	7.77	0.31
Anodic (2nd)	0.82	1.03

Using the cathodic peaks of the scan rates from 40 to 120 mV/s shown in figure 5.50, the current densities of the peaks are plotted against the square root of the scan rate in figure 5.51. Here, an acceptable linear relationship is visible. Using this graph, the reaction parameters for cobalt deposition are estimated. α is estimated to be equal to 0.21, the diffusion coefficient is $2.61 \times 10^{-6}\,\mathrm{cm^2\,s^{-1}}$, and k_s is $1.03 \times 10^{-7}\,\mathrm{cm\,s^{-1}}$, which indicates the reaction is irreversible.

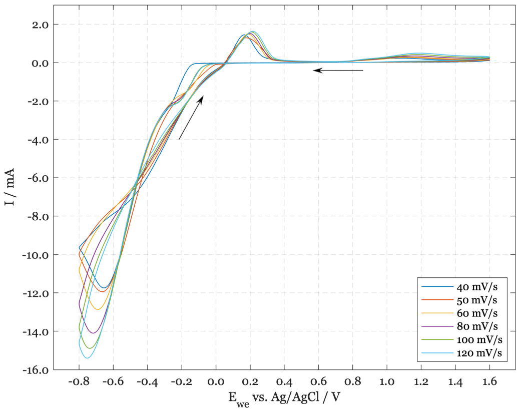

Figure 5.50: Voltammogram for 0.75 g 18GL35 in 0.5 M HNO_3 for scan rates between 40 and 120 mV/s at 298 K at pH 1.1

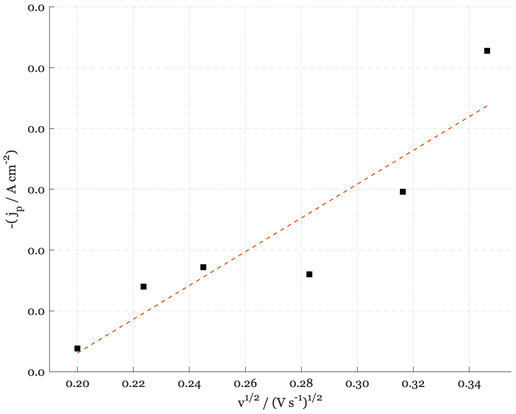

Figure 5.51: Cathodic peak current densities of CV curve for 0.75 g 18GL35 in 0.5 M HNO_3 at pH 1.1

Using the EQCM, a voltammogram together with a mass change curve is generated, shown in figure 5.52. Here a similar voltammogram as in figure 5.50 is visible. From the figure, it can be seen that a mass increase starts from circa 0.25 V in the cathodic direction of the scan, which keeps increasing up to around -0.10 V in the anodic direction of the scan. In this window a maximum mass of 7.74 µg is deposited at the surface of the electrode. This indicates a maximum change in mass per unit area of $39.42\,\mathrm{\mu g\,cm^{-2}}$.

Using the graph of Δf versus ΔQ obtained using the EQCM method, the M/z values are calculated and compared with the voltammogram and the characteristic values for M/z according to the literature. Table 5.19 shows the M/z values for the graphs visible in figure 5.52. Two windows with a distinctive M/z value can be observed, from 0.56 V to -0.27 V and from 0.01 V to 0.36 V. For the other windows an M/z value lower than four is observed, which indicates no active reactions are occurring in that potential range. For 0.56 V to -0.27 V, the deposition of cobalt with adsorbed hydrogen is active, with an observed M/z value of $13.10\,\mathrm{g\,mol^{-1}}$, which is close to the characteristic value of $14.80\,\mathrm{g\,mol^{-1}}$. From 0.01 V to 0.36 V, the direct dissolution of cobalt is active, with an observed M/z value of $28.8\,\mathrm{g\,mol^{-1}}$, where during cobalt dissolution the M/z value is close to $29.5\,\mathrm{g\,mol^{-1}}$. This concludes that only cobalt is active at the potential between -0.50 V and 0.25 V.

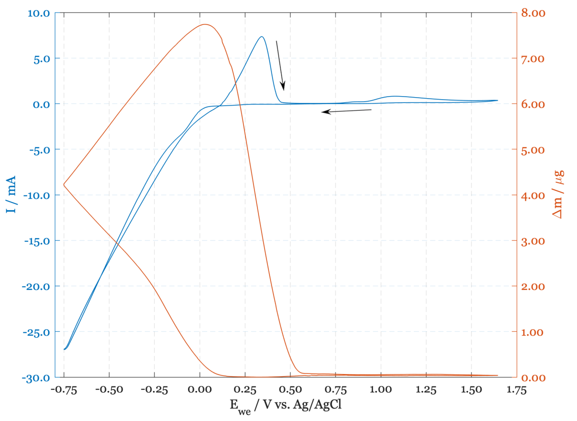

Figure 5.52: Cyclic voltammogram (—) for 18GL35 sample in 0.5 M HNO_3 at pH 1.10 and corresponding curve for Δm (—)

Table 5.19: M/z for 18GL35 sample in 0.5 M HNO_3 solution at pH = 1.10

pH	Potential range (V)			M/z (gmol^{-1})
1.20	0.56	to	−0.27	13.1 ± 0.5
	−0.27	to	−0.80	0.9 ± 0.5
	−0.80	to	−0.47	1.2 ± 0.5
	−0.47	to	0.01	3.7 ± 0.5
	0.01	to	0.36	28.8 ± 0.5
	0.36	to	1.60	0.2 ± 0.5
	1.60	to	0.56	0.1 ± 0.5

5.8.5. 18GL3D

In this section, the voltammograms, Δm-curve and M/z values of sample 18GL3D are evaluated, after which the cathodic and anodic peak potentials are discussed and the kinetic reaction parameters are calculated. The minerals in this sample with the largest mineral mass are carrollite (24.39%), chalcopyrite (28.95%), quartz (17.42%) and k-feldspar (10.17%). The other minerals have a contribution lower then 10.00% to the total mineral mass. The voltammogram of this sample is shown in figure 5.53. Here, a large drop is visible in the cathodic direction of the scan between -0.20 V and -0.80 V. Two peaks are visible in the anodic direction of the scan around 0.10 V and 1.05 V. Table 5.20 shows the peaks visible in the voltammogram with the corresponding applied voltage.

Table 5.20: Peak characteristics for the 18GL3D sample

Peak	Current density peak (mA)	Applied voltage (V)
Cathodic	−23.60	−0.80
Anodic (1st)	0.97	0.17
Anodic (2nd)	0.54	1.06

Using the cathodic peaks shown in figure 5.53, the current densities of the peaks are plotted against the square root of the scan rate in figure 5.54. A different phenomena is visible compared to similar figures for the other samples. Here, a linear relationship with a negative slope is observed. However, this can still be used and the reaction parameters for cobalt deposition are estimated, where α is calculated to be equal to 0.37, the diffusion coefficient is 1.92×10^{-7} cm^2 s^{-1}, and k$_s$ is 1.37×10^{-2} cm s^{-1}, indicating the reaction is quasi-reversible.

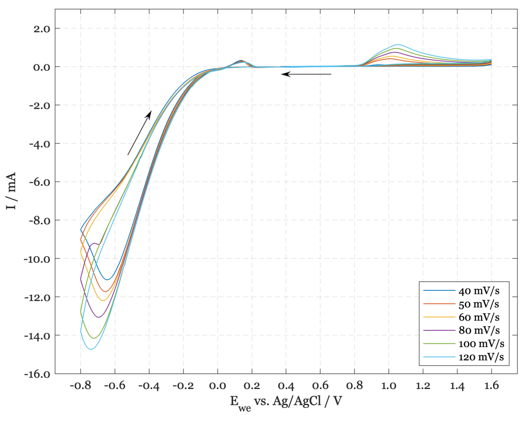

Figure 5.53: Voltammogram for 0.75 g 18GL3D in 0.5 M HNO_3 for scan rates between 40 and 120 mV/s at 298 K at pH 1.1

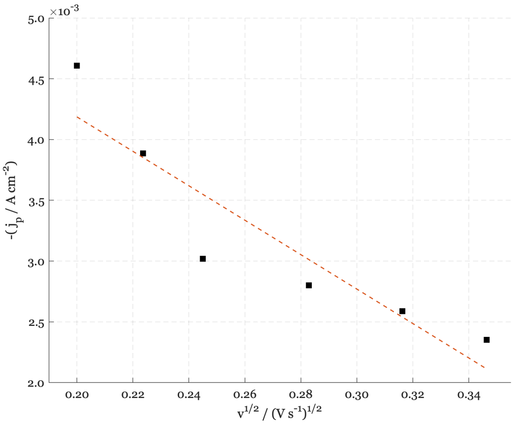

Figure 5.54: Cathodic peak current densities of CV curve for 0.75 g 18GL3D in 0.5 M HNO_3 at pH 1.1

Using the EQCM, a voltammogram together with a mass change curve is generated, shown in figure 5.55. Here a similar voltammogram as in figure 5.53 is visible. From the figure, it can be seen the a mass increase starts from circa 0.50 V in the cathodic direction of the scan, which keeps increasing up to around 0.00 V in the anodic direction of the scan. In this window a maximum mass of 0.88 µg is deposited at the surface of the electrode, which indicates a maximum change in mass per unit area of 4.49 $\mu g\,cm^{-2}$.

Using the graph of Δf versus ΔQ obtained using the EQCM method, the M/z values are calculated and compared with the voltammogram and the characteristic values for M/z according to the literature. Table 5.21 shows the M/z values for the graphs visible in figure 5.55. Two windows with a distinctive M/z value can be observed, from 1.60 V to -0.27 V and from -0.09 V to 0.56 V. For the other windows an M/z value around one is observed, which indicates no active reactions are occurring in that potential range. For 1.60 V to -0.27 V, the deposition of cobalt with adsorbed hydrogen is supposed to be active, having a characteristic M/z value of 14.80 $g\,mol^{-1}$, which is not close to the literature value of 7.20 $g\,mol^{-1}$. The value is almost half the characteristic value, which indicates the data for this interval is not completely reliable. For -0.09 V to 0.56 V, the direct dissolution of copper is active, having an observed M/z value of 42.5 $g\,mol^{-1}$, where during copper dissolution the M/z value can go up to 80 $g\,mol^{-1}$. This concludes that, due to the low M/z value in the first window, only copper is active at the potential around 0.25 V.

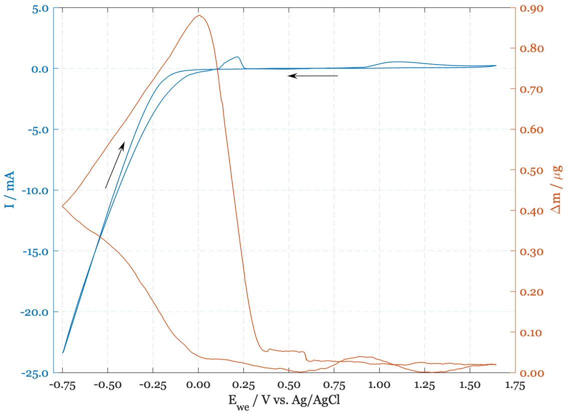

Figure 5.55: Cyclic voltammogram (—) for 18GL3D sample in 0.5 M HNO_3 at pH 1.10 and corresponding curve for Δm (—)

Table 5.21: M/z for 18GL3D sample in 0.5 M HNO_3 solution at pH = 1.10

pH	Potential range (V)			M/z ($g\,mol^{-1}$)
1.20	0.56	to	1.60	0.1 ± 0.5
	1.60	to	−0.27	7.2 ± 0.5
	−0.27	to	−0.52	0.7 ± 0.5
	−0.52	to	−0.80	0.1 ± 0.5
	−0.80	to	−0.49	0.2 ± 0.5
	−0.49	to	−0.09	1.1 ± 0.5
	−0.09	to	0.56	42.5 ± 0.5

5.8.6. 18GL3E

In this section, the voltammograms, Δm-curve and M/z values of sample 18GL3E are evaluated. The minerals in this sample with the largest mineral mass are dolomite (14.22%), quartz (25.00%), k-feldspar (23.82%), phlogopite (15.10%) and magnesiochlorite (10.57%). The other minerals have a contribution lower then 10.00% to the total mineral mass. The voltammogram of this sample is shown in figure 5.56. Here, a large drop is visible in the cathodic direction of the scan between -0.20 V and -0.80 V. One peak is visible in the anodic direction of the scan around 1.15 V. Table 5.22 shows the peaks visible in the voltammogram with the corresponding applied voltage.

Table 5.22: Peak characteristics for the 18GL3E sample

Peak	Current density peak (mA)	Applied voltage (V)
Cathodic	−15.74	−0.80
Anodic (1^{st})	0.14	0.44
Anodic (2^{nd})	0.65	1.09

As with the other samples, the cathodic peaks of the scan rate from 40 to 120 mV/s shown in figure 5.53 would be used for calculating the reaction parameters. However, no anodic or cathodic peak can be associated with copper or cobalt deposition and dissolution, which is evaluated using the EQCM. Therefore, it is not possible to generate a graph of the scan rate versus the current density and no reaction parameters can be obtained.

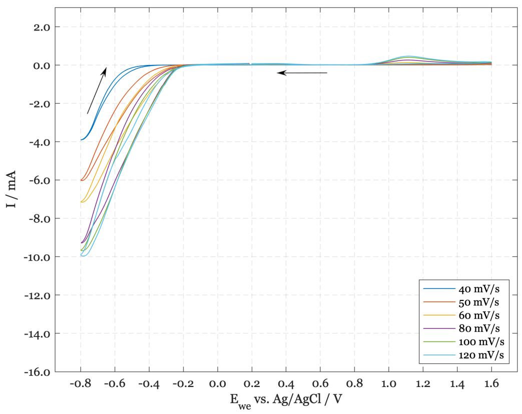

Figure 5.56: Voltammogram for 0.75 g 18GL3E in 0.5 M HNO_3 for scan rates between 40 and 120 mV/s at 298 K at pH 1.1

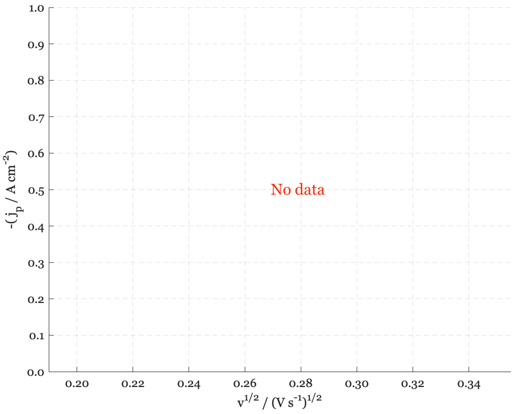

Figure 5.57: Cathodic peak current densities of CV curve for 0.75 g 18GL3E in 0.5 M HNO_3 at pH 1.1

Using the EQCM, a voltammogram together with a mass change curve is generated, shown in figure 5.58. Here a similar voltammogram compared to figure 5.56 is visible. From the figure, it can be seen the a minimal mass increase is starting from circa -0.75 V in the cathodic direction of the scan, which keeps increasing up to around -0.10 V in the anodic direction of the scan. In this window a maximum mass of 0.14 µg is deposited at the surface of the electrode of the EQCM, which indicates a maximum change in mass per unit area of 0.73 $\mu g\,cm^{-2}$, which can be neglected due to its proximity to zero.

Using the graph of Δf versus ΔQ obtained using the EQCM method, the M/z values are calculated and compared with the voltammogram and the characteristic values for M/z according to the literature. Table 5.23 shows the M/z values for the graphs visible in figure 5.58. For this sample, no potential ranges with a distinctive M/z value can be observed, with a maximum M/z value of 3.8 $\mu g\,cm^{-2}$. This concludes that, due to the low M/z values over the complete potential range, no active elements and reactions are observed.

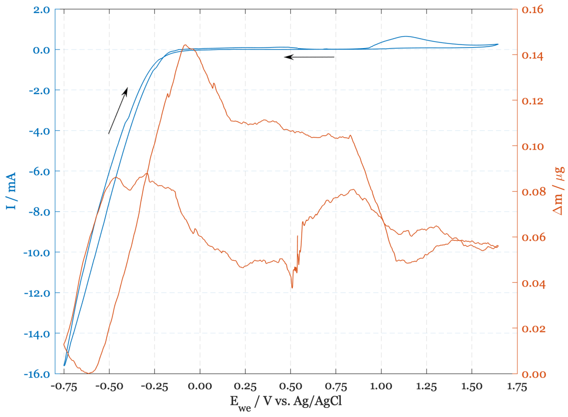

Figure 5.58: Cyclic voltammogram (—) for 18GL3E sample in 0.5 M HNO_3 at pH 1.10 and corresponding curve for Δm (—)

Table 5.23: M/z for 18GL3E sample in 0.5 M HNO_3 solution at pH = 1.10

pH	Potential range (V)			M/z ($g mol^{-1}$)
1.20	0.50	to	−0.14	1.6 ± 0.5
	−0.14	to	−0.60	0.1 ± 0.5
	−0.60	to	−0.80	0.1 ± 0.5
	−0.80	to	−0.51	0.1 ± 0.5
	−0.51	to	−0.15	0.5 ± 0.5
	−0.15	to	0.85	3.8 ± 0.5
	0.85	to	1.60	0.2 ± 0.5
	1.60	to	0.50	1.8 ± 0.5

5.9. Electrochemical cleaning of electrodes

After each CV or EQCM experiment, some electrodeposited material remains on the surface of the electrode (CV) or the quartz crystal resonator (EQCM). The electrode used for cyclic voltammetry needs, according to the manufacturer, cleaning using a special polishing kit. This was done after the experiments were finished. As for the EQCM resonators, according to the manufacturers, they are made to be used only once. Since the cost of one resonator is significant, it is desired to reuse it. Santos et al. (2007) and García-Miranda Ferrari et al.

(2018) mention the cleaning of the resonators. They both used a 0.1 M H_2SO_4 solution until characteristic CV-cures of the platinum in acid were obtained, where a potential window between -0.25 V and 1.20 V (vs. SCE) was used.

In this research, the electrodes were cleaned using a 0.5 M HNO_3 solution, which is also used for the leaching experiments. After electrodeposition is finished, the electrode is immersed in the HNO_3 solution for at least 20 cycles until characteristic CV curves are observed. Figure 5.59 shows the characteristic CV curve for a pure 0.5 M HNO_3 solution. The optimal potential window was decided to be between -0.3 V and 1.6 V. This window was chosen, because with higher or lower potentials the current will increase or decrease to infinity without adding any extra cleaning effects of the electrode. The cleaning principle is based on the change between reduction and oxidation cycles, and not on a maximum current peak. This means that after an experiment, sufficient cycles are needed in order to generate curves similar to the one shown in figure 5.59.

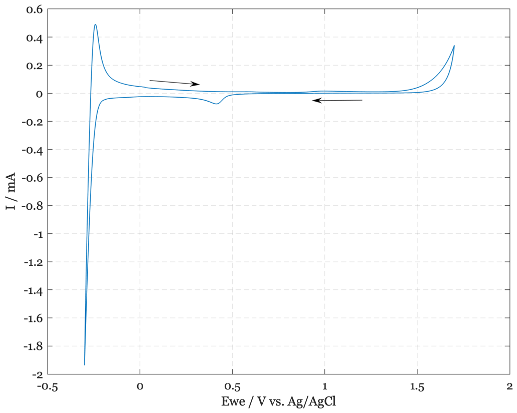

Figure 5.59: Cyclic voltammogram for a clean 0.5 M HNO_3 solution

Figure 5.60 shows 21 cycles of the cleaning process of the quartz resonator. The first cycle shows a clear peak around 0.40 V. This peak is caused by material left on the electrode. When the electric sweep of the potential takes place for the second cycle, the peak is reduced. When the amount of cycles increases the voltammogram returns to the characteristic curve shown in figure 5.59, where the arrow indicates the decrease of the peak current. The decrease of peak current is growing with each cycle, which is shown in figure 5.60, where for each cycle the maximum peak current current is plotted.

Figure 5.60 also shows the frequency change measured by the EQCM. This curve shows an increase in the frequency change that indicates that the mass on the electrode surface is decreasing as the number of cycles is increased. At the start of the cleaning process, a minimum frequency of 6.17 kHz is found, which is equal to a mass of 0.68 µg. Finally, the frequency and mass on the electrode will decrease to zero, after which the electrode quartz resonator can be reused for the next experiment.

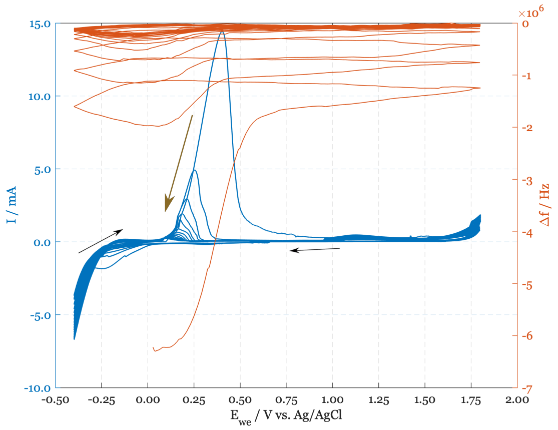

Figure 5.60: Cyclic voltammogram (—) for 0.5 M HNO_3 cleaning solution and corresponding frequency change (—)

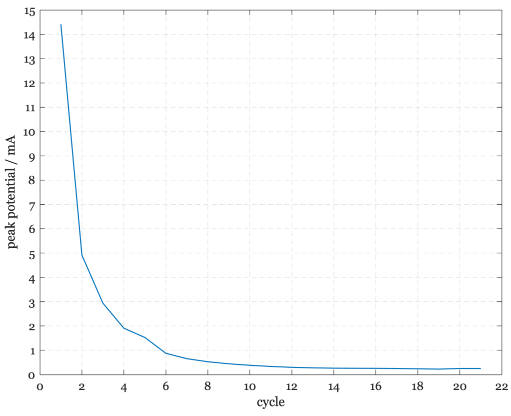

Figure 5.61: Peak potentials for all cycles shown in figure 5.60.

6

Discussion

This chapter discusses the results obtained in chapter 5, and will be delving deeper into the meaning, importance and relevance of the results. It focuses on the explanation and evaluation of what has been found and how this relates to the literature review of chapter 3. All experiments and modelled results evaluated in chapter 5 will be evaluated and compared to each other to discuss what the results mean, why they do or do not matter and what practical actions or scientific studies are suggested for the future.

First, the sensitivity analysis using cyclic voltammetry models is evaluated for the different parameters. This is linked to the first research question on how different chemical properties will influence the electrochemical behaviour of the voltammogram. This is followed by a discussion of all chemical compositions, synthetic ores and ores from the DRC to answer to other research questions on the electrochemical properties, the possibility for selective electroplating, what influence a varying mineral composition has and if it is possible to relate the parameters of these three substances with each other.

6.1. Sensitivity analysis

The first obtained results are from the sensitivity analysis with simulations of cyclic voltammetry (CV) obtained in section 5.1 to evaluate differences in parameters. Here, the diffusion coefficient, initial concentration, charge-transfer coefficient, the number of involved electrons and the temperature were evaluated for different values. For all values, different voltammograms were generated and their differences and similarities will be discussed in this section.

The peak potentials of the evaluated parameters show that an increase was observed in the voltammogram when a parameter was in- or decreased. This is used to answer the first research question. Using a theoretical model the more abstract parameters can be evaluated. Values such as the initial concentration and the temperature can be tested more easily in an experiment, where the other parameters are not generated easily.

Table 6.1 shows a summary of the minimum and maximum cathodic peak current density of figures 5.1, 5.3, 5.5, 5.7 and 5.9, given in $\mathrm{mA\,cm^{-2}}$. It can be seen that the largest influence is contributed by the number of electrons that have been transferred in the solution. An increase for the difference of the amount of electrons involved in the reaction is the largest, with a value of almost 21 $\mathrm{mA\,cm^{-2}}$ where the evaluated values for n increase with a factor of five. The smallest increase is visible for α with a minimal difference of 0.06, where the evaluated values for α have increased with a factor of 99. This indicates that n is indeed one of the most important properties within the reaction, since it generates a large difference in the peak potential with a moderate increase in the evaluated value.

For the other parameters, for C_0 a difference of 5.75 $\mathrm{mA\,cm^{-2}}$ is observed with an increase of the tested value of a factor five. D generates a difference of 7.47 $\mathrm{mA\,cm^{-2}}$ where the increasing factor for the evaluated values is 1.00×10^4 For T, the difference is 0.26 $\mathrm{mA\,cm^{-2}}$, where the factor of the evaluated values is equal to 1.28. When all the parameters are evaluated, it can be said that the amount of electrons transferred in the solution is the most significant parameter evaluated in this thesis.

It needs to be noted that an electron transfer of five electrons does not occur very often. Electron transfers of one, two or three electrons are observed more generally. Looking at a maximum of three electrons transferred, the difference between one and three electrons is 9.5 $\mathrm{mA\,cm^{-2}}$, where the increasing factor is equal to three. However, using this value it would still continue to be the electrochemical parameter with the largest influence on the shape of the voltammogram. So, this data contributes a clearer understanding of the parameters influencing the behaviour of the shape of the voltammogram.

Table 6.1: Overview of the minimum and maximum current densities combined with evaluated parameter

Parameter	Unit	Minimum ($\mathrm{mA\,cm^{-2}}$)	Evaluated value	Maximum ($\mathrm{mA\,cm^{-2}}$)	Evaluated value
D	$\mathrm{cm^2\,s^{-1}}$	−0.01	1.00×10^{-8}	−7.48	1.00×10^{-4}
C_0	$\mathrm{mol\,cm^{-3}}$	−1.20	0.50	−6.95	2.50
α	-	−2.33	0.01	−2.39	0.99
n	-	−2.40	1.00	−23.00	5.00
T	K	−2.43	283.15	−2.17	363.15

When the current densities are plotted against the evaluated values, the relationship between them can be evaluated and it is possible to determine if the relation is linear, exponential or other, which can be seen in figures 5.2, 5.4, 5.6, 5.8 and 5.10. Using the simulations, it was found that the peaks of the diffusion coefficient, the initial concentration, the number of electrons transferred and the temperature generated a linear relationship. Only for the charge-transfer coefficient an exponential relationship was found. All generated trend lines using the tested data points generated an R^2-value between 0.95 and 1.00, which indicates a large correlation for the plots.

Another difference is that the linear relationship of the temperature is positive, has a positive slope, and not as the other parameters, a negative slope for the trendline. This indicates that an increasing temperature has a negative effect and peak on the current density of the voltammogram. This provides a new insight into the relationship between temperature and the other parameters tested.

As a remark, this sensitivity analysis is carried out for sole parameters within a mathematical model. In real experiments these parameters can also change when one parameter is adjusted. For example, when the parameter for temperature is changed this will also indirectly change the diffusion and transfer coefficient, because they are linked to each other. However, this section demonstrated how certain parameters will change the shape of the voltammogram and how different shapes and forms of the voltammogram can be explained.

6.2. Chemical compositions

This section discusses the differences and similarities between the solutions made using fabricated chemical compositions. The solutions of $CoCl_2$ with (section 5.2) and without adding HNO_3 (section 5.3) to increase the pH to more acidic conditions were compared to each other. Two types of cobalt-bearing solutions, $CoCl_2$ (section 5.2) and $CoSO_4$ (section 5.4), were tested for similarities between their voltammograms together with $CuSO_4$ (section 5.5). $CoCl_2$ and $CuSO_4$ (section 5.6) were tested and compared in a mixed solution for different pH levels. Afterwards, these values were compared with synthetic ores (section 5.7) and ores coming from the DRC (section 5.8), which will also be discussed.

6.2.1. $CoCl_2$ vs. $CoCl_2$ with HNO_3

For $CoCl_2$ the voltammograms were given in section 5.2 and 5.3. Both pH values of 5.80 and 1.70 show differences in the voltammograms. Figure 6.1 shows both voltammograms in one plot. The used conditions such as concentration, scan rate and temperature are identical. It is clear that for a higher pH the current peak is more than three times as high in the anodic direction and more than two times as high in the cathodic direction of the scan. For substances, the temperature and α are almost the same. Therefore, the difference in the diffusion coefficient must originate from the change in shape of the voltammogram. For the solution at pH 5.80, the value for D was higher than for the solution at pH 1.70, which indicates that more cobalt was diffused per unit area and therefore a larger amount was reduced.

The peak current for solutions are different, but the potential where cobalt reduction and oxidation occurs are similar. The reduction of both solutions is present around -1.10 V and the oxidation occurred around 0.05 V. These results do not fit with the theory that the standard reduction potential of the reduction of Co^{2+} is -0.28 V. Most probably this is caused by the change in the diffusion coefficient and the presence of chloride in the solution, which can cause different electrochemical behaviour.

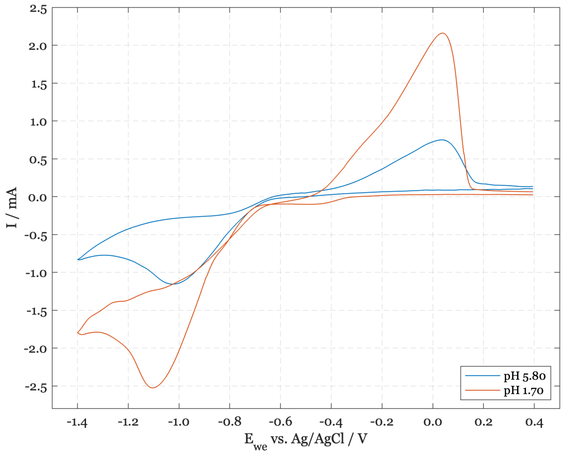

Figure 6.1: Cyclic voltammogram 0.05 M $CoCl_2$ for pH 5.80 and 1.70 shown in figures 5.12 and 5.17. The scan rate was 100 $mV s^{-1}$

Another difference can be observed around a potential of -0.45 V in the cathodic direction of the scan. Here, a small peak was visible for the solution with pH 1.70, where for the other solution it was not present. This difference can be explained by the change in pH. For a pH < 4.00, the deposition of cobalt happens with adsorbed hydrogen, which is visible is the hydrogen evolution reaction (HER) around this potential. For pH > 4.00, the deposition of cobalt proceeds through the reduction of cobalt from $Co(OH)_2$, where no HER is present. Since the pH of the solution is higher than 4.00, no peak for the HER reaction is visible in figure 6.1.

6.2.2. $CoCl_2$ vs. $CoSO_4$ vs. $CuSO_4$

This section discusses the differences and similarities of 0.05 M solution of $CoCl_2$, $CoSO_4$ and $CuSO_4$ (sections 5.2, 5.4 and 5.5). These substances were diluted in demineralised water only, so no other impurities were present. For $CoCl_2$ and $CoSO_4$ the values for α were similar and $CoCl_2$ had a higher value for D than $CoSO_4$. This indicates that more cobalt was diffused per unit area and therefore a larger amount was reduced when a solution of $CoCl_2$ was used.

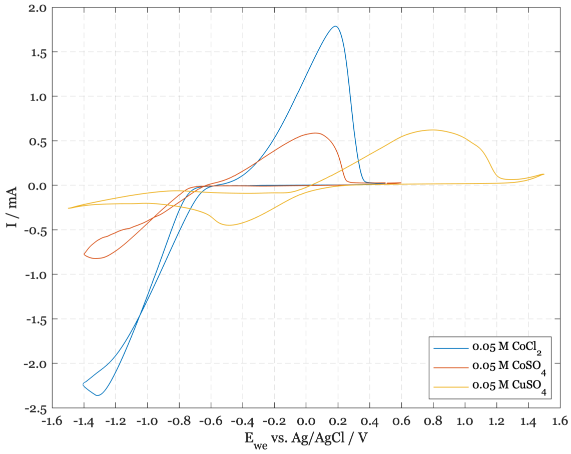

Figure 6.2: Cyclic voltammogram 0.05 M $CoCl_2$, 0.05 M $CoSO_4$ and 0.05 M $CuSO_4$. The scan rate was 100 $mV s^{-1}$ for all solutions

Figure 6.2 shows three single voltammograms from figures 5.12, 5.20 and 5.22. For both cobalt-bearing solutions, the potentials for the oxidation and reduction peaks were similar, respectively around 0.10 V and -1.30 V. It is clear that the peak for $CoCl_2$ is significantly higher than the peak for $CoSO_4$. This indicates that chloride has a more positive and negative influence on the peak density then sulfide does. However the most important parameter is that the reduction of both solutions is around a potential of -1.30 V.

For $CuSO_4$ the oxidation and reduction peaks occur respectively around 0.80 V and -0.50 V. The reduction differs from the value known in the literature for direct cobalt reduction, which indicates that the sulfide has a limiting influence compared to the standard potential. Compared to the cobalt-bearing solution, the value for α is larger with a value of 0.25 and a value for D that is smaller with a factor 1.00×10^{-2} compared to the other solution shown in figure 6.2. This indicates that less diffusion is occurring per unit area and the electroplating process is less smooth. The higher value for α can be explained by a more characteristic appearance of the voltammogram, where the distance between both peaks is more equally distributed.

6.2.3. $CuSO_4$ mixed with $CoCl_2$

Two solution of 0.05 M $CuSO_4$ and 0.05 M $CoCl_2$ were mixed to indicate their response to the shape of the voltammogram. Section 6.2.2 evaluated the pure solutions. According to the literature it was expected to see peaks around similar potentials for both copper and cobalt. Figure 6.3 shows two voltammograms from figures 5.25 and 5.27. It is clear that for pH 5.60 the peaks in both cathodic and anodic directions of the scan are larger then for pH 1.50 up to a factor of two, except the peak around -0.25 V. This indicates that HNO_3 suppresses the peak current of the solution, as this is the only difference between the two substances.

From the previous section, the potentials for copper and cobalt were estimated around -0.50 V and -1.30 V. For cobalt the potential is similar for pH 1.50, where no distinctive peak is visible for pH 5.60. Two peaks are visible around -0.25 V, which therefore is contributed to the reduction of copper. For the voltammogram at pH 1.50 an extra peak is visible around -0.85 V, which is assumed to be the reaction for the HER, since it occurs at pH < 4.00 and this reaction occurs prior to the reduction of cobalt.

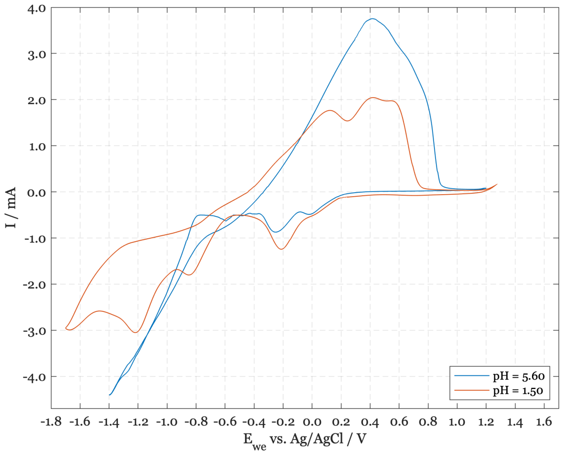

Figure 6.3: Cyclic voltammogram 0.05 M $CoCl_2$ mixed with 0.05 M $CuSO_4$. The scan rate was 50 $mV s^{-1}$

The values for α and D are similar, which indicates reactions for cobalt reduction in both solutions are similar. The diffusion coefficient for pH 1.50 is slightly larger, but is still in the same order of significance. Using the EQCM, figures 5.29 and 5.30 give maximum depositions of 16.0 µg and 23.0 µg for pH 5.60 and 1.50. A higher mass increase for the pH 1.50 solution can be clarified by the HER reaction, which generates small H_2 bubbles at the surface of the resonator. This was also visible when the experiments were conducted.

Figure 6.3 suggests that for pH 1.50 an extra HER is taking place. However, based on the findings by studying the M/z values, no evidence of this reaction were noticed in the cathodic direction of the scan. When the scan was reversed, a value around 11.0 $g mol^{-1}$ was visible, which is close to the characteristic value of 15.24 $g mol^{-1}$ but it is more plausible that the HER is occurring. This is because the low pH and supporting studies have indicated this, however the reliability of this data is reduced.

6.2.4. Overview

The past sections have discussed the parameters obtained with the CV and EQCM and the experiments provided new insights into the relationship between different substances and the shape of the voltammograms and the corresponding reaction parameters. Table 6.2 shows the parameters of all experiments carried out in this thesis using chemical compositions together with similar substances in different environments which are based on the findings in similar studies.

Table 6.2: Overview of diffusion coefficient of Co(II) in various electrolyte solutions (modified from: Li et al., 2014)

#	Authors	System	Temperature (K)	α	D ($cm^2 s^{-1}$)
1	Carlin et al.	$CoCl_2$ in $AlCl_3$-EMIC	295	-	4.40×10^{-7}
2	Su et al.	$Co(BF_4)_2$ in $BMIMBF_4$	333	0.18	1.76×10^{-8}
3	Yang et al.	$CoCl_2$ in urea-NaBr-LBr	373	0.45	2.50×10^{-6}
4	Xu et al.	$CoCl_2$ in urea-NaBr-acetamide	353	0.26	2.83×10^{-7}
5	Wang et al.	$CoCl_2$ in urea-NaBr-acetamide	353	0.23	2.24×10^{-7}
6	Fakui et al.	$Co(TFSA)_2$ in BMPTFSA	300	-	7.20×10^{-9}
7	Li et al.	$CoCl_2$ in urea-choline chloride	373	0.36	1.70×10^{-6}
8	This work	$CoCl_2$	298	0.11	8.82×10^{-6}
9	This work	$CoCl_2$ in HNO_3	298	0.12	6.15×10^{-6}
10	This work	$CoSO_4$	293	0.09	1.10×10^{-6}
11	This work	$CuSO_4$	293	0.25	6.61×10^{-8}
12	This work	$CoCl_2$ with $CuSO_4$ (pH = 5.60)	293	0.25	4.34×10^{-8}
13	This work	$CoCl_2$ with $CuSO_4$ (pH = 1.50)	293	0.25	6.61×10^{-8}

Comparing all systems, a variety of temperatures can be seen. These implicate that when higher temperatures are used, higher values for α can be expected, but no particular differences for D are. For example, Yang et al. (1995) and Li et al. (2014) used a temperature of 373 K, which resulted in higher values of α between 0.36 and 0.45. For D, both values of Yang et al. (1995) and Li et al. (2014) are significantly larger, with an order of significance of 1.00×10^{-6} However, this is also observed with temperatures of 293 K and no clear relation can be observed.

Overall, all results in this thesis look plausible as table 6.2 shows the literature states the values of α between 0.10 and 0.50 to be regular, and values for D in order of significance between 1.00×10^{-6} and 1.00×10^{-9} as well. To increase the reliability of the data, further research is needed to establish a more clear relationship between the chemical substances used and temperature, α and D.

6.3. SD069 vs. SD073

For the synthetic oxyhydroxide samples doped with 10 mol% *(SD069)* and 8 mol% *(SD073)* of cobalt, differences in the voltammogram were be observed. Figure 6.4 shows two voltammograms from figures 5.31 and 5.35, where differences between both samples are visible at pH 5.60. The values for the current of the peaks is significantly low, indicating low electrochemical activity, where for SD073 four peaks in the cathodic direction of the scan are visible at 0.85 V, 0.00 V, -0.30 and -0.65 V. For SD069 also four peaks are visible at 1.05 V, 0.20 V, -0.05 V and more negative around -0.60 V. It is assumed that these are observed for similar reactions, where SD069 shown more electrochemical activity. This can be explained by the larger amount of cobalt.

In previous experiments in this thesis, cobalt reduction occurred around the potential of -1.25 V, which is not visible for both samples at pH 5.60. At lower potentials than -0.80 V the current dropped until infinity and the voltammogram became unstable. The data suggests that cobalt reduction is not occurring at those intervals because iron is present in the solution. From the M/z values it is observed that at pH 5.80 for SD069 the reduction of both cobalt and iron is occurring, where for SD073 only the direct reduction of cobalt is observed without the reduction of iron(III) to iron(II). For both experiments, the reduction of cobalt is occurring at -0.05 V (SD069) for SD069 and 0.85 V (SD073). This result was unexpected because it is a significant difference of the potential between both reductions of cobalt, but indicates that a higher percentage of cobalt in an iron oxyhydroxide changes the electrochemical behaviour of the substance. Looking at the mass changes for pH 5.60, a larger mass increase is shown for SD069 (1.5 µg) then for SD073 (0.09 µg), which can be clarified by the higher percentage of cobalt.

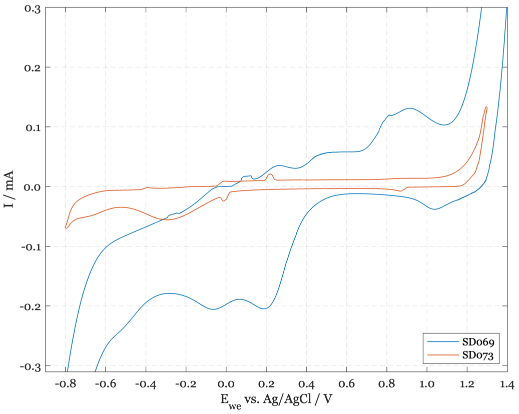

Figure 6.4: Voltammogram for SD069 and SD073 synthetic samples is 0.5 M HNO_3 for pH 5.60, where $\upsilon = 50\ \mathrm{mV\,s^{-1}}$

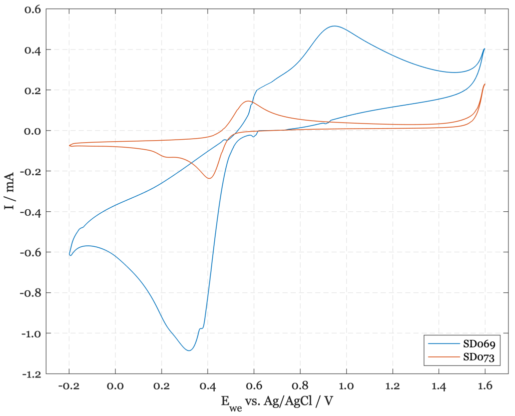

Figure 6.5: Voltammogram for SD069 and SD073 synthetic samples is 0.5 M HNO_3 for pH 1.10, where $\upsilon = 50\ \mathrm{mV\,s^{-1}}$

Figure 6.5 shows two voltammograms from figures 5.32 and 5.36, where the differences between both samples are visible at pH 1.10. The values for the current of the peaks are larger than for pH 5.60, indicating higher electrochemical activity. For SD073 two peaks in the cathodic direction of the scan are visible at 0.40 V and 0.25 V. For SD069 three peaks are visible at 0.60 V, 0.38 V and 0.35 V. It is assumed that these are observed for similar reactions, where SD069 has more electrochemical activity indicated by the larger peak currents. This can be explained by the larger amount of cobalt present in the solution and is in line with the findings for the same substance at pH 1.10.

For the values for cobalt reduction, no knowledge of the potentials used in the previous experiments could be used to identify the occurring reactions. Looking at the M/z values for SD069 shows that the reduction of cobalt with absorbed hydrogen is occurring in the 1.60 V to 0.45 V window, which would indicate the peak visible at 0.60 V. For SD073 the peak for deposition of cobalt is at 0.40 V. This is relatively close to each other and can be accepted as the potential for cobalt reduction, where the small difference can be attributed to the change in the cobalt percentage present in the samples. For both samples, similar mass increases are visible, which indicate no differences are observed and related to the different cobalt percentages.

The experiments of the synthetic samples provide new insights into the relationship between iron and cobalt, and the possibility to apply selective leaching when both elements are present in a leaching solution. For sample SD073 at pH 1.10, M/z values attributed to both reactions were observed, which makes it plausible that at a constant potential these element will come out of the solution. Sample pH 5.60 does not show activity of iron. However, for pH 5.60 electrochemical activity for iron and cobalt is observed, where SD073 only shows cobalt related activity. To explore these observation further research is needed to establish more reliable and extensive results.

6.4. Ores from Mutanda mining operation

Table 6.3 gives an overview of the reaction parameters obtained in the experiments with the samples from the Mutanda mine as discussed in section 5.8. It is clear that 18GL3E shows no parameters, which is caused by the lack of electrochemical activity for the sample. No reactions related to cobalt, copper or iron were observed and therefore, no parameters could be observed. Only a relatively small mass increase was observed for the sample, which can be neglected compared to the mass changes of the other samples.

Sample 18GL33 and 18GL35 both showed irreversible reactions, which can be explained by their similar composition looking at their mass percentages. However, α for both samples is different. These results do not fit with the theory that similar substances would produce similar parameters. The only plausible reason for these results could be the small variations in the mineralogy looking at minerals as dolomite, quartz, chalcocite and magnesiochlorite. However, these changes are minimal and it remains unclear what origins this difference has. The samples show similar parameters for D and k_s, which is in line with the expectations. Both samples show the highest mass increase per unit area, which shows that larger fractions of bornite do not influence the deposition of cobalt.

Samples 18GL31 and 18GL3D both contain fractions of chalcopyrite. However, 18GL3D showed no activity for cobalt which indicates different parameters for these samples. These results do not fit with the theory that for similar compositions for one voltammogram no peak is observed. Therefore, α varies, as do the values for D and k_s. Due to the lack of available data, the results cannot confirm any relationship between these samples and further research would be needed to make this more clear.

Sample 18GL3F contains the most carrollite, indicating the largest fraction of cobalt, but shows an average mass increase lower than samples 18GL33 and 18GL35 that have a lower mass percentage of carrollite which should indicate lower fractions of cobalt. Similarities are present looking at D, indicating a similar diffusion coefficient, which can be explained by a common mineral composition in the ore. The largest mass percentage of carrollite would indicate the quasi-reversible reaction for sample 18GL3F, where the other two are irreversible.

Table 6.3: Overview of values for α, D, k_s and Δm obtained from experiments using the Mutanda ores

System	α (-)	D ($cm^2 s^{-1}$)	k_s ($cm s^{-1}$)	Δm ($\mu g cm^{-2}$)	Reaction
18GL31	0.49	1.04×10^{-10}	4.27×10^{-5}	2.75	Quasi-reversible
18GL33	0.77	1.85×10^{-6}	2.74×10^{-8}	38.00	Irreversible
18GL35	0.21	2.61×10^{-7}	1.03×10^{-7}	39.42	Irreversible
18GL3D*	0.37	1.92×10^{-7}	1.37×10^{-2}	4.49	Quasi-reversible
18GL3E**	-	-	-	0.73	-
18GL3F	0.37	5.73×10^{-7}	3.24×10^{-2}	14.90	Quasi-reversible

* = No peaks for cobalt are present, peaks for copper are used instead.

** = No electrochemical activity observed.

The ores from the Mutanda operation show similar shapes looking at the voltammogram. Figure 6.6 shows all voltammograms combined from figures 5.41, 5.44, 5.47, 5.50, 5.53 and 5.56, . Peaks, larger and smaller, are visible in the cathodic direction of the scan. A small dimple is visible at -0.20 V and a large drop in the current afterwards continuing until a potential of -0.80 V. In the anodic direction of the scan a larger peak is visible between 0.20 V and 0.40 V and a smaller peak is visible between 0.80 V and 1.40 V.

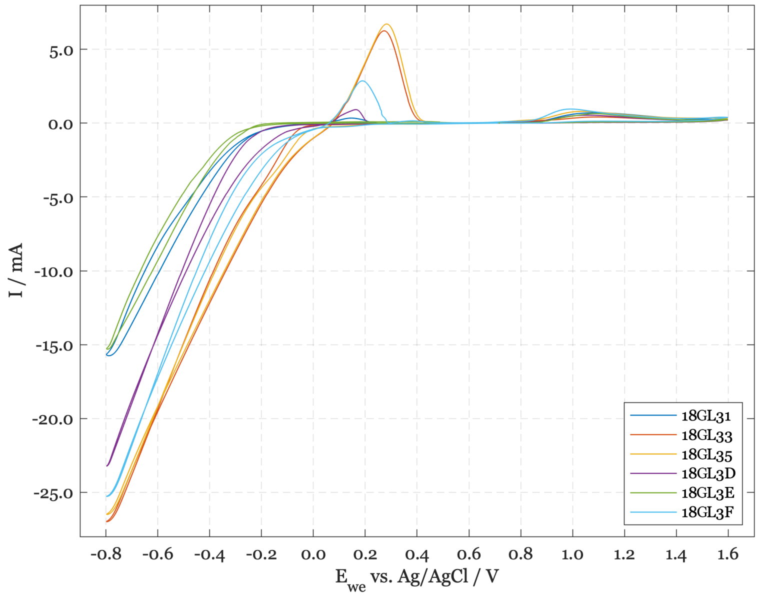

Figure 6.6: Cyclic voltammogram of 0.75 g of DRC-ore in 0.5 M HNO_3 with υ = 50 mVs^{-1}

At first, when these potentials are compared with the potentials discussed in the previous sections of the discussion, it would be assumed the peak around -0.20 V is associated with copper reduction and the larger drop in potential with cobalt reduction. In the same way, it would be expected that the 0.30 V peak corresponds to copper oxidation and the 1.00 V peak with cobalt oxidation.

From the figure it can be seen that samples 18GL33 and 18GL35 have the highest peaks in both the anodic and cathodic direction of the scan. Looking at the mineralogy, both samples contain larger amounts of bornite compared to the other samples. This is an iron-bearing mineral, so it can be assumed that a higher mass percentage of bornite will increase the electrochemical activity in the form of higher peaks.

Sample 18GL3F produces an average peak compared to the other samples. This sample contains the largest mass percentage of carrollite, which indicates a high percentage of cobalt. A smaller fraction of copper-bearing ores is present, which indicates the lower peaks in both the cathodic and anodic direction of the scan. Compared with samples 18GL33 and 18GL35, this would indicate that copper is the dominant element for the size of the peak current as the largest peak. However, the smaller peak at 1.00 V shows the largest peak, indicating cobalt would be the most electrochemical active element.

Samples 18GL31 and 18GL3D have lower peaks in the anodic direction of the scan, but sample 18GL3D shows a more negative current for the large drop at the cathodic current. The same applies as with previous sample; a lower mass percentage of carrollite is present and the sample contains a larger fraction of chalcopyrite. The difference in electrochemical activity between both samples can be explained by their mass percentages of chalcopyrite, which can explain a correlation between the mass percentage of copper and the peak behaviour of the voltammogram.

Sample 18GL3E contains the least mass percentage of cobalt, since no carrollite is present. Equal mass percentages of dolomite, quartz, K-feldspar, phlogopite and magnesiochlorite can be found, which suggests the combination of the minerals do not produce any significant peaks. None of these minerals contain iron, copper or cobalt so it is clear this causes the lack of electrochemical activity shown in the voltammogram. Due to the low concentration of carrollite and heterogenite, no electrochemical behaviour is observed, which is in line with the expectation for minerals present in this sample.

Comparing the samples for the obtained M/z values, it is clear that sample 18GL3E does not show any electrochemical activity due to it's lack of electrochemically active minerals, i.e. copper, cobalt and iron. Sample 18GL3D shows no values linked to cobalt reduction, where the peak in the anodic direction is associated with copper. This sample contains a larger mass percentage of chalcopyrite then carrollite. This provides a new insight into the relationship between carrollite and chalcopyrite; if the mass percentage of chalcopyrite is higher, no activity for cobalt is observed.

Sample 18GL31 shows similar behaviour as sample 18GL3D where chalcopyrite is present. However, the fraction of carrollite is larger which results in electrochemical activity in cobalt being measured in the form of the reduction of cobalt with adsorbed hydrogen. The larger peak in the anodic direction of the scan, however, is attributed to copper or iron. Due to the lack of available data, the results cannot confirm if the element present in this reaction is either copper or iron. The data of these samples shows that it would be possible to apply the use of electrochemistry for the selective electrowinning of copper and cobalt.

Samples 18GL33, 18GL35 and 18GL3F have in common that only electrochemical activity is observed indicating reactions involving cobalt. The cobalt reduction reaction involving adsorbed hydrogen occurs in the potential window between 0.72 V and -0.29 V for all samples, which indicates no correlation is visible between the values obtained with previous experiments that indicated that cobalt reduction occurs around a more negative potential. These samples contain minimal mass percentages of chalcopyrite, but do contain fractions of bornite. Both minerals contain copper, iron and sulfide in different ratios. The data suggests that chalcopyrite has a larger influence on cobalt activity then bornite and suggests that no selective electrowinning can happen when larger mass percentages of bornite are present in the ore.

7

Conclusions and recommendations

In this chapter the final conclusions of this research are drawn based upon what is presented and discussed in chapters 5 and 6. Afterwards several recommendations for further research within this topic are proposed.

7.1. Conclusions

Here the general conclusions on this research are drawn by answering the five different research questions as presented in chapter 2. These research questions were set in order to reach the objective of this research. The objective for this research was stated as follows:

> *Investigate what causes the differences in the electrochemical behaviour of copper-cobalt minerals in aqueous solutions using chemical compositions, synthetic and real ores, and find a correlation between the obtained results using the graphs generated using CV and EQCM-techniques.*

In order to reach the set objective mentioned above, a separate answer to the five research questions is formulated below.

1. *How do different electrochemical properties influence the electrochemical behaviour of cobalt in solutions using cyclic voltammetry simulations?*

The sensitivity analysis as presented in section 5.1 and discussed in section 6.1 made a prognosis on the behaviour of the shape of the voltammogram by changing different parameters in the model. The prognosis was based upon changes in the diffusion coefficient, initial concentration, charge-transfer coefficient, the number of involved electrons and the temperature. Looking at the peak currents and the applied potentials, it can be concluded that the number of electrons involved in the reaction have the largest influence on the behaviour on the shape of the voltammogram. D and C_0 have changed the shape significantly, but the factor of change in the evaluated parameters is much higher and generates a smaller change in the peak currents. T and α can be neglected looking at their influence on the minimum and maximum changes in peak current.

This finding clearly illustrates that the number of electrons involved changes by far changes the electrochemical activity the most, but it also raises the question of the importance of the other parameters. Their influence has less impact on the peak current, though it is expected that parameters such as α and T would also have a larger contribution to the change in the voltammogram. However, this can be attributed to the fact taht this analysis was carried out by changing single parameters within a model. In "real-life" experiments, these parameters can be changed when another parameter is adjusted. For example, when the T is changed this will indirectly change D and α, because they are linked to each other.

2. *What are the most important electrochemical properties of multiple cobalt-bearing solutions, investigated with the help of cyclic voltammetry (CV) and the electrochemical quartz crystal microbalance (EQCM)?*

It has been discovered that changing the pH from an alkaline environment to a more acidic environment changes the shape of the voltammogram. The peak current will increase up to a factor three, while the peak potential of the reaction remains constant for both the peaks in the cathodic and anodic direction of the scan. As suggested in the literature, this research found that cobalt reduction occurs directly or through cobalt deposition where hydrogen is absorbed with the hydrogen evolution reaction (HER) in an acidic environment ($pH < 4.00$). At alkaline pH-levels ($pH > 4.00$) cobalt reduction and deposition is observed through cobalt hydroxide.

Cobalt chloride present in a mixed solution with copper sulfide results, looking in the cathodic direction of the scan, in distinctive peaks for pH 1.50. However, for pH 5.60 more negative currents are observed indicating that HNO_3 suppresses the maximum peak current, where in the pure solutions of $CoCl_2$ and $CoCl_2 + HNO_3$ mentioned above, it was the other way around. This indicates that mixed solutions behave differently than when both substances are tested individually.

The reaction parameters conclude that the charge transfer coefficient (α) is relatively low for $CoCl_2$ and $CoSO_4$, where higher values are observed for $CuSO_4$ and the mixed solution of $CoCl_2$ and $CuSO_4$. This indicates that when a copper is added to a solution, the value charge-transfer coefficient will increase with a factor up to 2.5. When the temperature increases, it can be concluded that the charge-transfer coefficient will increase. The values for D are all in the expected order of magnitude. All reactions are classified as irreversible or quasi-reversible indicating the reaction rate is slow and extreme electrode potentials are needed to drive the electron transfer and register current on the potentiostat.

3. *Can selective electrodeposition be applied, so reduction and/or deposition is possible so other elements than cobalt (Co), such as copper (Cu) and iron (Fe), can be gained in the same solution by using their characteristic reduction potentials?*

This thesis clearly illustrates that different potentials are observed when mixed solutions, synthetic ores and DRC-ores are evaluated using CV, but it also illustrates that this does not happen similarly in the tested environments. For the mixed solution it can be concluded that selective electrodeposition is possible by switching the potential between -1.20 V for cobalt and -0.20 V for copper reduction. However, no extensive analysis, i.e. QEMSCAN or FTIR, is carried out to analyse the mineral and elemental composition of the electrodeposited material, and this would be needed to make sure copper or cobalt is indeed deposited on the electrode.

The synthetic ores show that different peaks can be assigned to both cobalt and iron, suggesting selective electrodeposition is possible. However, it is found that the reaction involving iron applies to the reduction of Fe(III) to Fe(II), which is a reduction reaction, and no electrodeposition actually occurs. This indicates that for the synthetic ores only containing iron and cobalt, no selective electrodeposition is possible.

The ores from the Mutanda mining operation showed that selective electrowinning has potential for particular ores. The ores containing higher mass percentages of bornite have no potential for this application. Selective electrodeposition is possible for ores containing a minimum mass percentages of chalcopyrite (> 16%) and carrollite (> 45%).

4. *What is the influence of a varying mineralogy and mineral structure on the electrochemical behaviour of the cobalt-bearing ores and the shape of the corresponding voltammogram?*

For the synthetic ores, it can be concluded that increasing the cobalt percentage compared to the iron will have a positive effect on the increase of both peak currents in the anodic and cathodic direction of the scan. On top of that, increasing the mol% of cobalt adds more peaks to the voltammogram indicating the higher the cobalt percentage, the more likely this can also be noticed in the voltammogram. This is in line with the expectation that the a characteristic peak for an chemical reaction will increase if the substance is more abundant.

The DRC-ores make it clear that the mineralogy of the sample has a major influence on the shape of the voltammogram. This research clearly illustrates that minerals containing larger fractions of bornite induce larger peaks than cobalt-bearing minerals, but it also raises the question why chalcopyrite, also a copper-bearing mineral, is not as dominant. A larger mass percentage of carrolite generates larger peak potentials than similar fractions of chalcopyrite and it can be concluded that if no copper, cobalt or iron is present no electrochemical activity is observed.

5. *Is it possible to find a correlation between the electrochemical properties of chemical compositions, the synthetic iron-cobalt ore and the cobalt-bearing samples from the DRC?*

Comparing all experiments, no overall correlation has been found between the samples. For all experiments similar reactions and electrochemical activity is observed looking at the peak potentials and within the same environment, a correlation can be found. However, when the electrolyte solution or pH changes, the characteristic peak potential of the same reaction does so too. This makes it hard to predict the potential at which electrodeposition will occur.

7.2. Recommendations

The recommendations of this research are divided into recommendations regarding the evaluation of electrochemical properties and behaviour of copper/cobalt-bearing minerals using cyclic voltammetry and the electrochemical quartz crystal microbalance and for future research.

7.2.1. Recommendations regarding the electrochemical properties and behaviour of copper and cobalt-bearing minerals using CV and EQCM

- **Investigate the effect on the shape of the voltammogram and mass curve by using a laboratory setup to get a better knowledge about the behaviour of reaction parameters for "real" experiments.**
  In chapter 5.1 it was concluded that for several parameters, the electrochemical behaviour and therefore the shape of the voltammogram changed when parameters as temperature, initial concentration, diffusion coefficient and the charge-transfer coefficient are changed. However, the effect of these parameters in "real" experiments, possibly resulting in different outcomes, was not quantified within this thesis. Therefore, it is recommended to investigate if parameters change in the same way for laboratory experiments as they do for the modelled results, since this will beof major importance when electrowinning experiments are upscaled to more real-life electrowinning plants.

- **Acquire additional data on using synthetic ores to obtain recovery percentages and a better understanding of the electrochemical behaviour.**
  In this study only iron and cobalt synthetic ores were used to determine influences between different cobalt mol percentages. The QEMSCAN on the DRC-ores gave a good indication on the mineralogy of the samples, but synthetic ores would increase the liability of the results. Further, if it is precisely known what is present in the solution a better expectation of the recovery percentage can be obtained. Due to the leaching stop for the DRC-ores, no recovery percentages for the copper and cobalt bearing minerals are known and it is expected that using synthetic ores would generate better results.

- **Use techniques to evaluate the quantitative analysis of minerals, such as XRF, QEMSCAN and FTIR, to analyse the electrodeposited material before and after electrodeposition.**
  From the data obtained using the EQCM, mass increases are observed at the surface of the electrode and the resonator. After the experiments, it is visible that copper and/or cobalt has electrodeposited. Using the M/z value it can be assessed what reaction did occur, which in turn indicates which element is present at the electrode. However, this is not completely reliable since no analysis is carried out to analyse the exact composition of that material. Therefore, quantitative analysis of minerals can contribute to a better understanding and will increase the certainty of the data so more precise conclusion can be drawn.

7.2.2. Recommendations for further research

- **Investigate parameters such as temperature, magnetic field and impurities on the electrochemical behaviour of the reaction and changes in the yield of electrodeposited material.**
  In this thesis, differences in the electrochemical behaviour were tested for different pH levels above and below 4.00, since it was assumed this is the threshold for cobalt reduction with or without adsorbed hydrogen. The literature review evaluated several effects that can influence the electrochemical behaviour of cobalt. Therefore, additional research is advised to improve the understanding of the influence changing the temperature and concentrations of the electrolyte solution, to apply a magnetic field to it or introduce additives or impurities to the solutions.

- **More data is needed to validate and calibrate the characteristic potentials that can be used for selective electrowinning.**
  In different experiments, different characteristic peak potentials have been observed for copper, cobalt on iron reduction. Therefore, a better understanding of what the origins are of the variations for these peak potentials is needed. It would be expected that similar elements give similar peak potentials and further research can be used to find a correlation between peak potential and a factor such as pH, temperature or similar. If this could be achieved, it would generate a large impact on the prediction of potentials which makes it easier to do experiments in the lab that can be applied to, for example, selective electrowinning in a processing plant.

- **Generate more data of the selective electrowinning experiments in terms of additional (rare) elements, such as Lithium.**
  In this thesis, reduction and deposition of copper, cobalt and iron was observed. In mineral processing plants, solvent extraction (SX) is currently used to separate the copper and cobalt concentrates, after which electrowinning is used to purify the elements so they can be sold to the client. If this step can be cut out, it can reduce costs and contribute to a more environmentally friendly way of cobalt separation. As in other mining projects, selective electrowinning could be a way of reaching this, but further research would be necessary.

Bibliography

Adesokan, B. J., Quan, X., Evgrafov, A., Heiskanen, A., Boisen, A., and Sørensen, M. P. Experimentation and numerical modeling of cyclic voltammetry for electrochemical micro-sized sensors under the influence of electrolyte flow. *Journal of Electroanalytical Chemistry*, 763:141–148, 2016. doi: 10.1016/j.jelechem.2015.12.029.

Alves Dias, P., Blagoeva, D., Pavel, C., and Arvanitidis, N. *Cobalt: demand-supply balances in the transition to electric mobility*. Publications Office of the European Union, Luxembourg, 2018. ISBN 9789279943119. doi: 10.2760/97710.

Attia, P. M. Cyclic voltammetry simulation tutorials, May 2018. URL `https://petermattia.com/cyclic_voltammetry_simulation/index.html`. Online; accessed: 05-07-2019.

Badawy, W. A., Al-Kharafi, F. M., and Al-Ajmi, J. R. Electrochemical behaviour of cobalt in aqueous solutions of different pH. *Journal of Applied Electrochemistry*, 30(6):693–704, 2000. ISSN 0021891X. doi: 10.1023/A:1003893122201.

Bard, A. J. and Faulkner, L. R. *Electrochemical Methods, Fundamentals and Applications*. John Wiley & Sons, Inc., Hoboken, New Jersey, 2nd edition, 2001. ISBN 13 978-9-471-04372-0. doi: 10.1021/ed060pa25.1.

Bertazzoli, R. Studies of the Electrodeposition of Cobalt on a Vitreous Carbon Electrode. *J. Braz. Chem. Soc.*, 8(4):357–362, 1997.

BioLogic. EC-Lab – Application Note #13: Bio-Logic instrument and Quartz Crystal Microbalance (QCM) coupling: Mass measurement during a polypyrrol film deposition, 2009. URL `https://www.bio-logic.net/wp-content/uploads/20101105-application-note-13.pdf`. Online; accessed: 31-07-2019.

BioLogic. EC-Lab & BT-Lab Software: Techniques and Applications, 2019.

Bockris, J. O., Reddy, K., and Gamboa-Aldeco, M. *Modern Electrochemistry 1, 2A, and 2B*. Springer US, New York, United States, 2nd edition, 1998. ISBN 978-0-387-24569-0.

Brown, J. H. Development and Use of a Cyclic Voltammetry Simulator To Introduce Undergraduate Students to Electrochemical Simulations. *Journal of Chemical Education*, 92(9):1490–1496, 2015. ISSN 19381328. doi: 10.1021/acs.jchemed.5b00225.

Buttry, D. A. and Ward, M. D. Measurement of Interfacial Processes at Electrode Surfaces with the Electrochemical Quartz Crystal Microbalance. *Chemical Reviews*, 92(6):1355–1379, 1992. ISSN 15206890. doi: 10.1021/cr00014a006.

Cailteux, J. Lithostratigraphy of the Neoproterozoic Shaba-type (Zaire) Roan Supergroup and metallogenesis of associated stratiform mineralization. *Journal of African Earth Sciences*, 19(4):279–301, 1994. ISSN 1464-343X. doi: https://doi.org/10.1016/0899-5362(94)90015-9.

Cailteux, J. L. and De Putter, T. The Neoproterozoic Katanga Supergroup (D. R. Congo): State-of-the-art and revisions of the lithostratigraphy, sedimentary basin and geodynamic evolution. *Journal of African Earth Sciences*, 150(May 2018):522–531, 2019. ISSN 18791956. doi: 10.1016/j.jafrearsci.2018.07.020.

Cailteux, J., Kampunzu, A., Lerouge, C., Kaputo, A., and Milesi, J. Genesis of sediment-hosted stratiform copper–cobalt deposits, central african copperbelt. *Journal of African Earth Sciences*, 42(1):134–158, 2005. ISSN 1464-343X. doi: https://doi.org/10.1016/j.jafrearsci.2005.08.001. Recent Advances in the Geology and Mineralization of the Central African Copperbelt.

Cao, X., Xu, L., Shi, Y., Wang, Y., and Xue, X. Electrochemical behavior and electrodeposition of cobalt from choline chloride-urea deep eutectic solvent. *Electrochimica Acta*, 295:550–557, 2019. doi: 10.1016/j.electacta.2018.10.163. URL `https://doi.org/10.1016/j.electacta.2018.10.163`.

Carlin, R. T., De Long, H. C., Fuller, J., and Trulove, P. C. Microelectrode evaluation of transition metal-aluminum alloy electrodepositions in chloroaluminate ionic liquids. *Journal of The Electrochemical Society*, 145(5):1598–1607, 1998. doi: 10.1149/1.1838524.

Cheang, C. and Mohamed, N. Removal of cobalt from ammonium chloride solutions using a batch cell through an electrogenerative process. *Separation and Purification Technology*, 162:154–161, 2016.

CIM. CIM Definition Standards. *Mineral Resources and Mineral Reserves*, May 2014. URL `http://michaelhorner.ca/wp-content/uploads/2016/05/CIM_DEFINITION_STANDARDS_20142.pdf`. Online; accessed: 23-04-2019.

Cliffel, D. E. and Bard, A. J. Scanning Electrochemical Microscopy. 36. A Combined Scanning Electrochemical Microscope-Quartz Crystal Microbalance Instrument for Studying Thin Films. *Analytical Chemistry*, 70(9): 1993–1998, 1998. doi: 10.1021/ac971217n.

Clowes, W. MMG Joins Glencore, ERG Reviewing Congo Plans After Tax Hike. *Bloomberg*, April 2019. URL `https://www.bloomberg.com/news/articles/2019-04-03/mmg-joins-glencore-erg-in-reviewing-congo-plans-after-tax-hike`. Online; accessed: 23-04-2019.

Commodity Research Bureau. *The CRB Commodity Yearbook 2005 with CD-ROM*. John Wiley & Sons, Inc., Hoboken, New Jersey, 2005. ISBN 978-0-471-74054-4.

Crundwell, F. K., Moats, M. S., Ramachandran, V., Robinson, T. G., and Davenport, W. G. Cobalt – Occurrence, Production, Use and Price. *Extractive Metallurgy of Nickel, Cobalt and Platinum Group Metals*, pages 357–363, 2011. doi: 10.1016/b978-0-08-096809-4.10028-0.

Cui, C. Q., Jiang, S., and Tseung, A. Electrodeposition of Cobalt from Aqueous Chloride Solutions. *Journal of The Electrochemical Society*, 137(11):3418–3423, 2006. doi: 10.1149/1.2086232.

Darton Commodities. Cobalt market review. *The magazine of the Minor Metals Trade Association*, 2016. URL `https://mmta.co.uk/wp-content/uploads/2016/08/100055_crucible_july_2013.pdf`. Online; accessed: 09-04-2019.

Das, S. and Subbaiah, T. Electrowinning of Cobalt. *Hydrometallurgy*, 12:317–333, 1984.

Dehaine, Q., Tijsseling, L., and Glass, H. Cobalt geology, geometallurgy and geomicrobiology (CoG3) project progress report. Update presentation for National History Museum, 2017.

Dewaele, S., Muchez, P., Vets, J., Fernandez-Alonzo, M., and Tack, L. Multiphase origin of the Cu–Co ore deposits in the western part of the Lufilian fold-and-thrust belt, Katanga (Democratic Republic of Congo). *Journal of African Earth Sciences*, 46(5):455–469, 2006. ISSN 1464-343X. doi: https://doi.org/10.1016/j.jafrearsci.2006.08.002.

Elsherief, A. E. Effects of cobalt, temperature and certain impurities upon cobalt electrowinning from sulfate solutions. *Journal of Applied Electrochemistry*, 33(1):43–49, 2003. ISSN 0021891X. doi: 10.1023/A:1022938824111.

Evans, J. Introduction and the Significance of Electrometallurgy. *Reference Module in Materials Science and Materials Engineering*, 2014(April 2015):1–13, 2015. doi: 10.1016/b978-0-12-803581-8.03594-3.

Fakui, R., Katayama, Y., and Miura, T. The effect of organic additives in electrode- position of co from an amide-type ionic liquid. *Electrochim. Acta 56*, 56, 2011.

Flis-Kabulska, I. Electrodeposition of cobalt on gold during voltammetric cycling. *Journal of Applied Electrochemistry*, 36(2):131–137, 2006. doi: 10.1007/s10800-005-9024-8.

François, A. L'extrémité occidentale de l'arc cuprifère shabien. mémoire du département géologique. gécamines, likasi, république du zaïre. *Etude géologique*, page 65, 1973.

François, A. Synthèse géologique sur l'arc cuprifère du Shaba (Rép. du Zaïre). *Centenaire de la Société Belge de Géologie*, pages 15–65, 1987.

Free, M. L. and Moats, M. *Hydrometallurgical Processing*, volume 3. Elsevier Ltd., 2015. ISBN 9783319157146. doi: 10.1007/978-3-319-15714-6_6.

Freyssinet, P., Butt, C. R. M., Morris, R. C., and Piantone, P. Ore-forming processes related to lateritic weathering. *Economic geology 100th anniversary volume*, pages 681–722, 2005. doi: 10.5382/AV100.21.

Fried, I. *The Chemistry of Electrode Processes*. Academic Press, London and New York, 1^{st} edition, 1973. ISBN 978-0-12-267650-5. doi: 10.1016/B978-0-12-267650-5.X5001-2.

Gabe, D. The role of hydrogen in metal electrodeposition processes. *Journal of Applied Electrochemistry*, 27: 908–915, 1997. doi: 10.1023/A:1018497401365.

García-Miranda Ferrari, A., Foster, C. W., Kelly, P. J., Brownson, D. A., and Banks, C. E. Determination of the Electrochemical Area of Screen-Printed Electrochemical Sensing Platforms. *Biosensors*, 8(2):1–10, 2018. ISSN 20796374. doi: 10.3390/bios8020053.

Glencore. Mutanda Mining Sarl; Sell side visit, November 2013. URL `https://www.glencore.com/dam/jcr:851138e1-268a-4554-ad03-c6b8dea21308/Glencore-Sell-Side-Analyst-Visit-Mutanda-201311.pdf`. Online; accessed: 17-04-2019.

Glencore. Resources & Reserves, December 2018. URL `https://www.glencore.com/dam/jcr:ae4466b4-7ef4-4407-ae00-6ca55b694028/GLEN_2018_Resources_Reserves_Report-.pdf`. Online; accessed: 23-04-2019.

Goodall, W. R., Scales, P. J., and Butcher, A. R. The use of QEMSCAN and diagnostic leaching in the characterisation of visible gold in complex ores. *Minerals Engineering*, 18(8):877–886, 2005. doi: 10.1016/j.mineng.2005.01.018.

Gottlieb, P., Butcher, A., Gottlieb, P., Wilkie, G., Sutherland, D., Suthers, S., Perera, K., Jenkins, B., Spencer, S., and Butcher, A. Process Mineral Applications Microscopy for Process. *Microtextural Mineralogy*, April:0–2, 2000. doi: 10.1007/s11837-000-0126-9.

Graham, D. J. *Standard Operating Procedures for Cyclic Voltammetry*. Lulu Press, Inc., Morrisville, North Carolina, 1^{st} edition, 2018. ISBN 978-1-38751-430-4.

Grdeń, M., Klimek, K., and Rogulski, Z. A quartz crystal microbalance study on oxidation of a cobalt electrode in an alkaline solution. *Electrochemistry Communications*, 11(2):499–503, 2009. ISSN 13882481. doi: 10.1016/j.elecom.2008.12.037.

Gürmen, S. and Friedrich, B. Recovery of Cobalt Powder and Tungsten Carbide from Cemented Carbide Scrap - Part I: Kinetics of Cobalt Acid Leaching. *World of Metallurgy*, 57(3):143–147, 2004.

Hannis, S., Bide, T., and Minks, A. Cobalt. *Britisch National Survey, Nottingham, United Kingdom*, 2009. URL `https://www.bgs.ac.uk/downloads/start.cfm?id=1400`. Online; accessed: 08-04-2019.

Harvey, D. *Reversibility – Chemical vs. Electrochemical*. McGraw-Hill Education, 1999. ISBN 0072375477.

Herman, R. E. and Beverley, D. Mineral Resource Estimate Update Report: Mutanda South Copper Deposit, DRC. Technical report, Riaan Herman Consulting cc., November 2016. Report number: R1125-2016-GMS.

Hune, N. and Sanderson, H. Glencore to halt production at world's largest cobalt mine. *The Financial Times*, August 2019. URL `https://www.ft.com/content/8cd1fd7a-b86c-11e9-96bd-8e884d3ea203`. Online; accessed: 30-09-2019.

Jamasmie, C. DRC says Ok for Glencore to take full control of Mutanda copper mine. *Mining.com*, January 2017. URL `http://www.mining.com/drc-says-ok-for-glencore-to-take-full-control-of-mutanda-copper-mine/`. Online; accessed: 18-04-2019.

Jeffrey, M. I., Choo, W. L., and Breuer, P. L. Effect of additives and impurities on the cobalt electrowinning process. *Minerals Engineering*, 13(12):1231–1241, 2000. ISSN 08926875. doi: 10.1016/S0892-6875(00)00107-2.

Kasa, T. and Solomon, T. Cyclic Voltammetric and Electrochemical Simulation Studies on the Electro-Oxidation of Catechol in the Presence of 4, 4-bipyridine. *American Journal of Physical Chemistry*, 5(3): 45–55, 1964. doi: 10.11648/j.ajpc.20160503.11.

Kirk–Othmer. *Kirk-Othmer Encyclopedia of Chemical Technology.* John Wiley & Sons, Inc., Hoboken, New Jersey, 1978. ISBN 978-0-47-148494-3. doi: 10.1002/0471238961.

Klingler, R. J. and Kochi, J. K. Electron-transfer kinetics from cyclic voltammetry. Quantitative description of electrochemical reversibility. *Journal of Physical Chemistry*, 85(12):1731–1741, 1981. ISSN 00223654. doi: 10.1021/j150612a028.

Kongstein, O. E., Haarberg, G. M., and Thonstad, J. Electrodeposition of Cobalt from Chloride Solutions. *Electrochem*, page 5, 1982.

Krause, A., Uhlemann, M., Gebert, A., and Schultz, L. The effect of magnetic fields on the electrodeposition of cobalt. *Electrochimica Acta*, 49(24):4127–4134, 2004. ISSN 00134686. doi: 10.1016/j.electacta.2004.04.006.

Kruger, T. Glencore buys stakes in Mutanda Mining and Katanga Mining. *Mining Review Africa*, February 2017. URL `https://www.miningreview.com/central-africa/glencore-buys-stakes-mutanda-mining-katanga-mining/`. Online; accessed: 18-04-2019.

Li, M., Wang, Z., and Reddy, R. G. Cobalt electrodeposition using urea and choline chloride. *Electrochimica Acta*, 123:325–331, 2014. ISSN 00134686. doi: 10.1016/j.electacta.2014.01.052.

Lupi, C. and Pilone, D. Electrodeposition of nickel-cobalt alloys: The effect of process parameters on energy consumption. *Minerals Engineering*, 14(11):1403–1410, 2001. ISSN 08926875. doi: 10.1016/S0892-6875(01)00154-6.

Matsushima, J. T., Pereira, E. C., and Trivinho-Strixino, F. Investigation of cobalt deposition using the electrochemical quartz crystal microbalance. *Electrochimica Acta*, 51:1960–1966, 2006. doi: 10.1016/j.electacta.2005.07.003.

Mbendi, M. Nickel and Cobalt Mining in Democratic Republic of the Congo - Copper and Cobalt Mining, 2005.

Metalary. Cobalt Price. *Los Angeles, CA: Bacic Media Group*, 2019. URL `www.metalary.com/cobalt-price/`. Online; accessed: 08-04-2019.

Miękoś, E., Krawczyk, B., Jaksender, M., Zieliński, M., Czarny, K., Kołodziejczyk, K., and Szczukocki, D. Influence of constant magnetic field on electrodeposition of metals, alloys, conductive polymers, and organic reactions. *Journal of Solid State Electrochemistry*, 22(6):1629–1647, 2018. ISSN 1432-8488. doi: 10.1007/s10008-017-3875-x.

Mishra, S., Lawrence, F., Mallika, C., Pandey, N. K., Srinivasan, R., Mudali, U. K., and Natarajan, R. Kinetics of reduction of nitric acid by electrochemical method and validation of cell design for plant application. *Electrochimica Acta*, 160(2):219–226, 2015. ISSN 00134686. doi: 10.1016/j.electacta.2015.01.099. URL `http://dx.doi.org/10.1016/j.electacta.2015.01.099`.

Mohanty, U., Rintala, L., Halli, P., Taskinen, P., and Lundström, M. Hydrometallurgical Approach for Leaching of Metals from Copper Rich Side Stream Originating from Base Metal Production. *Metals*, 8(1):40, 2018. doi: 10.3390/met8010040.

Natural History Museum. CoG^3 Consortium: Investigating the recovery of cobalt, October 2017. URL `http://www.nhm.ac.uk/our-science/our-work/sustainability/cog3-cobalt-project.html`. Online; accessed: 04-04-2019.

Nemtoi, G., Chiriac, H., Dragos, O., Apostu, M.-O., and Lutic, D. The Voltammetric Characterization of the Electrodeposition of Cobalt , Nickel and Iron on Gold Disk Electrode. *ACTA CHEMICA IASI*, 17:151–168, 2009.

New Pacific Metals Corp. Mineral Estimates - Reserves vs Resources, February 2018. URL `https://newpacificmetals.com/mining-101/mineral-estimates-reserves-vs-resources`. Online; accessed: 23-04-2019.

Nicholson, R. and Shain, I. Theory of stationary electrode polarography: single scan and cyclic methods applied to reversible, irreversible, and kinetic systems. *Analytical Chemistry*, 36:706–723, 1964.

Nusheh, M. and Yoozbashizadeh, H. Study on Electrowinning of Cobalt by Cyclic Voltammetry Technique. *Iranian Journal of Materials Science & Engineering*, 7(2):45–48, 2010.

Pletcher, D. *A First Course in Electrode Processes*. The Royal Society of Chemistry, Cambridge, United Kingdom, 2nd edition, 2009. ISBN 978-1-84755-893-0.

Pradhan, N., Subbaiah, T., Das, S. C., and Dash, U. N. Effect of zinc on the electrocrystallization of cobalt. *Journal of Applied Electrochemistry*, 27(6):713–719, 1997. doi: 10.1023/A:1018496006392.

Princeton Applied Research. Quartz Crystal Resonator, Instruction Manual, June 2007. URL `https://www.ameteksi.com/-/media/ameteksi/download_links/documentations/supportcenter/princetonappliedresearch/productmanuals/qa-cl3-4-5-and-6-and-others-instruction-manual-rev-1-20-0-0.pdf?la=en`. Online; accessed: 09-08-2019.

Rountree, K. J., Mccarthy, B. D., Rountree, E. S., Eisenhart, T. T., and Dempsey, J. L. A Practical Beginner's Guide to Cyclic Voltammetry. *Journal of Chemical Education*, 95:197–206, 2018. doi: 10.1021/acs.jchemed.7b00361.

Sanderson, H. Cobalt price hits highest level since 2008 on electric car demand. *The Financial Times*, March 2019. URL `https://www.ft.com/content/1e6303f6-2386-11e8-add1-0e8958b189ea`. Online; accessed: 08-04-2019.

Sanderson, H. and Hume, N. Glencore to cut workers at key DR Congo copper and cobalt mine. *The Financial Times*, February 2019. URL `https://www.ft.com/content/b180af9a-2bae-11e9-a5ab-ff8ef2b976c7`. Online; accessed: 23-04-2019.

Santoro, L., Tshipeng, S., Pirard, E., Bouzahzah, H., Kaniki, A., and Herrington, R. Mineralogical reconciliation of cobalt recovery from the acid leaching of oxide ores from five deposits in Katanga (DRC). *Minerals Engineering*, 137(February):277–289, 2019. ISSN 08926875. doi: 10.1016/j.mineng.2019.02.011.

Santos, J. S., Matos, R., Trivinho-Strixino, F., and Pereira, E. C. Effect of temperature on Co electrodeposition in the presence of boric acid. *Electrochimica Acta*, 53(2):644–649, 2007. ISSN 00134686. doi: 10.1016/j.electacta.2007.07.025.

Sauerbrey, G. Verwendung von Schwingquarzen zur Wägung dünner Schichten und zur Mikrowägung. *Zeitschrift für Physik*, 155(2):206–222, 1959. doi: 10.1007/BF01337937.

Schwarzacher, W., Masliy, A., Medvedev, A., Kutuso, K., and Lafouresse, M. pH dependence of the composition of electrodeposited Co films in aqueous sulfate solutions. *Russian Journal of Electrochemistry*, 43(7):856–858, 2007. ISSN 1023-1935. doi: 10.1134/s1023193507070178.

Semenova, D., Zubov, A., Silina, Y. E., Micheli, L., Koch, M., Fernandes, A. C., and Gernaey, K. V. Mechanistic modeling of cyclic voltammetry: A helpful tool for understanding biosensor principles and supporting design optimization. *Sensors and Actuators, B: Chemical*, 259:945–955, 2018. doi: 10.1016/j.snb.2017.12.088.

Shedd, K. Cobalt (Mineral Commodity Survey). *US Geological Survey, US Department of the Interior, Reston, VA*, 2017. URL `https://minerals.usgs.gov/minerals/pubs/commodity/cobalt/mcs-2017-cobal.pdf`. Online; accessed: 08-04-2019.

Su, C., Maozhong, and Yang, P. Electrochemical behavior of cobalt from 1-butyl-3-methylimidazolium tetrafluoroborate ionic liquid. *Journal of Applied Surface Science*, 44(6), 2010. doi: 10.1016/j.apsusc.2010.02.087.

Tijsseling, L. T. Linking the Characterisation of Cobalt-Bearing Copper Ore to Comminution Properties. Master's thesis, Delft University of Technology, the Netherlands, 2017.

Tkaczyk, A. H., Bartl, A., Amato, A., Lapkovskis, V., and Petranikova, M. Sustainability evaluation of essential critical raw materials: cobalt, niobium, tungsten and rare earth elements. *Journal of Physics D: Applied Physics*, 51(20):26, 2018. ISSN 13616463. doi: 10.1088/1361-6463/aaba99.

UK Research and Innovation. CoG^3: The geology, geometallurgy and geomicrobiology of cobalt resources leading to new product streams, 2017. URL `https://gtr.ukri.org/projects?ref=NE%2FM011488%2F1`. Online; accessed: 04-04-2019.

USGS. Cobalt Statistics. *US Geological Survey, Reston, VA*, 2019. URL `https://minerals.usgs.gov/minerals/pubs/historical-statistics/ds140-cobal.xlsx`. Online; accessed: 08-04-2019.

Vanysek, P. Electrochemical Series. *CRC Handbook of Chemistry and Physics*, pages 20–29, 2010. URL `https://sites.chem.colostate.edu/diverdi/all_courses/CRC%20reference%20data/electrochemical%20series.pdf`. Online; accessed: 17-04-2019.

Walt, V. and Meyer, S. Blood, Sweat, and Batteries. *Fortune*, August 2018. URL `http://fortune.com/longform/blood-sweat-and-batteries/`. Online; accessed: 17-04-2019.

Wang, J., Xu, C., Liu, P., Tong, Y., and Liu, G. Preparation of y-co alloy film in acetamide-urea-nabr melt. *T. Nonferr. Metal. Soc.*, 12(6), 2002.

Wang, J. *Analytical Electrochemistry.* John Wiley & Sons, Inc., Hoboken, New Jersey, 3rd edition, 2006. ISBN 978-0-471-67879-3. doi: 10.1002/0471790303.

Wang, S., Wang, J., and Gao, Y. Development and use of an open-source, user-friendly package to simulate voltammetry experiments. *Journal of Chemical Education*, 94(10):1567–1570, 2017. doi: 10.1021/acs.jchemed.6b00986.

Wendorff, M. Genetic aspects of the Katangan megabreccias: Neoproterozoic of Central Africa. *Journal of African Earth Sciences*, 30(3):703–715, 2000. ISSN 1464-343X. doi: https://doi.org/10.1016/S0899-5362(00)00047-6. 50th Anniversary of the Geological Survey.

Wimberley, F., Onley, P., van der Schyff, W., Cunningham, E., Eckstein, S., Lotheringen, J., Anderson, S., and Johnstone, K. Mineral Expert's Report: Mutanda. Technical report, Golder Associates Africa, Ltd., May 2011. URL `https://www.miningdataonline.com/reports/Mutanda_May_2011_TR.pdf`. Online; accessed: 17-04-2019. Report number: 12971-10171-3.

WMD. *World Mining Data 2018, Iron and Ferro Alloy metals, Non-Ferrous Metals, Precious Metals, Industrial Minerals, Mineral Fuels.* Federal Ministry of Sustainability and Tourism, Vienna, Austria, 2018. ISBN 978-3-901074-44-8.

Xu, C., Pan, W., Yuan, D., Tong, Y., and Liu, G. Preparation of gd-co alloy film in acetamide-urea-nabr melt. *T. Nonferr. Metal. Soc.*, 12(5), 2002.

Yang, Q., D.R., Q., Zhu, D., and Sa, L. Electrodeposition of cobalt and rare earth- cobalt in urea-nabr-kbr melt. *Electrochemistry*, 1(3), 1995.

Yu, Y., Song, Z., Ge, H., Wei, G., and Jiang, L. Effects of Magnetic Fields on the Electrodeposition Process of Cobalt. *International Journal of Electrochemical Science*, 10:4812–4819, 2015.

Zhang, W., Singh, P., and Muir, D. Oxidative precipitation of manganese with SO2/O2 and separation from cobalt and nickel. *Hydrometallurgy*, 63(2):127–135, 2002. ISSN 0304386X. doi: 10.1016/S0304-386X(01)00205-5.

Zhao, F., Xu, Y., Mibus, M., and Zangari, G. The induced electrochemical codeposition of Cu-Ge alloy films. *Journal of the Electrochemical Society*, 164(6):D354–D361, 2017. ISSN 19457111. doi: 10.1149/2.1241706jes.

A

Lithostratigraphic units of the KCB

Equivalence between revised and former lithostratigraphic units of the Katanga Supergroup (Modified from: Cailteux and De Putter, 2019).

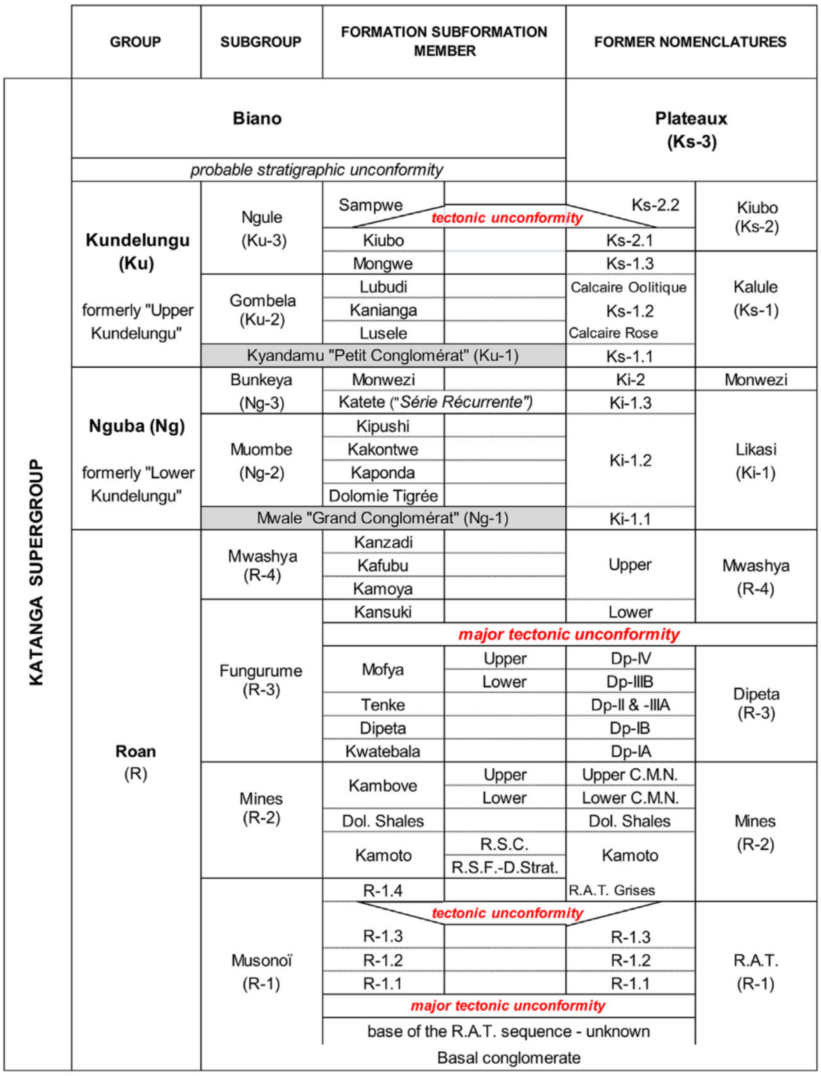

	GROUP	SUBGROUP	FORMATION SUBFORMATION MEMBER		FORMER NOMENCLATURES	
KATANGA SUPERGROUP	**Biano**				**Plateaux (Ks-3)**	
	probable stratigraphic unconformity					
	Kundelungu (Ku) formerly "Upper Kundelungu"	Ngule (Ku-3)	Sampwe		Ks-2.2	Kiubo (Ks-2)
			tectonic unconformity			
			Kiubo		Ks-2.1	
			Mongwe		Ks-1.3	Kalule (Ks-1)
		Gombela (Ku-2)	Lubudi		Calcaire Oolitique	
			Kanianga		Ks-1.2	
			Lusele		Calcaire Rose	
		Kyandamu "Petit Conglomérat" (Ku-1)			Ks-1.1	
	Nguba (Ng) formerly "Lower Kundelungu"	Bunkeya (Ng-3)	Monwezi		Ki-2	Monwezi
			Katete ("*Série Récurrente*")		Ki-1.3	Likasi (Ki-1)
		Muombe (Ng-2)	Kipushi		Ki-1.2	
			Kakontwe			
			Kaponda			
			Dolomie Tigrée			
		Mwale "Grand Conglomérat" (Ng-1)			Ki-1.1	
	Roan (R)	Mwashya (R-4)	Kanzadi		Upper	Mwashya (R-4)
			Kafubu			
			Kamoya			
		Fungurume (R-3)	Kansuki		Lower	
			major tectonic unconformity			
			Mofya	Upper	Dp-IV	Dipeta (R-3)
				Lower	Dp-IIIB	
			Tenke		Dp-II & -IIIA	
			Dipeta		Dp-IB	
			Kwatebala		Dp-IA	
		Mines (R-2)	Kambove	Upper	Upper C.M.N.	Mines (R-2)
				Lower	Lower C.M.N.	
			Dol. Shales		Dol. Shales	
			Kamoto	R.S.C.	Kamoto	
				R.S.F.-D.Strat.		
		Musonoï (R-1)	R-1.4		R.A.T. Grises	
			tectonic unconformity			
			R-1.3		R-1.3	R.A.T. (R-1)
			R-1.2		R-1.2	
			R-1.1		R-1.1	
			major tectonic unconformity			
			base of the R.A.T. sequence - unknown			
		Basal conglomerate				

B

Mineral Mass (%) based on density weighted QEMSCAN analysis.

CSM Lab Code Sample ID	18GL3**1** MM17 CC	18GL3**3** MM22 CC	18GL3**5** MM24 CC	18GL3**D** MM31 CC	18GL3**E** MM31 T	18GL3**F** MM32 CC
	Mineral mass (%):					
Carrollite*	46.74	36.24	29.51	24.39	0.65	64.09
Heterogenite*	0.01	0.00	0.00	0.00	0.00	0.00
Chalcopyrite	16.13	1.09	1.22	28.95	1.53	3.55
Bornite	0.16	49.32	53.37	0.33	0.01	15.51
Chalcocite	0.05	2.20	1.47	0.02	0.00	0.28
Pyrite	4.21	0.04	0.18	0.07	0.01	0.06
Barite	0.04	0.00	0.00	0.03	0.00	0.00
Gypsum	0.01	0.00	0.01	0.00	0.00	0.00
Chrysocolla	0.96	0.45	0.31	0.80	0.17	0.42
Heterogenite	0.01	0.00	0.00	0.00	0.00	0.00
Fe-Ox/CO3	0.10	0.19	0.47	0.15	0.21	0.24
Rutile	0.37	0.10	0.04	0.62	1.21	0.07
Ilmenite	0.00	0.00	0.00	0.00	0.00	0.00
Dolomite	0.19	2.24	5.17	2.14	14.22	5.05
Fe Dolomite/Ankerite	0.03	0.08	0.05	0.09	0.40	0.08
Apatite	0.06	0.16	0.02	0.16	0.68	0.02
Magnesite	0.00	0.00	0.02	0.00	0.01	0.07
Quartz	16.91	3.68	7.12	17.42	25.00	6.15
Plagioclase	0.28	0.01	0.04	0.39	1.08	0.02
K-feldspar	9.48	0.01	0.01	10.17	23.82	0.17
Muscovite/Illite	2.67	0.00	0.01	3.48	4.32	0.02
Biotite	0.99	0.00	0.00	0.79	0.85	0.01
Phlogopite	0.08	0.00	0.00	5.80	15.10	0.05
Magnesiochlorite	0.28	3.95	0.80	4.12	10.57	1.99
Mg silicates	0.02	0.20	0.14	0.04	0.09	2.13
Kaolinite	0.16	0.00	0.01	0.02	0.03	0.00
Zircon	0.00	0.00	0.00	0.01	0.01	0.00
Monazite	0.01	0.00	0.00	0.01	0.01	0.00
Others	0.05	0.03	0.04	0.02	0.01	0.02

* = Cobalt bearing mineral.

C

Analysed Mutanda samples.

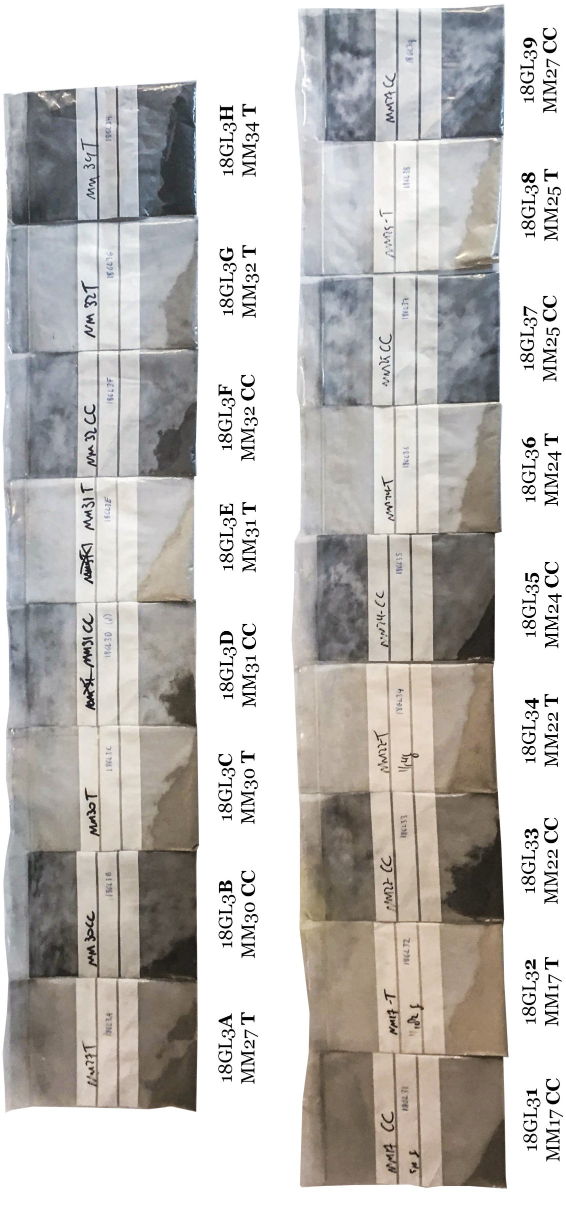

18GL3A MM27 T
18GL3B MM30 CC
18GL3C MM30 T
18GL3D MM31 CC
18GL3E MM31 T
18GL3F MM32 CC
18GL3G MM32 T
18GL3H MM34 T
18GL31 MM17 CC
18GL32 MM17 T
18GL33 MM22 CC
18GL34 MM22 T
18GL35 MM24 CC
18GL36 MM24 T
18GL37 MM25 CC
18GL38 MM25 T
18GL39 MM27 CC

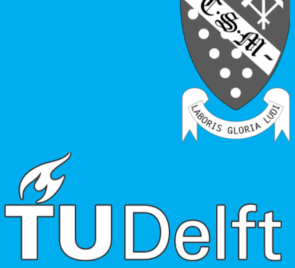
C.S.M.
LABORIS GLORIA LUDI
TU Delft